UNIVERSITÀ DEGLI STUDI DI CATANIA

DOTTORATO DI RICERCA IN FISICA - XXII CICLO

Roberto Susino

INVESTIGATING THE CHARACTERISTICS OF CORONAL LOOP HEATING BY HYDRODYNAMIC SIMULATIONS

TESI DI DOTTORATO

Tutor: Prof. L. Paternò
Supervisor: Dott. D. Spadaro
Coordinatore: Prof. F. Riggi

DICEMBRE 2009

PREFACE

The analysis presented here, dealing with the long-standing problem of the heating of the solar corona, constitutes the main topic of my research work of the last three years. Part of the results of this study are also discussed in a paper recently accepted for publication in the Astrophysical Journal and currently in press. The corresponding manuscript version is enclosed in Appendix B.

During my PhD course, I also addressed some aspects relevant to the problem of the identification of the slow wind acceleration regions, which appear to be associated with the bright, helmet-shaped coronal structures known as coronal streamers. In order to extend the knowledge of the physical characteristics of these structures and of their surroundings, as well as to investigate their connection with the origin of the slow solar wind, I contributed to the analysis of spectral observations of a narrow, mid-latitude streamer performed with SOHO UVCS in 2004. This study led to the publication of two papers (Susino et al. 2008, Spadaro et al. 2007), reported in Appendix B.

CONTENTS

INTRODUCTION

The nature of the mechanisms for heating the solar corona has been one of the most intensely studied problems in solar physics during the past six decades, and yet it remains one of the least understood.

Up until about 1940, it was thought that the temperature of the Sun decreased from the solar surface. However, when it was realized that emission lines seen during total solar eclipses were due to known elements at very high stages of ionisation, solar physicists were confronted with the puzzle of how the temperature in the outer solar atmosphere could pass from the value of about 6000 K in the photosphere to the surprisingly higher $1 - 2$ million degrees (or even more) in the corona.

Since there, the so-called "coronal heating problem" has been restricted by substantial progresses in theoretical modelling, new high-resolution imaging by satellite telescope observations, and more sophisticated data analysis. Nevertheless, a number of important issues must be addressed yet. In particular, the question on whether the plasma heating inside coronal structures is the effect of steady or time-dependent processes, uniform or localised somewhere in space, is still open.

Several theories for coronal heating have been proposed, each of them invoking different physical mechanisms producing different characteristics in the energy deposition, but it has proved difficult to determine which ones, if any, are actually correct. It is clear that a definitive test of any coronal heating model requires a quantitative prediction of observable quantities that is based on a detailed treatment. Plausible theories must be able to tie together a number as large as possible of the observational evidences that have been inferred from the high-quality data delivered by recent solar missions, such as *Yohkoh*, the Solar and Heliospheric Observatory (SOHO), the Transition Region and Coronal Explorer (TRACE), and *Hinode*.

EUV and X-ray imaging data from these satellites have revealed that the outer solar atmosphere is highly structured. Non-uniformities are present in both plasma density and temperature and should be a direct result of spatial and temporal variations in the rate of coronal heating. In particular, it has been well established that much of the plasma in the Sun's corona is confined by the magnetic field in distinct, arch-shaped structures known as coronal loops.

Such coronal loops are characterized by different lengths, temperatures, activity levels, and appear to evolve with lifetimes of the order of several hours. The dynamic behaviour as well as the radiative properties of the plasma inside these structures are clear signatures of unknown mechanisms that are responsible for their heating. While early observations of coronal loops were made primarily in soft X-rays and suggested that these structures are in states of quasi-static equilibrium under the action of steady heating, more recent measurements in the EUV have pointed out a number of discrepancies between the predicted features of steady heating models and the characteristics of the observed loops, particularly at low temperatures. It emerges from this picture that coronal loops most probably evolve in response to heating that is strongly time-dependent. Moreover, it is unlikely that any of the suggested heating mechanism provides a continuous, constant supply of heat to the corona.

Theoretical models of coronal loop heating involve as a primary energy source chromospheric footpoint motions or upward leaking Alfvén waves which are dissipated in the corona by a series of possible mechanisms, such as magnetic reconnection, resonant absorption, or phase mixing. Most of these mechanisms produce heating on individual magnetic flux surfaces (i.e., strands) that is impulsive in nature. Therefore, the hypothesis that coronal loops are heated by many tiny, small-scale energetic events, as envisioned by the so-called "nanoflare theory", has recently been advanced. This model postulates that loops are bundles of thin, unresolved magnetic strands that are independently heated by storms of energy pulses.

The concept of nanoflares is appealing for several reasons, but particularly because of its flexibility. Nanoflare-heated loops can in fact achieve quasi-steady conditions if the pulses repeat sufficiently rapidly in each strand, although the heating is indeed time-dependent. Moreover, uniform or non-uniform heating

conditions can be obtained if nanoflares are concentrated at a particular location or distributed along the whole structure of the loop.

In this work we analyse the dynamic behaviour of the plasma confined in a magnetic flux-tube and subject to different kinds of heating regimes. We consider both steady and impulsive heating. In the latter case, the particular nanoflare model we use is generic in the sense that it does not specify a particular energy dissipation mechanism. We also examine both the cases of uniform and footpoint-concentrated heating.

The loop plasma evolution in response to these different heating regimes is derived through one-dimensional numerical simulations performed with the Adaptively Refined Godunov Solver (ARGOS) hydro-code, which solves the standard set of hydrodynamic equations for a non-turbulent, compressible fluid flow. ARGOS employs a fully adaptive computational grid by using the Parallel Adaptive Mesh refinement package (PARAMESH). Hence, it is capable of resolving steep gradient regions and/or discontinuities that are likely to develop during the loop plasma evolution.

Our objective is to investigate on whether the variation of the heating properties (i.e., the parameters defining the temporal and spatial dependence of the energy deposition) can affect the hydrodynamic behaviour of the plasma filling the loop and, if so, what kind of signatures produces on the plasma-related observable quantities. The relevant consequences of the different heating regimes on some plasma diagnostics, such as the Doppler shifts of some coronal and transition region spectral lines and the differential emission measure distribution, are therefore discussed in detail, together with the indications that the variety of conditions found in this exploration give on the physical origins of coronal heating and related phenomena.

Our results show that thermal non-equilibrium and, consequently, condensation formation cycles develop along the loop when impulsive heating, with a pulse repetition times lower than the plasma characteristic cooling time, is localised at the loop footpoints and the pulse energy is below a threshold above which the heating balances the radiative losses, thus preventing the catastrophic cooling that triggers the condensation.

Condensations appear to significantly affect spectral lines forming at transition region temperatures, that exhibit rather pronounced red-shifts indicating downflows that trace out the motion of the condensation towards the solar surface. Coronal lines show substantial blue-shifts of their centroids only when impulsive heating has a pulse cadence time longer than the characteristic cooling time of the loop; hence, analysis of these spectral lines could be useful in discriminating between localised heating regimes with high or low nanoflare repetition times.

Conversely, a condensation does not produce observable signatures in the differential emission measure distribution (DEM) because it does not redistribute the plasma over a sufficiently large temperature range. On the other hand, the DEM coronal peak is found sensitive to the pulse cadence time when this is longer or comparable to the plasma cooling time. However, the DEMs derived from our models appear to be unable to reproduce both the transition region and the coronal structure of some observed DEMs with a unique set of heating parameters.

Finally, our simulations could give an explanation of the warm overdense and hot underdense loops observed by TRACE, SOHO, *Yohkoh*, and *Hinode*. Overdense conditions at relatively low temperatures are attained by condensation-forming models, while underdense conditions at higher temperatures are generally achieved by impulsive heating models with low cadence times and high nanoflare energies.

The thesis is organised as follows. Chapter 1 gives a general description of the solar corona and its structures, and discusses the main topics and issues related to the coronal heating problem. Chapter 2 reviews the basic physics of hydrodynamics applied to the coronal plasma. Chapter 3 describes in detail the numerical model adopted in this work and the characteristics of the simulations that have been performed. The main results of our analysis, concerning both the evolution of the plasma physical parameters and the plasma-related diagnostics, are reported and discussed in Chapters 4 and 5, respectively. In Chapter 6 we discuss the informations and implications deriving from our investigation.

1

THE SOLAR CORONA HEATING PROBLEM

1.1 CHARACTERISTICS OF THE SOLAR CORONA

The solar corona is the high-temperature portion of the Sun's outer atmosphere, beginning slightly above the visible surface (the photosphere) and extending hundred of thousands kilometres, or further, into interplanetary space.

Images such as those obtained by the latest solar spacecrafts, like *Yohkoh*, TRACE, SOHO, and *Hinode*, have shown that the density and temperature structure of the solar corona is far from a simply conceived hydrostatic, uniform, and gravitationally stratified atmospheric model, but rather shows highly inhomogeneous features. A lot of dynamic processes heat up the chromospheric plasma that is driven by the over-pressure upwards into the corona, producing over-dense structures with densities that exceed those of the ambient quiet corona.

The plasma particle density in the solar atmosphere decreases rather rapidly with height above the surface, from about 10^{17} cm^{-3} in the photosphere to nearly 10^6 cm^{-3} at a height of 1 $R_\odot$ (i.e., one solar radius) in the upper corona. The transition region at the base of the corona constitutes an abrupt boundary where the coronal density decreases by several orders of magnitude.

The temperature initially decreases from the photospheric value of $\sim$ 6000 K to a minimum of $\sim$ 4300 K, at the top of the photosphere; subsequently, it rises slowly through the lower chromosphere, then dramatically through the transition region, reaching the surprising value of a few million degrees in the corona. Thereafter, the temperature falls quite slowly in the outer corona, which is expanding outwards as the solar wind, to a value of $\sim 10^5$ K at 1 AU.[1] While in the chromosphere the plasma is only partially ionised, since the average temperature is $\sim$ 11000 K (the proton to neutral hydrogen density ratio, H^+/H, is about 10^{-3}

1 One Astronomical Unit (AU) corresponds to the mean distance of the Sun from Earth, and it is equal to $\sim 1.5 \times 10^8$ km.

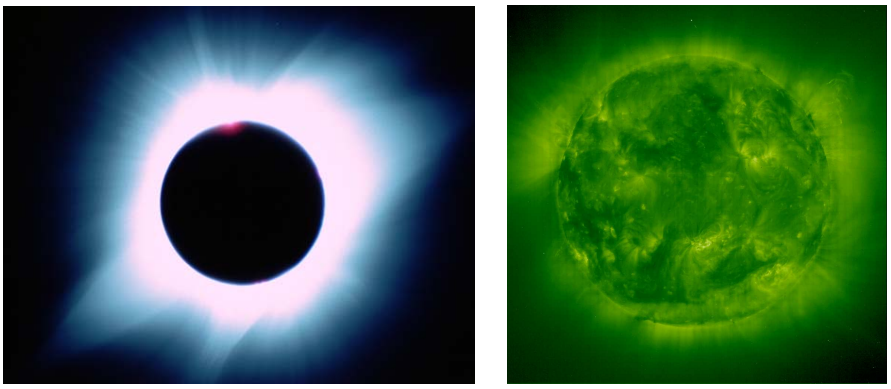

(a) (b)

Figure 1.1: (a) The solar corona observed in white-light during the solar eclipse of August 11, 1999. (b) A SOHO/EIT Fe XII image of the Sun, recorded in the same day, at a wavelength of 195 Å, sensitive in the temperature range of $1.2 - 1.5$ MK.

at the base of the chromosphere), in the corona the temperature is so high that coronal plasma is fully ionised. Therefore, the corona is very faint and cannot normally be seen in white light, since it emits very little compared with the photosphere; white-light observations can be performed only during solar eclipses (see Fig. 1.1a), when the brighter photospheric layers are occulted by the Moon, or by means of a particular instrument, the coronagraph.

Conversely, in EUV and soft X-rays the corona appears much more bright and can be observed directly, since the contribution from the inner atmosphere is negligible in these spectral ranges. Clearly, the disadvantage of observing in EUV and soft X-rays is that such wavelengths are absorbed by the Earth's atmosphere, so that observations are only possible from space, by means of dedicated space-borne missions (Fig. 1.1b).

From EUV and X-ray imaging data, the Sun's corona appears highly structured. It has been understood that the solar magnetic field plays a fundamental role in controlling the topology and dynamics of all coronal structures and phenomena. A basic parameter is the ratio of the plasma thermal pressure, p_{th}, to the magnetic pressure, p_{mag}, the so-called plasma β-parameter. It is defined as

$$\beta = \frac{p_{th}}{p_{mag}} = \frac{nk_BT}{B^2/8\pi}, \tag{1.1}$$

where n (cm^{-3}) is the plasma number density, k_B (erg K^{-1}) the Boltzmann constant, T (K) the plasma temperature, and B (Gauss) is the magnetic field. Typical values for B in the corona are of $50 - 100$ Gauss in resolved elements within the active regions.

Owing to the low-density and high-temperature plasma conditions, in the large part of the solar corona the value of β is less than unity, that constitutes a rigorous topological constraint. The coronal plasma is magnetically confined and the inhibition of the cross-field transport has the consequence that every particle flow that streams from the chromosphere to the corona traces out bundles of magnetic field lines. Thus, the solar corona can be conceived as composed by structures that presumably trace the magnetic field.

There are two different magnetic regions in the corona, that fundamentally have different properties. Those in which the magnetic field lines are predominantly open appear relatively dark and are known as coronal holes; they always exist around the solar poles and sometimes, during solar activity maxima, extend towards the equator. Those in which the magnetic field lines are mainly closed consist of many arch-shaped, bright, and dense structures called coronal loops (see Fig. 1.2).

Coronal loops are ubiquitous (outside coronal holes), but most conspicuously seen in active regions. They consist of magnetic flux tubes that emerge from the inner layers of the solar atmosphere through the mechanism of magnetic buoyancy, and expand into the chromosphere and corona. The regions where the loops are anchored in the photosphere, the so-called footpoints, have opposite magnetic polarity and are affected by the turbulent, random motions caused by the convective flows acting below the solar surface.

Coronal loops are characterized by very different values of lengths, temperatures, lifetimes, and activity levels. The longest loops join different active regions; they may be up to 700 Mm long and have maximum temperatures of about 2 to 3 MK. Active-region loops are rooted within a single active region and typically connect sunspots; they have lengths ranging from 10 to 100 Mm and temperatures up to ~ 5 MK. They are often structured in magnetic arcades. Quiet-region loops do not connect active regions and are somewhat cooler than the previous ones, with a temperature of about 1.5 MK. As far as the lifetime is concerned, a

single loop lasts typically many hours up to one day, but more complex systems may last for several solar rotations.

Active-region loops are not permanent coronal features, but they exhibit an intrinsically dynamic behaviour.

Even in quiescent, non-flaring conditions, cool EUV loops ($T \simeq 1 - 2$ MK) are characterized by strong temporal variability of emission and substantial plasma flows. For instance, CDS measurements (e.g., Kjeldseth-Mo & Brekke, 1998) showed significant changes in the physical structure of coronal loops over a period of about one hour, in particular seen in emission lines forming in the temperature range $T \simeq 0.1 - 0.5$ MK. This variability is generally associated to large Doppler-shifts, with corresponding velocities typically around $50 - 100$ km s^{-1}. Furthermore, recent CDS and EIT observations of coronal loops, performed with high temporal cadence, have revealed spatially localised brightenings, moving down towards the footpoints of the loops, probably associated to rapid plasma evacuation triggered by radiation-dominated cooling (De Groof et al., 2004).

The properties of X-ray loops are, conversely, almost different from those of EUV loops. For instance, *Yohkoh* SXT observations suggest that hot ($T \gtrsim 3$ MK) active-region loops may be classified into two components in terms of their temporal behaviour: a transient high-temperature ($T > 5$ MK) component, probably due to microflares, and a persistent low-temperature ($3 \lesssim T < 5$ MK) component. The contribution of the former to the overall heating of the corona is, however, small, while the persistent low temperature component is dominant in energetics (Nagata et al., 2003).

1.2 THE CORONAL HEATING PROBLEM

The reason for the temperature rise above the photosphere has been one of the major problems in solar physics ever since, and is not yet well understood.

When Grotrian (1939) and Edlén (1942), more than six decades ago, identified Fe IX and Ca XIV lines in the solar spectrum, a coronal temperature of about 1 MK was inferred from the formation temperature of these highly ionised elements. These measurements unavoidably stated that the corona consists of a fully ionised hydrogen plasma. Nevertheless, the maintenance of the temperatures necessary

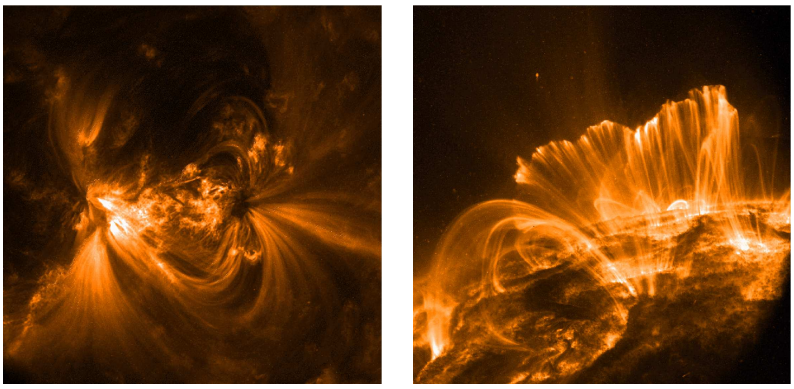

(a) (b)

Figure 1.2: TRACE Fe IX/X (171 Å) images of the million-degrees solar corona. (a) A coronal active region observed on the disk on June 2, 2000, where various sets of active-region loops are visible. (b) A post-flare magnetic arcade observed on the limb on November 8, 2000.

for such ionisation represents a perplexing issue, that is often referred to as the coronal heating problem.

It is clear that if only thermal conduction was at work, the temperature in the corona should steadily decrease from the photospheric value with increasing height, according to the second law of thermodynamics. Moreover, owing to the radiative losses by EUV emission, the corona should just cool off in a few hours, if some heating mechanism was not continuously supplying the right amount of energy to maintain the observed plasma temperature.

A basic requirement of any plausible heating theory is thus to: i) identify an energy source that can sustain the losses produced by thermal conduction and radiation in the corona; ii) determine the possible energy conversion, transport, and deposition mechanisms; and iii) predict the spectrum of emitted radiation and its manifestations as observable quantities.

1.2.1 *Heating energy requirement*

The energy necessary to heat the upper atmosphere has at least to balance the sum of the two major loss terms of conductive and radiative losses.

A thermal equilibrium has often been assumed to hold at each location, expressed as

$$H - C - R = 0, \tag{1.2}$$

where H is the unknown heating term, $C = \nabla \cdot \vec{F}_C$ is the conductive-loss term, given by the divergence of a conductive flux $\vec{F}_C$, and R is the radiative-loss term. Each of the previous terms represents an energy per unit volume and time (erg cm^{-3} s^{-1}). Since neighbouring structures are fully isolated, because of the highly organised structuring by the magnetic field, the heating requirement can be specified separately for each of them.

When the thermal equilibrium holds, the temperature distribution is determined by the relative sizes of R and H, and by the response of C in maintaining the thermal balance. In the chromosphere, R and H are of the same order of magnitude, and their difference, C, is very small. As the temperature rises, the radiation (R) increases, reaching a maximum between 10^4 and 10^5 K, and greatly exceeds the heating (H); this is the case of the lower transition region, where the radiation is so large that it cannot be supplied by mechanical heating and plasma has to be heated from above by conduction (C). In the lower corona, above 10^5 K, the radiative losses fall down dramatically: the energy deposited as heat cannot be radiated away and it must be transported by conduction inwards and outwards the region where the temperature maximum occurs.

Table 1.1 lists the energy losses per unit area in the corona, transition region, and chromosphere for comparison, given separately for active regions, quiet Sun, and coronal holes. For the corona, the losses due to the solar wind are also indicated, since this kind of energy transport becomes increasingly important and eventually it dominates conduction of heat outwards, above the temperature maximum of an open magnetic field region. It is worth noting that the energy necessary to balance the losses in the corona is only a few percent of that needed in the chromosphere. Moreover, the heating requirement in dense coronal loops within active regions is up to two orders of magnitude greater than that of the quiet Sun and coronal holes.

Table 1.1: Energy losses from the upper atmosphere (in units of erg cm^{-2} s^{-1}; adapted from Withbroe & Noise, 1977).

		Active Regions	Quiet Sun	Coronal Holes
CORONA	Conduction	$10^5 - 10^7$	2×10^5	6×10^4
	Radiation	5×10^6	10^5	10^4
	Solar wind	$(< 10^5)$	5×10^4	7×10^5
TRANSITION REGION	Conduction	–	–	–
	Radiation	2×10^6	3×10^5	3×10^5
CHROMOSPHERE	Conduction	–	–	–
	Radiation	2×10^7	4×10^6	4×10^6

1.2.2 *Overview of coronal heating models*

Although there is a quite specific perception of the energy requirements in the solar corona, the detailed nature of the heating mechanisms is highly controversial. In particular, the main features that need to be understood concern the temporal and spatial characteriztics of the heating processes.

The first theoretical models of coronal loop heating (e.g., Rosner et al., 1978; Serio et al., 1981) considered a steady heating term. They were initially able to predict and reproduce a large number of characteristics in the X-ray and EUV coronal emission of both the Sun and solar-type stars. Nevertheless, recent space-borne missions like *Yohkoh*, SOHO, TRACE, and *Hinode*, have delivered data of unprecedented quality, providing observations that are either completely or in part inconsistent with the plasma properties derived from steady-heating models. It would seem, therefore, that coronal loops must be heated in a time-dependent way.

Moreover, studies on the field-aligned spatial structures of the heating (see, e.g., Priest et al., 1998; Antiochos et al., 1999; Aschwanden et al., 2001; Reale, 2002; Karpen et al., 2003; Gudiksen & Nordlund, 2005) yielded conflicting results, so that it is not yet clear if the heating is uniform along a coronal loop,

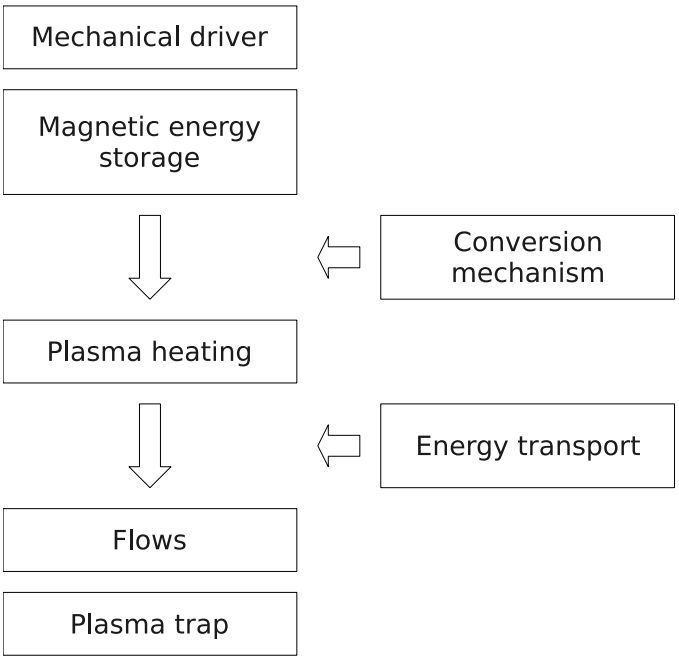

Figure 1.3: Flowchart showing the different steps that are involved in the coronal heating process.

concentrated around its top or near its footpoints, or randomly localised along its entire structure.

Several heating theories have been suggested to explain the energy input to the corona. In most of them, coronal heating is treated as a multi-stage process that involves a series of steps, as illustrated in Fig. 1.3: the energy coming from a mechanical driver (1) is initially stored by the magnetic field (2) and successively converted into heat by one or more conversion mechanisms (3). Coronal plasma is then heated (4) and the resulting overpressure induces particle flows (5), which become trapped in coronal loops (6), where they are eventually observed.

Presently, most of the coronal heating models cover only an incomplete subset of these steps. For instance, multi-dimensional full-MHD models are typically used to study the source and conversion of energy, but they provide little useful information on the response of the plasma and its radiation signatures. Conversely,

$1D$ hydrodynamic models are typically used to study the plasma response, but they treat the heating in a generic way, without regarding its physical origin.

The basic assumption of all heating theories is that the ultimate source of energy is represented by the random plasma motions caused by turbulence in and below the photosphere. These motions produce a displacement of the photospheric footpoints of coronal magnetic flux tubes and stress the field quasi-statically or generate Alfvén waves that propagate upwards, depending on whether the time-scale of the motions, τ, is long or short compared to the Alfvén transit time, τ_A, along the magnetic structure. Since

$$\tau_A = L/v_A = L/\sqrt{B^2/4\pi\rho}, \tag{1.3}$$

where L is the length of the flux-tube, v_A the Alfvén speed, and ρ the plasma mass density, the Alfvén transit time typically spans from a few tens of seconds for compact loops to some minutes for much longer loops.

It is customary to classify theoretical heating models into AC (Alternating Current) and DC (Direct Current) types, on the basis of the coronal response to the photospheric driver that provides the energy. If the photospheric driver, namely the turbulent motions induced by convection, changes the footpoint positions faster than a coronal loop can adjust itself to (e.g., by damping and dissipation of incident Alfvén waves), the loop will experience an alternating current excitation, which is characteristic of AC models. On the other hand, if the changes of the footpoint positions happen on time scales much longer than the Alfvén travel time along the loop, the loop will be able to reconfigure in a quasi-static way, and the coronal currents will be almost direct ones, that defines DC models.

AC heating models

In AC heating models, energy is provided by steepening and dissipation of waves.

Turbulent convective motions on the solar surface generate a large flux of waves propagating upwards. These waves are characterized by a variety of forms: acoustic, Alfvén, fast and slow magneto-sonic, for instance.

It has been pointed out that a very large wave flux of $\sim 10^7$ erg cm^{-2} s^{-1} is produced below the photosphere (Narain & Ulmschneider, 1996), but, even if an

energy flux of this magnitude is more than adequate to heat the corona, it is not clear how much of this flux reaches the higher levels.

Acoustic and magneto-acoustic waves are not able to reach the coronal layers, since they steepen and form shocks very rapidly, but Alfvén waves appear to be capable to penetrate into the corona. The estimated energy flux carried by Alfvén waves is something less than about 5×10^6 erg cm^{-2} s^{-1} in regions of strong magnetic field (Ulrich, 1996), so it is sufficient to heat coronal holes and quiet Sun, and marginally adequate to heat active region loops. Even though most of them are reflected in the upper chromosphere and transition region, a substantial fraction can be transmitted through a resonant cavity with a nearly standing Alfvén wave and dissipated through the mechanism of resonant absorption (e.g., Ionson, 1978; Hollweg, 1984, 1981; Poedts et al., 1994).

In the low plasma-β corona, the magnetic field varies very little across a loop structure, but the density can vary by several orders of magnitude. Therefore, the Alfvén speed ($v_A = \sqrt{B^2/4\pi\rho}$) is non-uniform across coronal loops due to the radial density variation. The mechanism of resonant absorption is based on the idea that absorption of Alfvén waves (by Ohmic and viscous dissipation) is greatly enhanced in narrow radial layers where the local resonance frequency, ν_{res}, matches the oscillation frequency of the incident wave, ν_{wave}.

A remarkable key point is that, even though the spatially averaged heating-rate carried by the Alfvén wave is approximately constant, the different magnetic flux-surfaces that make up the loop are impulsively heated as resonance layers pass by, since they will continually change from being resonant to non-resonant owing to the continuous variation of the cross-field density structure and of the resonant absorption profile (Ofman, 1998).

In particular, recent studies (see, e.g., Antolin & Shibata, 2009) have shown that the mechanism of resonant absorption produces heating in coronal loops that is time-dependent, with time-scales of the order of half the Alvén wave period, the most efficient period range for the heating being $200 - 300$ s.

DC heating models

When photospheric motions are sufficiently slow, the magnetic configuration of coronal structures evolves through a succession of equilibrium states which store

energy in excess of the potential one. The electric currents associated with such non-potential equilibria produce heating by ohmic dissipation that is, however, quite negligible, since the coronal conductivity is very low. The only way by which magnetic field dissipation can provide enough energy to heat the corona is by magnetic field changes with associated electric currents concentrations in tiny current-sheets, with dimensions typically less than a few metres, where magnetic energy is rapidly converted into heat through the process of magnetic reconnection. This is the basic idea of DC heating models.

Photospheric granular and super-granular flows twist coronal field lines by random angles and increase the magnetic stress energy, at a rate given by the Poynting flux through the base of coronal flux tubes:

$$\frac{dW}{dt} \approx \frac{1}{4\pi} B_{\perp} B_{\parallel} v, \tag{1.4}$$

where $B_{\perp}$ and $B_{\parallel}$ are the vertical and horizontal components of the field and v is the (horizontal) footpoint velocity (see, e.g., Klimchuk, 2006). Using for $B_{\perp}$ the typical active region value of $\sim$ 100 Gauss, for v the observed photospheric velocity of $\sim 10^5$ cm s^{-1}, and assuming $B_{\parallel} \approx B_{\perp}$, Eq. (1.4) gives $dW/dt \approx 10^7$ erg cm^{-2} s^{-1}, more than adequate to explain the observed energy losses of both the quiet Sun and active regions.

As the photospheric footpoints of coronal loops are twisted, the neighbouring coronal flux tubes will respond and interact each others, either moving apart or coming closer. At the interface between the flux-tubes, where the magnetic field lines are oppositely directed or simply inclined at a non-zero angle, a current-sheet is formed, the magnetic field reconnects, and magnetic stress energy is converted into heat (through ohmic dissipation), bulk kinetic energy, and fast-particle energy. Parker (1988) estimated that the energy conversion starts to take place when the twist angle between neighbouring magnetic field lines exceeds a critical threshold angle of about 14°. If the magnetic field is twisted up faster than its ohmic relaxation time, the energy excess will be stored until it is released as a flare-like event; once the heat has been released, it is conducted very efficiently along the magnetic field.

Current-sheets can be produced by several processes: for instance, by the interaction of topologically separate parts of large magnetic configurations, like active regions, or by the emerging of new magnetic flux from the photosphere within a region of pre-existing magnetic field. Current-sheets may also be formed when magneto-static equilibrium becomes unstable or even ceases to exist.

There is no question that DC heating is viable, at least from an energetic point of view. However, to understand in detail how the magnetic stress energy is converted into heat is a much difficult challenge. As far as the temporal characteristics of the heating through DC processes are concerned, MHD magnetic reconnection models provide useful informations on the energy dissipation time-scales. For instance, the Petschek-type magnetic reconnection mechanism (Petschek, 1964) predicts an impulsive heating of magnetic flux-tubes that are in contact with standing slow shocks emanating from the reconnection X-point, with energy pulses that last no more that a few tens of seconds. Even processes associated to the so-called secondary instability (see, e.g., Dahlburg et al., 2003, 2005; Klimchuk, 2006) produces impulsive heating events that last about 100 s.

1.2.3 *The nanoflare theory*

As already said, a significant amount of observational and theoretical evidence indicates that large part of the corona is in a state of ceaseless activity and evolves in response to heating that is strongly time-dependent (i.e., impulsive). The evidence further suggests that the cross-field spatial scale of heating is very small, so that unresolved structures are ubiquitous. On the basis of these indications, the hypothesis that the corona is heated by many tiny, small-scale magnetic-reconnection related events, as envisioned by the so-called nanoflare theory, has been advanced.

Long time ago, Parker (1988) introduced the idea of nanoflares, i.e. impulsive releases of roughly 10^{24} erg (some nine orders of magnitude lower than normal flares) produced by the dissipation of small current-sheets that form as a result of the photospheric motions of the loop footpoints. In its original form, the nanoflare heating model assumed that coronal loops consist of many elemental

flux tubes, or magnetic strands, whose cross-section dimensions are well below the typical instrumental resolution.

Observational profs of the multi-stranded composition of coronal loops come from recent spectroscopic measurements which show that most loops have broad differential emission measure distributions within their cross-section, i.e. they seem to be multi-thermal (Schmelz et al., 2001; Schmelz, 2002; Schmelz et al., 2003; Martens et al., 2002). Since energy transport is highly inefficient across the field lines in the solar corona, coronal loops are comprised of sub-resolution magnetic strands. However, there is also evidence of an isothermal cross-field structure at least for some coronal loops (see, e.g., Neupert et al., 1998; Aschwanden et al., 2001; Aschwanden, 2002; Del Zanna & Mason, 2003), which is inconsistent with the drawback of multi-stranded loops.

The nanoflare model has been developed and studied in considerable detail by many authors (e.g., Cargill, 1994; Klimchuk & Cargill, 2001; Spadaro et al., 2003; Cargill & Klimchuk, 2004; Reale et al., 2005; Patsourakos & Klimchuk, 2005; Klimchuk, 2006; Klimchuk et al., 2008). The basic idea is that each of the strands forming a coronal loop is heated impulsively, quasi-randomly and at different times from its neighbours. The frequency with which nanoflares recur in a given strand is a very important parameter of the model, since the properties of the plasma depend sensitively on whether the time interval between successive events is long or short compared to the radiative cooling time τ_{rad} (i.e., the time the loop would employ to radiatively cool down). The longer is the repetition time, more the system deviates from equilibrium; conversely, when nanoflares repeat very rapidly the situation is effectively the same as that of steady heating. On the basis of these simple concepts, the model is able to tie together a number of different observational concerns that otherwise would be of difficult interpretation.

Recent SOHO and TRACE observations have in fact pointed out that a large majority of warm coronal loops ($T \sim 1-2$ MK), although appearing in quasi-static conditions, are indeed over dense (Aschwanden et al., 1999, 2001; Winebarger et al., 2003; Patsourakos et al., 2004), while hot loops ($T > 2$ MK) observed by *Yohkoh* exhibit lower densities than those predicted by loop models in hydrostatic equilibrium (Porter & Klimchuk, 1995). Moreover, loops generally appear to live

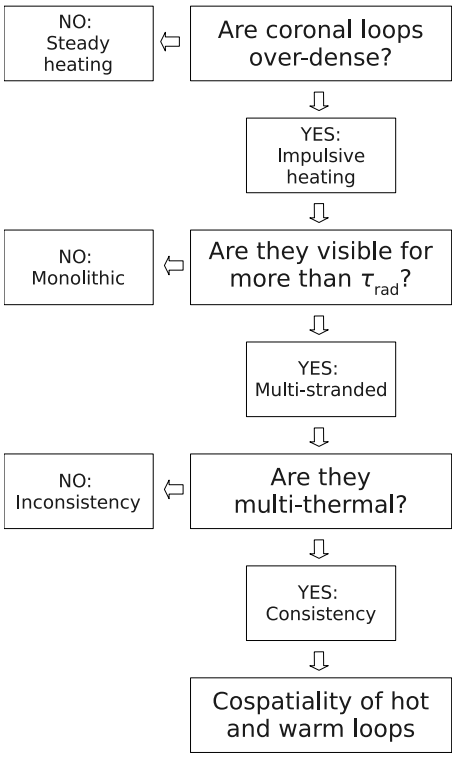

Figure 1.4: Schematic representation of the characteristics and issues of the nanoflare theory (from Klimchuk, Coronal Loops Workshop IV – Florence, 2009). Steady heating models with monolithic loops are consistent with isothermal structures, while cross-field multi-thermality is needed for impulsive-heating models when loops are visible for more than a radiative cooling time.

for a much longer time than the radiative cooling one. While X-ray loops support the view of steady heating (e.g., Porter & Klimchuk, 1995; Schrijver et al., 2004; Warren & Winebarger, 2006), EUV loops seem neither steadily heated (Aschwanden et al., 2000; Winebarger et al., 2003) nor cooled as monolithic structures.

It has been shown that the observed over-densities and time-scales could be explained just considering loops as bundles of nanoflare-heated strands, as long as nanoflares do not all occur at the same time (Klimchuk, 2006). Although each individual strand evolves rapidly, the whole ensemble that forms the loop will appear to change slowly compared with the radiative cooling time.

Yohkoh will preferentially detect the hottest strands while TRACE the warm ones, therefore the loops should be visible nearly simultaneously in a broad range

of temperatures. In other words, coronal loops should be detectable by both *Yohkoh* and TRACE at the same location, either at the same time or with a slight delay. Nevertheless, how often this is actually observed is still under debate (see, e.g., Klimchuk, 2006, and references therein). Some authors have shown that hot and warm loops tend to be mutually exclusive, since they preferentially appear in different parts of active regions; others have argued that hot and warm loops are located close each other, but not really overlap.

The problem of co-spatial hot and warm loops can be avoided if nanoflares are assumed to recur frequently, say with repetition times much shorter than the radiative cooling time within each strand. In these conditions a quasi-static equilibrium would be attained, where smaller events and lower frequencies would maintain warm strands, while larger events and higher frequencies would maintain hot strands.

In the framework of the nanoflare model, we tried to address these issues by performing hydrodynamic numerical simulations of coronal loops subject to different kinds of heating regimes. In particular, we considered heating either uniformly distributed along the loop or localised close to the chromospheric footpoints, in both steady-state and impulsive regimes. In the impulsive case, we considered different values for both the cadence of the injection of the energy pulses into the coronal segment of the loop and the amount of energy supplied by each nanoflare, in order to perform a exhaustive study of the consequences of the variation of such parameters for the loop structure and evolution.

2

HYDRODYNAMICS OF THE SOLAR CORONA

The plasma response to heating produced by either the dissipation of magnetic stresses or waves is extremely important, because the observable signatures needed to test any coronal heating theory depend critically on the physical state of plasma and also because the plasma response can affect, to some extent, the subsequent heating. Presently, one of the open points in addressing and solving the coronal heating problem is the gap between MHD treatments of the energy conversion mechanisms and hydrodynamic treatments of the plasma response.

The evolution of the basic plasma quantities, like temperature, density (or pressure), and velocity, can be derived by solving the classical hydrodynamic equations for a non-turbulent, compressible fluid flow, through numerical simulations in which different ranges of variability of the parameters characterizing the model are explored.

2.1 BASIC HYDRODYNAMIC EQUATIONS

The motion of an ideal gas in the presence of a gravitational field is governed by equations for the conservation of mass, momentum, and energy. For a compressible flow, when the gas viscosity is neglected, the standard set of time-dependent hydrodynamic equations may be written as

$$\frac{D}{Dt}\rho = -\rho\nabla\cdot\vec{v}, \tag{2.1a}$$

$$\rho\frac{D}{Dt}\vec{v} = -\nabla p - \rho\vec{g}_{\odot}, \tag{2.1b}$$

$$\rho T\frac{D}{Dt}S = H - R - \nabla\cdot\vec{F}_C, \tag{2.1c}$$

where

$$\frac{D}{Dt} = \frac{\partial}{\partial t} + \vec{v} \cdot \nabla \tag{2.2}$$

is the operator for the total derivative, ρ the plasma mass density, $\vec{v}$ the plasma velocity, p the pressure, $\vec{g}_\odot$ the local gravitational acceleration, and S is the entropy per unit mass.

The plasma pressure is determined by an equation of state, which is taken for simplicity as the perfect gas law:

$$p = nk_B T. \tag{2.3}$$

For a fully ionised hydrogen plasma it results $n = n_p + n_e = 2n_e$, $p = 2n_e k_B T$, and $\rho = n_p m_p + n_e m_e \simeq n_e m_p$ (the subscripts p and e denote protons and electrons, respectively).

The energy equation (2.1c) can alternatively be expressed in terms of the internal energy (ϵ) per unit mass of the plasma:

$$\rho \frac{D}{Dt}\epsilon - \frac{p}{\rho}\frac{D}{Dt}\rho = H - R - \nabla \cdot \vec{F}_C. \tag{2.4}$$

For an ideal gas, the internal energy is

$$\epsilon = \frac{1}{\gamma - 1}\frac{p}{\rho}, \tag{2.5}$$

where $\gamma = c_p/c_v$ is the adiabatic exponent that expresses the ratio of the specific heats at constant pressure (c_p) and at constant volume (c_v). An equivalent form for the internal energy is $\epsilon = c_v T$.

The conductive flux in the right-hand side of the energy equation may be written as $\vec{F}_C = -\underline{\underline{\kappa}} \nabla T$ (where $\underline{\underline{\kappa}}$ is the thermal conduction tensor) and its divergence, i.e. the conductive-loss term, split into two parts:

$$\nabla \cdot \vec{F}_C = \nabla_\parallel \cdot (-\kappa_\parallel \nabla_\parallel T) + \nabla_\perp \cdot (-\kappa_\perp \nabla_\perp T), \tag{2.6}$$

Table 2.1: The variation of χ and α with temperature (see Eq. 2.10), according to Rosner et al. (1978).

$\log T$			$\log\chi$	α
4.3	–	4.6	−21.85	0
4.6	–	4.9	−31	2
4.9	–	5.4	−21.2	0
5.4	–	5.75	−10.4	−2
5.75	–	6.3	−21.94	0
6.3	–	7.0	−17.73	−2/3

where subscripts $\parallel$ and $\perp$ refer to values along and across the magnetic field. Conduction along the magnetic field is primarily by electrons, while conduction across the field is mainly by protons and ions in general. For a fully ionised hydrogen plasma, Spitzer (1962) gives

$$\kappa_{\parallel} = 9.2 \times 10^{-7} T^{5/2} = \kappa_0 T^{5/2} \quad (\text{erg s}^{-1}\ \text{cm}^{-1}\ \text{K}^{-1}). \tag{2.7}$$

In the corona, $\kappa_{\perp} \ll \kappa_{\parallel}$ and the conduction is mainly along the field; in this case Eq. (2.6) simply reduces to

$$\frac{\partial}{\partial s} F_C = \frac{\partial}{\partial s}\left(-\kappa_0 T^{5/2} \frac{\partial}{\partial s} T\right), \tag{2.8}$$

in terms of the distance s along a particular magnetic field line.

For the optically thin part of the atmosphere ($T > 20000$ K in the transition region and corona), the radiative-loss term R in the energy equation takes the form:

$$R = n_e n_p \Lambda(T) \simeq n_e^2 \Lambda(T), \tag{2.9}$$

where $\Lambda(T)$ is called radiative-loss function. This function accounts for all the line contributions radiating at a given temperature T and it has been evaluated by a number of authors (Cox & Tucker, 1969; Cook et al., 1989; Landini & Monsignori Fossi, 1990; Martens et al., 2000, e.g.,). For practical applications in

hydrodynamic loop models, it has also been parametrized in the analytical form:

$$\Lambda(T) = \chi T^{\alpha} \quad (\text{erg cm}^3\ \text{s}^{-1}), \tag{2.10}$$

where χ and α are piecewise constants, whose different values are defined in several temperature ranges. Figure 2.1 shows the behaviour of various calculations of $\Lambda(T)$, together with the most commonly adopted approximation, derived by Rosner et al. (1978), while Table 2.1 lists the corresponding values of χ and α. The radiative-loss function presents a maximum around 10^5 K and a minimum around 10^7 K; between $10^{4.5} - 10^7$ K it is mostly dominated by contributions from the elements C, O, Si, and Fe.

Hydrodynamic equations for coronal loops may be written more specifically, in one dimension, as a function of the loop curvilinear coordinate s (i.e., the distance along a particular magnetic field line of the flux tube), by inserting the operator (2.2) explicitly, and the form (2.4) of the energy equation:

$$\frac{\partial}{\partial t}\rho = -\frac{\partial}{\partial s}(\rho v) \tag{2.11a}$$

$$\rho\frac{\partial}{\partial t}v + \rho v\frac{\partial}{\partial s}v = -\frac{\partial}{\partial s}p - \rho g_{\parallel} \tag{2.11b}$$

$$\rho\frac{\partial}{\partial t}\epsilon + \rho v\frac{\partial}{\partial s}\epsilon + p\frac{\partial}{\partial s}v = H - n_e^2\Lambda(T) - \frac{\partial}{\partial s}\left(-\kappa_0 T^{5/2}\frac{\partial}{\partial s}T\right), \tag{2.11c}$$

where $g_{\parallel}$ is the component of the gravity along the loop axis.

The generic solution of equations (2.11) has to match the boundary conditions at the edges of the computational domain. These consist in fixing the value of the plasma temperature, density, and velocity, together with the value of the temperature gradient, at $s = 0$ and $s = D$, where D is the total length of the modelled flux-tube. Often the system is conveniently assumed to be thermally isolated (for instance, when a temperature value near a chromospheric plateau is taken), and the condition for the temperature gradient becomes $(\partial/\partial s)T = 0$.

Although no analytical solution for the hydrodynamic equations can be derived, since the energy equation contains a differential equation of second order in temperature and the radiative-loss function is approximated in arbitrary ways, the

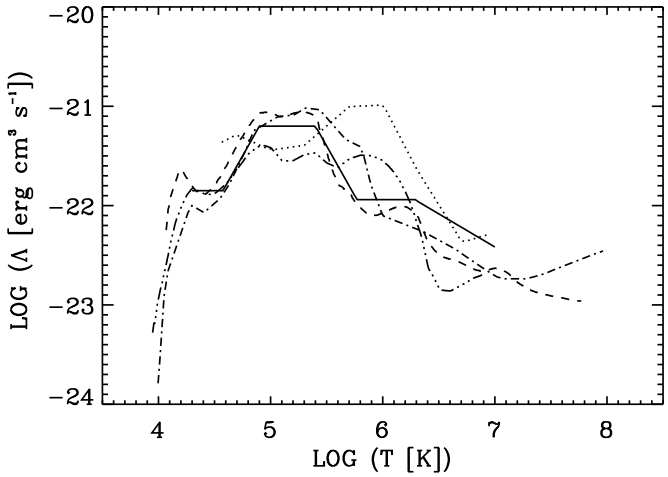

Figure 2.1: Comparison of various radiative-loss functions. Shown are the results of Cox & Tucker (1969, dot-dashed line), Cook et al. (1989, triple-dot-dashed line), Landini & Monsignori Fossi (1990, dashed line), Martens et al. (2000, dotted line), and the piecewise power-law approximation of Rosner et al. (1978, solid line).

system (2.11) can be numerically solved, either by explicit codes (e.g., starting from one boundary and adjusting the free parameters until the solution matches the second boundary condition) or by implicit codes (e.g., keeping the parameters at the boundaries fixed and optimising the solution in between).

2.2 HYDROSTATIC SOLUTIONS

Even though the solar corona is highly dynamic, many coronal structures, especially those with the longest life-times, are found to settle into a nearly stationary state most of the time, since dynamic phenomena, in the solar corona, often evolve into a quasi-static equilibrium.

Therefore, it appears evident that is possible to neglect both the time-dependence ($\partial/\partial t = 0$) and flows ($v \rightarrow 0$) in the hydrodynamic equations, and to

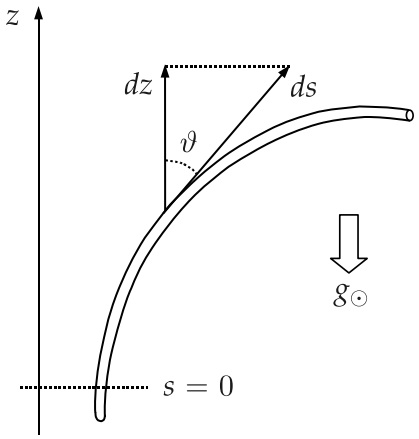

Figure 2.2: A magnetic flux tube inclined at ϑ to the vertical z-axis. Distance s is measured along the field lines from the photospheric footpoint at $s = 0$.

consider, amongst all the mathematically possible solutions, only those characterizing stationary states. The system (2.11) thus reduces to:

$$\frac{d}{ds}p + m_p n_e g_{\parallel} = 0 \tag{2.12a}$$

$$H - n_e^2 \Lambda(T) - \frac{d}{ds}\left(-\kappa_0 T^{5/2}\frac{d}{ds}T\right) = 0. \tag{2.12b}$$

The assumption of vanishing flows can be considered valid when the flow speed is much smaller than both the adiabatic sound speed ($c_s = \sqrt{\gamma p/\rho}$), the Alfvén speed ($v_A$) and the gravitational free-fall speed. Each solution for density $n_e(s)$ (or pressure p) and temperature $T(s)$, that satisfies both the equations (2.12), the ideal gas law ($p = 2n_e k_B T$), and the boundary conditions expressed above, is called hydrostatic solution.

The study of hydrostatic solutions is of relevant importance, because on the one hand equations (2.12) are simpler than the full hydrodynamic system (2.11) and can be solved either numerically or analytically under particular conditions, on the other hand hydrostatic solutions provide a number of useful informations that are valid for most of the coronal structures.

2.2.1 *Hydrostatic scale-height*

Equation (2.12a) simply states that in hydrostatic equilibrium the pressure is balanced by gravitational force, i.e. plasma is gravitationally stratified. In this case, an important quantity can be derived from the momentum equation: the so-called hydrostatic scale-height.

If the loop axis is inclined at an angle ϑ with respect to the vertical, Eq. (2.12a) may be rewritten as

$$\frac{d}{ds}p + m_p n_e g_\odot \cos\vartheta = 0, \tag{2.13}$$

where $g_\odot$ is the gravitational acceleration along the z-axis. Since $ds\cos\vartheta = dz$ (see Fig. 2.2), the previous equation becomes

$$\frac{d}{dz}p + m_p n_e g_\odot = 0. \tag{2.14}$$

Substituting for n_e from the ideal gas law and integrating, we obtain

$$p(h) = p_0 \exp\left(-\int_0^h \frac{1}{\lambda_p(z)}\,dz\right), \tag{2.15}$$

where h is the height above the photosphere and p_0 is the pressure at the base (at $h = 0$ or $s = 0$) that may vary from one field line to another; also

$$\lambda_p(z) = \frac{2k_B T(z)}{m_p g_\odot} \tag{2.16}$$

is the (pressure) hydrostatic scale-height, that represents the vertical distance over which the pressure falls by a factor of e. Equation (2.15) shows that the pressure along a given magnetic field line drops exponentially with height. Since neighbouring structures can be characterized by very different temperatures or temperature gradients, the pressure scale-height may drastically change between adjacent loops.

In general, λ_p varies with height due to the dependence on the temperature profile $T(z)$, but, in the particular case when the temperature can be assumed

uniform along the flux tube (for instance, when the conductive flux F_C vanishes), λ_p is constant and Eq. (2.15) reduces to $p(h) = p_0 e^{-h/\lambda_p}$. Equation (2.16) may then be rewritten as a function of T as $\lambda_p \approx 5000\,T(1 + h/R_\odot)^2$, (where λ_p is measured in centimetres). A temperature of 10^4 K gives a scale-height of about 500 km near the photosphere, while a temperature of 1 MK makes $\lambda_p \approx 200$ Mm at a height of $\sim 1\ R_\odot$ above the solar surface. For relatively small loops (i.e., when $L \ll \lambda_p$), even an isobaric approximation can be used ($p(z) \approx const.$); for instance, this is quite valid for active-region loops.

2.2.2 *Heating scaling laws*

The least known term in the energy equation (2.12b) is the heating rate per unit volume $H(s)$, that crucially depends on the properties of the physical heating mechanism. Many old loop models assumed an uniform heating (e.g., Rosner et al., 1978) for the sake of simplicity. This assumption may be justified for some long-range heating mechanisms, but seems not to be consistent with the latest TRACE observations (see, e.g., Aschwanden et al., 2000).

A more realistic treatment must take into account a possible variation of the heating rate with s. The most common parametrization of the heating function considers a localisation of the heating somewhere along the loop, which can be expressed by an exponential function such as

$$H(s) = H_0 \exp\left(-\frac{s - s_0}{\lambda_H}\right), \tag{2.17}$$

where H_0 is the heating rate at the location s_0 and λ_H is the heating scale-length.

The momentum and energy equations (2.12) have numerically been solved both for the case of uniform and non-uniform heating, providing useful scaling laws, that allow to relate the maximum temperature T_{max} of the loop and the heating rate H_0 to the other parameters defining the model.

Uniform heating loops

The first historical derivation of hydrostatic solutions was carried out by Rosner et al. (1978) under the assumption of a uniform pressure p_0 (fairly valid for small loops with semi-length $L \ll \lambda_p$), and a constant heating rate H_0.

According to these authors, the conductive-loss term $(d/ds)F_C$ may be rewritten as a function of temperature in the following way:

$$\frac{d}{ds}F_C = \frac{d}{dT}F_C\frac{d}{ds}T = \frac{d}{dT}F_C\left(-\frac{F_C}{\kappa_0 T^{5/2}}\right), \tag{2.18}$$

and the energy equation (2.12b) may be rearranged to give the following temperature integral:

$$F_C\, dF_C = (R - H_0)\kappa_0 T^{5/2}\, dT, \tag{2.19}$$

where

$$R = \left(\frac{p_0}{2k_B T}\right)^2 \Lambda(T) \tag{2.20}$$

is the radiative-loss term expressed as a function of temperature and pressure through the perfect gas law.

Introducing the two auxiliary functions:

$$f_H(T) = 2\kappa_0 \int_{T_0}^{T} T'^{5/2} H_0\, dT' \tag{2.21}$$

and

$$f_R(T) = 2\kappa_0 \int_{T_0}^{T} T'^{5/2} \left(\frac{p_0}{2k_B T'}\right)^2 \Lambda(T')\, dT', \tag{2.22}$$

by assuming a thermally isolated loop, so that $F_C(T_0) = 0$, and integrating Eq. (2.19) yields

$$F_C(T)^2 = f_R(T) - f_H(T). \tag{2.23}$$

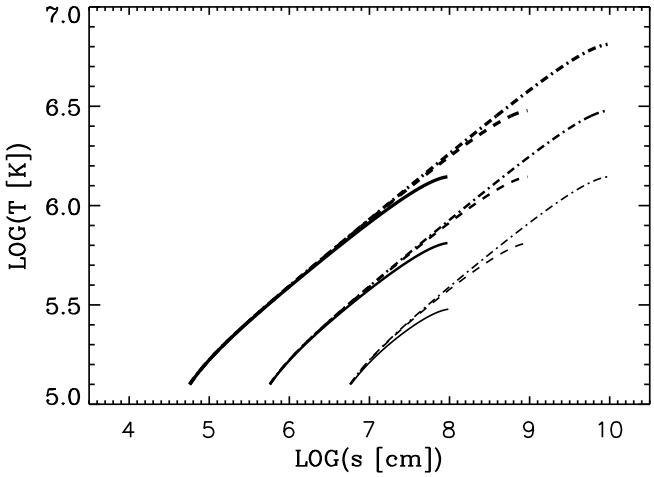

Figure 2.3: Temperature profiles derived from the analytical model of Rosner et al. (1978) for different values of the loop semi-length (1 Mm, solid lines; 10 Mm, dashed lines; 100 Mm, dot-dashed lines) and pressure (0.1, 1.0, and 10 dyn cm^{-2}, marked with thicker and thicker lines, respectively).

Substituting Eq. (2.23) into Eq. (2.18) leads to an equation that separates the length coordinate s and temperature T:

$$ds = -\frac{\kappa_0 T^{5/2}}{F_C(T)}\,dT = -\frac{\kappa_0 T^{5/2}}{\sqrt{f_R(T) - f_H(T)}}\,dT, \tag{2.24}$$

that can provide an explicit solution for the inverse of the temperature profile $T(s)$.

Rosner et al. (1978) made the further assumption of a single power-law approximation for the radiative-loss function, $\Lambda(T) \propto T^{-1/2}$ and derived from Eq. (2.24) the following analytical expression:

$$s - s_0 = 2.5 \times 10^5 p_0^{-1}(9.6 \times 10^{-16} T_{max}^3\,\psi(T) + 1), \tag{2.25}$$

where T_{max} is the loop maximum temperature and

$$\psi(T) = \arcsin(T/T_{max}) - (T/T_{max})(1 - (T/T_{max})^2)^{1/2}. \tag{2.26}$$

An example of temperature profiles, obtained from Eq. (2.25) for several loop models with different pressures and sizes, is shown in Fig. 2.3.

For $T = T_{max}$, $\psi(T) = \pi/2$ and Eq. (2.25) gives

$$s_{max} - s_0 = L \simeq 3.8 \times 10^{-10} p_0^{-1} T_{max}^3, \tag{2.27}$$

or, after rearranging,

$$T_{max} \simeq 1.4 \times 10^3 (p_0 L)^{1/3}, \tag{2.28}$$

which is the well known RTV scaling law for the apex temperature of a hydrostatic loop with constant pressure p_0. By using equations (2.23), (2.28) and the fact that the conductive flux vanishes at the temperature maximum ($F_C(T_{max}) = 0$), it is possible to eliminate T_{max} in order to obtain:

$$H_0 \simeq 9.8 \times 10^4 p_0^{7/6} L^{-5/6}, \tag{2.29}$$

that represents the RTV scaling law for the heating term.

These scaling laws have been applied mainly to soft X-ray loops, that are sufficiently hot to support the assumption of constant loop pressure, and seem to be roughly consistent with observations. The agreement is somewhat surprising also in the case of extreme coronal structures (e.g., flare loops), since the assumptions upon which the model is based (particularly, $v \approx 0$) are generally thought to be invalid in these cases (see Rosner et al., 1978). Full numerical solutions of the hydrostatic equations (e.g., Wragg & Priest, 1982) show that the RTV scaling laws are accurate for short loops, while, for sufficiently long loops, such as those for which only footpoints can be observed in X-ray images, the temperature may be up to a factor of two lower than that predicted by the scaling laws.

Non-uniform heating loops

Serio et al. (1981) introduced two important generalisations to the simple model of Rosner et al. (1978): i) the application of a non-uniform heating; ii) the consideration of the variation with height of the plasma pressure. They assumed the heating as concentrated near the loop footpoints with an exponential dependence

on the loop length coordinate s, Eq. (2.17) with $s_0 = 0$, and pressure varying as $p(s) = p_0 \exp(-s/\lambda_p)$ with $\lambda_p = const.$

The inclusion of these two important effects leads to a significant modification of the RTV scaling laws, that become:

$$T_{max} \approx 1.4 \times 10^3 (p_0 L)^{1/3} \exp\left(-0.08\frac{L}{\lambda_H} - 0.04\frac{L}{\lambda_p}\right), \tag{2.30}$$

$$H_0 \approx 9.8 \times 10^4 p^{7/6} L^{-5/6} \exp\left(0.78\frac{L}{\lambda_H} - 0.36\frac{L}{\lambda_p}\right). \tag{2.31}$$

These scaling laws deviate from those derived by Rosner et al. (1978) mainly for short heating scale-lengths, say when $\lambda_H \ll L$. For instance, taking $L/\lambda_H = 4$ yields an increase of ~ 2.6 in the loop base pressure and of ~ 22.6 in the heating rate.

2.3 THERMAL STABILITY OF CORONAL LOOPS

A fundamental topic concerns the stability of the solutions for the hydrodynamic equations. Hydrostatic solutions, or more generally time-independent solutions, assume an equilibrium state that can be either stable or unstable, depending on whether the system returns or not in the same initial state after perturbation. For instance, solutions that are generally stable can become suddenly unstable under particular conditions or for particular values of the temperature and density, i.e., they can develop an instability that breaks the equilibrium and forces the system to reconfigure into a new stationary state.

The most considerable source of instability of interest for coronal loop models is the so-called radiatively-driven thermal instability (see, e.g., Parker, 1953; Field, 1965) that occurs when thermal conduction is not sufficient to balance the radiative losses somewhere along a loop, leading to a local catastrophic plasma cooling.

It is possible to found analytical conditions for the thermal stability of loops as follows. When the pressure is assumed uniform, the time-dependent energy equation for a pure radiatively cooling loop may be written as:

$$m_p n_e \frac{\partial}{\partial t}(c_p T) = H - n_e^2 \Lambda(T), \tag{2.32}$$

where both the conductive-loss term and flows have been neglected. On taking $\Lambda(T) \approx \chi T^{\alpha}$, Eq. (2.32) then becomes:

$$m_p c_p \frac{\partial}{\partial t} T = h - \chi \frac{p_0}{2k_B} T^{\alpha-1}, \tag{2.33}$$

where $h = H/n_e$ is the heating rate per particle and n_e has been expressed in terms of the constant pressure p_0 and temperature by the ideal gas law. The heating term h may be constrained from the equilibrium state, for which $\partial/\partial t = 0$:

$$h = \chi \frac{p_0}{2k_B} T_0^{\alpha-1}, \tag{2.34}$$

where T_0 is the equilibrium temperature. Thus, substituting for h from Eq. (2.34), Eq. (2.33) yields

$$m_p c_p \frac{\partial}{\partial t} T = \chi \frac{p_0}{2k_B} T_0^{\alpha-1} \left(1 - \frac{T^{\alpha-1}}{T_0^{\alpha-1}}\right), \tag{2.35}$$

that is an evolutionary equation from which the stability conditions for a pure radiatively cooling loop can easily be derived.

If $\alpha < 1$, a small decrease in temperature ($T < T_0$) makes the right-hand side of equation (2.35) negative, so that $(\partial/\partial t)T < 0$ and the perturbation continues to act, a thermal-instability develops that cools the loop until a new equilibrium is reached, with a cooler and consequently higher density structure. It can be seen from Fig. 2.1 that $\alpha < 1$ for temperatures slightly exceeding 10^5 K, so that most of the coronal loops would undergo such a radiatively-driven thermal instability in the case of insufficient thermal conduction and heating. The time-scale of

the cooling, i.e., the radiative cooling-time τ_{rad}, follows from Eq. (2.35), after replacing $(\partial/\partial t)T$ with T_0/τ_{rad}:

$$\tau_{rad} \simeq \frac{2k_B c_p m_p}{\chi p_0 T_0^{\alpha-2}}. \tag{2.36}$$

Usually, thermal instability is prevented from taking place by the efficiency of thermal conduction along the magnetic field lines. When conductive losses predominate, the energy equation may be written as

$$m_p c_p \frac{\partial}{\partial t} T = h + \frac{2k_B T}{p_0} \frac{\partial}{\partial s} \left(\kappa_0 T^{5/2} \frac{\partial}{\partial s} T \right), \tag{2.37}$$

from which a conductive cooling-time, τ_{cond}, may be defined:

$$\tau_{cond} \simeq \frac{c_p m_p p_0 L^2}{2k_B \kappa_0 T_0^{7/2}}, \tag{2.38}$$

with the approximations $(\partial/\partial t)T \approx T_0/\tau_{cool}$ and $\partial/\partial s \approx 1/L$. If the conductive cooling-time is shorter than the radiative cooling-time, i.e. $\tau_{cond} < \tau_{rad}$, equations (2.36) and (2.38) give an alternative condition for the stability of the loop:

$$L < L_{max} = \left(\frac{4k_B^2 \kappa_0 T_0^{11/2-\alpha}}{\chi p_0^2} \right)^{1/2}. \tag{2.39}$$

When L exceeds the value of L_{max}, the plasma is thermally unstable. Some numerical values of radiative cooling times τ_{rad} and conductive cooling times τ_{cond} for typical coronal conditions are listed in Table 2.2.

Several studies of coronal loop heating (Serio et al., 1981; Antiochos et al., 1999, 2000; Karpen et al., 2001; Karpen & Antiochos, 2008; Klimchuk et al., 2009) showed that loops for which the temperature maximum is located below the loop-top are in general thermally unstable and the instability generally occurs whenever steady or quasi-steady heating is highly concentrated at low coronal heights in both the legs of a loop, with a scale-length that is shorter than a critical fraction of the loop semi-length, either for dipped or undipped flux-tubes.

Table 2.2: Radiative and conductive cooling times (computed for a loop with semi-length $L = 50$ Mm and expressed in seconds) for typical coronal densities (n_e) and temperatures (T).

n_e (cm^{-3})		T (K)				
		10^5	5×10^5	10^6	5×10^6	10^7
10^8	τ_{rad}	550	1.0×10^4	3.0×10^4	2.7×10^5	8.6×10^5
	τ_{cond}	3.0×10^5	5300	940	17	3
10^9	τ_{rad}	55	1000	3000	2.7×10^4	8.6×10^4
	τ_{cond}	3.0×10^6	5.3×10^4	9400	170	30
10^{10}	τ_{rad}	5.5	100	300	2700	8600
	τ_{cond}	3.0×10^7	5.3×10^5	9.4×10^4	1700	300

The most relevant effect of thermal non-equilibrium on a loop structure is the triggering of plasma condensation where the imbalance between heating, thermal conduction, and radiation occurs.

The phenomenon of plasma condensation is well known and extensively described in the literature (e.g., Antiochos et al., 1999, 2000; Karpen et al., 2001, 2006; Karpen & Antiochos, 2008; Klimchuk et al., 2009; Müller et al., 2003, 2004; Testa et al., 2005). Recently, it has also been observed in coronal non-flaring loops (e.g., O'Shea et al., 2007).

The steep temperature rise and overpressure caused by the concentration of the heating injection at the base of the loop drives the upward expansion, known as chromospheric evaporation (see, e.g., Antiochos & Sturrock, 1978), that produces an increase of density and consequently of radiative losses throughout the loop, even in the upper section where the heating is weaker.

The increase in radiative losses, that cannot be balanced by the energy supply and thermal conduction, eventually leads to a catastrophic cooling, down to chromospheric temperatures, of the material located close to the loop apex and, consequently, to the formation of a region of low-temperature and high-density plasma, i.e. a condensation (e.g., Antiochos et al., 1999). If the heating-rate in

the two legs of the loop is asymmetric, the blob of cool and dense plasma starts moving slowly towards the less heated footpoint, because of the pressure imbalance between the two legs of the loop, and finally sinks onto the chromosphere.

Since thermal non-equilibrium and the cycle of chromospheric evaporation, plasma condensation and sinking in footpoint-heated loop models may have relevant effects on the radiation spectrum emitted by the loop, as well as on the temperature distribution of plasma, it seems reasonable to consider that its occurrence could help in reproducing, at least to some extent, the observations previously described, in particular the EUV observations of warm loops.

3

THE NUMERICAL MODEL

3.1 THE HYDRODYNAMIC CODE

The numerical simulations presented in this work are performed by using the $1D$ hydrodynamic code ARGOS (Adaptively Refined Godunov Solver; see, e.g., MacNeice et al., 2000; Antiochos et al., 1999).

In order to solve the standard set of hydrodynamic equations (Eq.s 2.11) and to evolve the solution in time, ARGOS uses a second-order Godunov scheme with a MUSCL (Monotone Upstream-centered Schemes for Conservation Laws, Van Leer, 1979) flux limiter. In this method, the conserved variables (i.e., mass, momentum, and energy) are considered as piecewise constants over the mesh cells at each time step t_i and the time evolution is implicitly determined by the exact solution of the Riemann problem at the inter-cell boundaries, involving both the state of the system at time t_i and the successive one at $t_{i+1} = t_i + \Delta t$ (e.g., Hirsch, 1990). It is widely believed that high order Godunov schemes are the most robust methods for numerically solving one-dimensional fluid flow problems, like, e.g., non-turbulent, compressible coronal loop plasma motions in which steep gradients and/or discontinuities are likely to develop (Antiochos et al., 1999). The MUSCL limiter is used to avoid the spurious numerical oscillations that would otherwise occur in case of sharp changes in the solution domain.

To resolve evolving regions of steep gradients, such as the thin chromospheric-coronal transition regions at the base of the loop, ARGOS employs a fully adaptive grid by using the Parallel Adaptive Mesh refinement package PARAMESH (MacNeice et al., 2000). This is critically important for simulations of this type. Unless these regions are resolved, the plasma energetics and dynamics cannot be accurately computed. To further emphasize this point, we note that moving chromospheric-coronal interfaces can possibly form at locations other than the loop footpoints, such as at the sides of coronal condensations.

PARAMESH builds a hierarchy of subgrids to cover the whole computational domain, with spatial resolution varied to satisfy the demands of the application. These subgrid blocks form the nodes of a tree structure. Each grid block has a logically Cartesian mesh, and the index ranges are the same for every block. In this case, we use one-dimensional subgrid blocks with 20 grid cells and two guard cells at each end of the subgrid. When a subgrid block needs to be refined, it is split into two new blocks having their own 20 cell subgrids and covering the same coordinate range as their parent, but with a mesh spacing one half that of the parent's mesh spacing. If consistent with resolution requirements, then PARAMESH also will "derefine" two adjacent blocks, i.e., merge them into a single block with twice the mesh spacing. PARAMESH provides routines that manage the necessary communication between subgrid blocks.

The criterion for refining and derefining the numerical grid is related to the variations of the plasma density between neighbouring cells. Density is found to be the best quantity to use in determining the refinement level because it exhibits a strong spatial variation both in the corona and transition region, where pressure is approximately constant, and in the chromosphere, where temperature is kept uniform.

The refinement criterion used by PARAMESH is very simple. At each grid cell i, the error in density determination is computed:

$$\epsilon_i = |\rho_i - \rho_{i-1}| / \max(\rho_i, \rho_{i-1}), \tag{3.1}$$

and, for each subgrid block, the maximum value inside the block is found:

$$\epsilon_{max} = \max(\epsilon_0, \ldots, \epsilon_{21}). \tag{3.2}$$

A guard cell is added at each end of the subgrid (so, $i = 0, \ldots, 21$) to enable refinement of a solution. If ϵ_{max} exceeds 0.25, meaning that somewhere in the subgrid block the density varies at least by 25%, then that subgrid block is refined. On the contrary, if ϵ_{max} is less than 0.05 on a couple of neighbouring subgrid blocks, then they are derefined, provided that the spatial resolution of the new parent block is below the refinement threshold.

PARAMESH allows for 12 levels of refinement. Level 1 means that the whole computational domain is covered by a unique subgrid block, so that the cell size is $\Delta x = D/20$, where D is the total length of the computational domain. A refinement level n therefore has a cell size given by $\Delta x = 2^{1-n}D/20$. The initial domain is uniformly refined at level 6, so the initial cell size is $\Delta x = 0.0015625D$. Subgrids refined at level 12 have a cell size that is $2^6 = 64$ times finer. In the simulations presented here, the maximum refinement level corresponds to a minimum grid spacing of ~ 5 km.

The rapid transients, fast dynamics, and steep thermal gradients that characterize the loop plasma evolution may also have the effect to make the classical conductive flux predicted by the Spitzer formula ($F_C = \kappa_0 T^{5/2}|\nabla T|$) locally larger than the physically possible one (Klimchuk, 2006). In the cases of exceptionally high temperature and/or exceptionally low density, such as during the earliest phase of an impulsive heating event, the real heat flux saturates at a magnitude given by

$$F_S = c\frac{3}{2}\frac{k_B^{3/2}}{m_e^{1/2}} n_e T^{3/2}, \tag{3.3}$$

where c is a flux limiter constant that is set to $1/6$ (see Luciani et al. 1983; Karpen & DeVore 1987). ARGOS considers both the classical and saturated conduction regimes. In order to allow a smooth transition between them, the total heat flux used to compute the conductive-loss term ($C = \partial F_T/\partial s$) is set equal to:

$$F_T = \frac{F_C F_S}{\sqrt{F_C^2 + F_S^2}}, \tag{3.4}$$

which reduces to F_C when $|F_C| \ll |F_S|$ and to F_S when $|F_C| \gg |F_S|$.

The optically thin radiative-loss function $\Lambda(T)$ used by ARGOS for these calculations (see Fig. 3.1) is that given by Klimchuk et al. (2008), with the exception that there is a T^3 dependence below 0.1 MK to account approximately for optical depth effects. It consists in a piecewise continuous form based on atomic physics calculations with twice the coronal elemental abundances of Meyer (1985). The

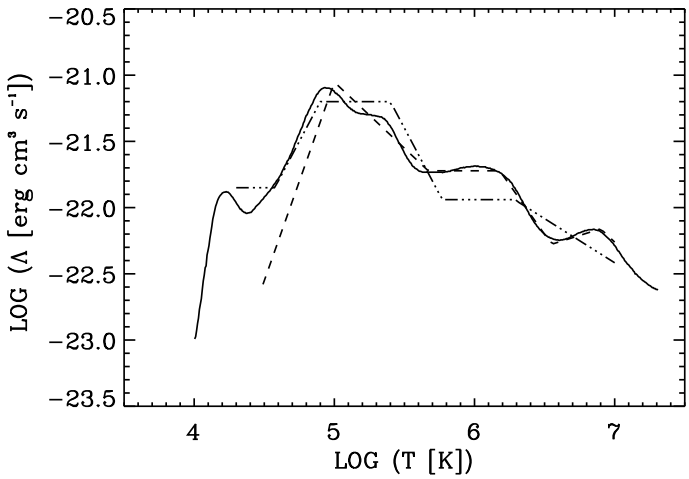

Figure 3.1: Optically thin radiative-loss function deduced from atomic physics calculations with twice the coronal elemental abundances of Meyer (1985, solid line) and the corresponding piecewise analytical approximation used by ARGOS (dashed line, see Klimchuk et al., 2008). Also shown, for comparison purposes, is the analytical radiative-loss function used in Rosner et al. (1978, triple-dot-dashed line).

highest temperature range of the loss function is dominated by thermal bremsstrahlung (Cox & Tucker, 1969).

A well-known source of possible numerical problems comes from the exponentially growing radiative-loss rate inferred for the deep chromosphere under the assumption of optically thin losses. In the Sun's chromosphere the radiative losses are limited by radiative transfer that is not included in our model. ARGOS addresses this problem assuming that: i) the radiative-loss coefficient identically vanishes for $T \leq 29500$ K; ii) the losses no longer increase with n^2 for densities larger than 6×10^{11} cm^{-3}. In particular, the former assumption implies that radiative losses for the H I Ly-α in the optically thin approximation (corresponding to the secondary peak centred at $\log T \simeq 4.1$ in the radiative-loss function of Fig. 3.1) are not included in our calculations.

3.2 SIMULATIONS PLAN

3.2.1 *Loop model geometry*

The loop considered in this work consists of three distinct sections: an arched coronal segment with a footpoint-to-apex half length of $L = 40$ Mm and two 60 Mm long chromospheric regions attached to each end of the coronal arch (see Fig. 3.2). The total length of the computational domain is $D = 200$ Mm. Note that we chose the length of the coronal part of the flux-tube to model typical active region loops as observed, for instance, by TRACE. The cross-section area is assumed to be constant, consistent with most observations of both EUV and X-ray loops (e.g., Klimchuk, 2000; López Fuentes et al., 2006).

For convenience, the geometry of the coronal part of the loop is given by the following analytic form:

$$z(s') = h\left(1 - \frac{1-\sqrt{1-(s'/b)^2}}{1-\sqrt{1-(L/b)^2}}\right), \tag{3.5}$$

where z is the height above the chromosphere, s' the curvilinear coordinate along the field lines ($s' = 0$ at the loop top and $s' = \pm L$ at the footpoints), h the loop apex height, and b is defined as:

$$b = \frac{L-h}{\sqrt{1-2h/L}}. \tag{3.6}$$

Here $h \simeq 15$ Mm. The component of solar gravity parallel to the loop is calculated by simply differentiating Eq. (3.5):

$$g_{\parallel}(s') = -g_{\odot}\frac{dz}{ds'} = g_{\odot}\frac{h}{b^2(1-\sqrt{1-(L/b)^2})}\frac{s'}{\sqrt{1-(s'/b)^2}}, \tag{3.7}$$

where $g_{\odot} = 2.7 \times 10^4$ cm s^{-2}. Note that $dz/ds' = \pm 1$ for $s' = \pm L$.

The two deep chromospheric regions at both ends of the coronal segment act as a mass reservoir. Each of them consists of a straight, horizontal segment where $g_{\parallel} = 0$, a quarter-circle where $g_{\parallel}$ increases from zero to $g_{\odot}$, and a straight vertical

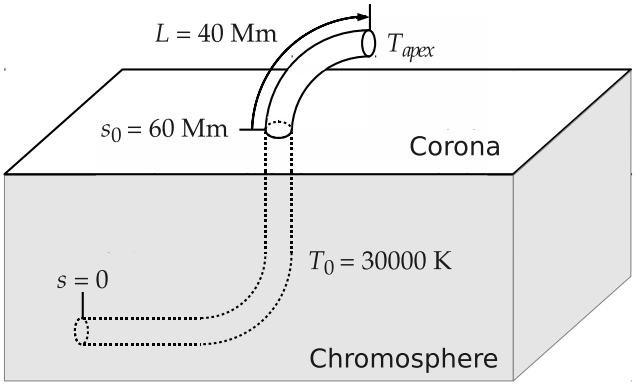

Figure 3.2: Schematic representation of the simulated loop. It consists in an arched magnetic flux-tube with coronal semi-length $L = 40$ Mm. At each footpoint (s_0), there is a 60 Mm long chromospheric segment maintained at a constant temperature of 30000 K.

tube, for which $g_{\parallel} = const. = g_{\odot}$. The plasma density is assumed uniform within the horizontal segment, then it scales with height according to the hydrostatic equilibrium law.

Throughout each simulation, the chromospheric sections of the loop are maintained at a nearly constant temperature $T_0 = 30000$ K by the radiative-loss function that falls drastically to zero over a 500 K temperature interval below T_0 (see Fig. 3.1). The same radiative-loss function is used for the cold condensations that possibly form and move along the coronal part of the loop during its evolution and are bounded by thin transition regions that closely resemble the classical transition regions at the loop footpoints. Although both chromosphere and condensations are treated in high simplified way, their interaction with the rest of the loop is rigorously modelled. In particular, the mass and energy exchange due to chromospheric evaporation and plasma condensation is accurately treated. A more realistic approach to the modelling of the energy balance in the optically thick chromosphere can be found, for instance, in Anzer & Heinzel (2000).

The only boundary conditions imposed in our simulations are those at the two end-points (rigid-wall, fixed temperature). Note that the edges of the computational domain are located many gravitational scale-heights below the chromospheric footpoints ($\lambda_p \simeq 2$ Mm for a temperature $T = 30000$ K, see Eq. 2.16) to minimise their effect on the simulated plasma evolution.

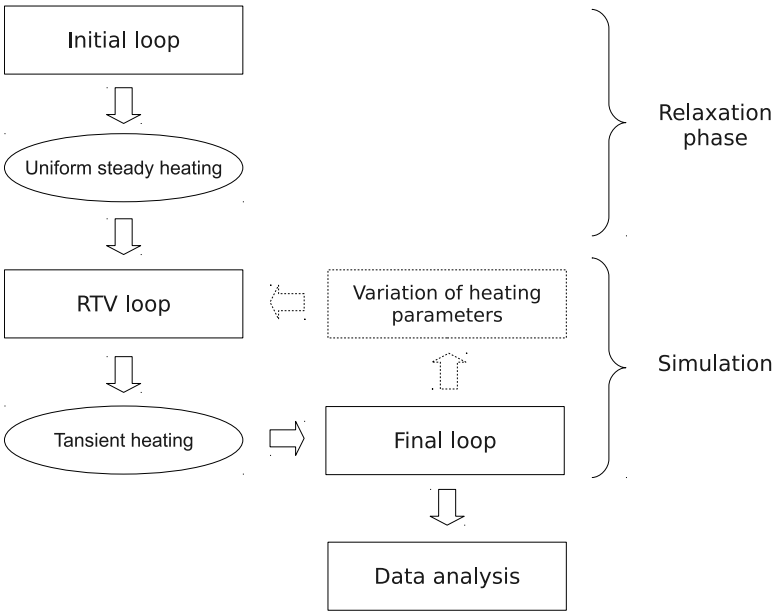

Figure 3.3: Flowchart showing the different steps of a simulation.

3.2.2 *Initial state*

Each simulation begins by allowing the loop to relax to a quasi-static equilibrium state under the action of a spatially uniform, temporally constant background heating, $H_{base} = 2 \times 10^{-5}$ erg cm^{-3} s^{-1} (see Fig. 3.3). The choice for the value of H_{base} is made according to the RTV hydrostatic scaling law for the heating term (Eq. 2.29) in order to get a loop apex temperature of about 0.75 MK at the end of the relaxation phase. At this stage, the loop structure is close to that of a steady loop as in Rosner et al. (1978). Figure 3.4 shows the loop temperature and density profiles at the beginning and at the end of the relaxation phase, together with a comparison between our initial steady-state model and the corresponding one obtained from Eq. (2.25) according to Rosner et al. (1978).

3.2.3 *Heating regimes*

Once the initial quasi-static state is achieved, we turn on, at $t = 0$ s, an additional heating term within the coronal part of the loop only; in the same loop region,

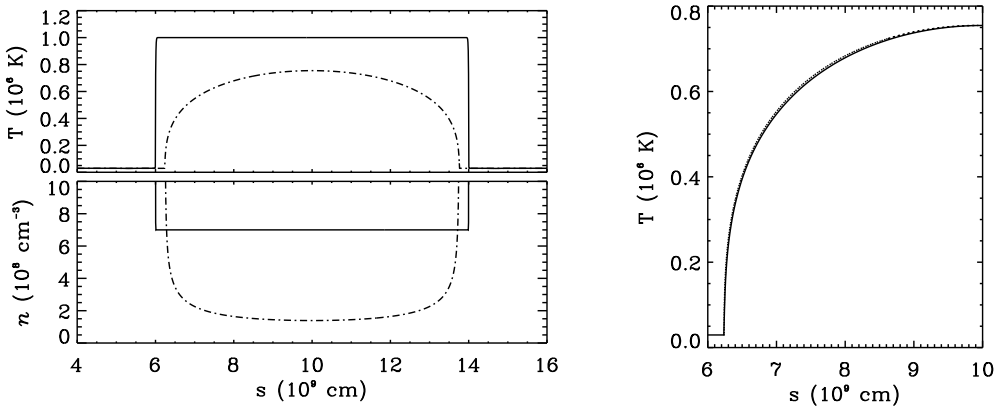

(a) (b)

Figure 3.4: (a) Instantaneous profiles of the loop temperature (top panel) and density (bottom panel) vs. the curvilinear coordinate s, at the beginning of the relaxation phase (solid line) and after the achievement of the quasi-static equilibrium state (dot-dashed line). (b) A comparison between the half-loop temperature profile of our initial equilibrium state (solid line) and the corresponding one obtained with the analytical approach of Rosner et al. (1978, dotted line).

the uniform background heating H_{base} applied to produce the initial equilibrium is turned off and remains off for the rest of the simulation. Conversely, in the chromospheric segments of the loop, the H_{base} heating is held invariant during the simulation, although it has a little influence on the loop hydrodynamics owing to the high density in the chromosphere.

For convenience, the additional heating rate applied to the corona, $H(s,t)$, is assumed to be a separable function of space and time:

$$H(s,t) = F(s) \cdot G(t) \quad (\text{erg cm}^{-3}\ \text{s}^{-1}). \tag{3.8}$$

We carried out simulations examining all the possible combinations among two kinds of heating spatial distributions, i.e. uniform[1] or localized near to the loop footpoints, and two kinds of temporal distribution, i.e. steady or impulsive.

1 Note that when we say *uniform*, we refer to the loop coronal segment only, since in this case the chromospheric and coronal heating rates are indeed different.

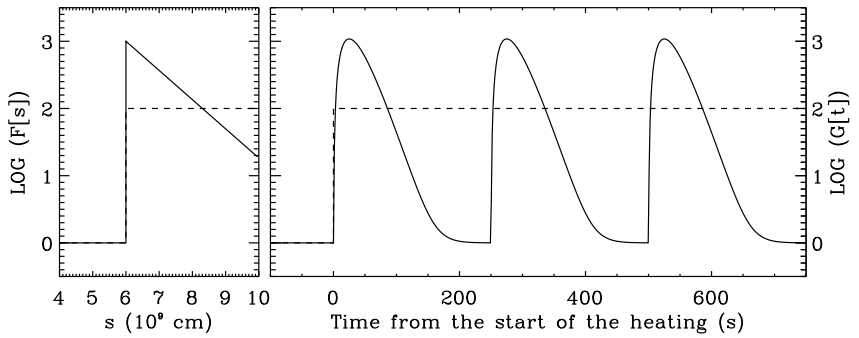

Figure 3.5: *Left:* Spatial dependence of the heating-rate function, $F(s)$, plotted versus the curvilinear coordinate s, for localised (solid line) and uniform (dashed line) heating. *Right:* Temporal dependence of the heating-rate function, $G(t)$, as a function of time, in the impulsive ($t_C = 250$ s, solid line) and steady (dashed line) heating cases. Note that the values are reported in adimensional units.

In the uniform heating cases, we have simply $F(s) = 1$. In the localized heating cases, the heating rate has a maximum at the loop footpoint, then exponentially decreases in the corona with a fixed scale-length $\lambda = 10$ Mm (see Fig. 3.5, left panel); the location and scale-length of the energy deposition are consistent with those deduced from TRACE observations (e.g., Aschwanden et al., 2000, 2001). We also consider the possibility of an asymmetric energy deposition between the two footpoints of the loop, since real coronal loops do not appear to be symmetric. The spatial dependence of heating is given in these cases by the following expression:

$$F(s) = \begin{cases} \exp\left(-\dfrac{s - s_0}{\lambda}\right), & s_0 \leq s \leq (s_0 + L), \\ f \exp\left(-\dfrac{s_0 + 2L - s}{\lambda}\right), & (s_0 + L) < s \leq (s_0 + 2L), \end{cases} \tag{3.9}$$

where $s_0 = 60$ Mm is the position of the left footpoint and $f = 0.75$ is the constant ratio of the localized heating at the right footpoint to that at the left one (i.e., the right footpoint of the loop is less intensely heated).

The temporal dependence of the heating in the steady cases can be expressed as $G(t) = H_S$, where H_S is the constant heating rate applied to the corona.

In the impulsive cases, we inject into the coronal part of the loop a multitude of energy pulses, or nanoflares, with constant cadence, duration, and energy amplitude; we model each nanoflare with a Maxwellian function, such that the energy release during a single event has a steep rise, followed by a more gradual decrease. Specifically:

$$G(t) = H_I \frac{1}{2\tau^3} t'^2 \exp\left(-\frac{t'}{\tau}\right), \quad t' = t \bmod t_C, \tag{3.10}$$

where H_I gives the volumetric heating dissipated per nanoflare event, τ is a characteristic parameter related to the duration of the energy pulses (here always equal to 12.5 s), t_C is the cadence time between two consecutive pulses, and t' measures the time from the start of each nanoflare (see Fig. 3.5, right panel).

The values of H_S and H_I are chosen to satisfy:

$$A \int_{s_0}^{s_0+2L} ds \int_0^{t_C} H(s,t)\, dt = H_P \quad \text{(erg)}, \tag{3.11}$$

where A is the constant cross-sectional area of the loop and H_P is the total energy deposited into the loop in a time interval equal to t_C (i.e., the energy dissipated per nanoflare event in the impulsive heating cases). In the steady heating cases, a value of $t_C = 250$ s is used to compute H_S, even if in these cases a cadence time is clearly not defined. Table 3.1 lists the values of the parameters adopted in the simulations performed for this work.

The values for t_C are fixed taking into account the characteristic cooling time of the loop, τ_{cool}. We estimated τ_{cool} using the expression given, for instance, by Serio et al. (1991):

$$\tau_{cool} \simeq 120 \frac{L_9}{\sqrt{T_7}}, \tag{3.12}$$

where L_9 is the loop semi-length in unit of 10^9 cm and T_7 the maximum temperature of the loop in unit of 10^7 K. For a loop with $L = 40$ Mm and an apex temperature $T_{max} = 2$ MK, it results $\tau_{cool} \approx 1000$ s. Here we report results obtained with t_C ranging from 250 s $\simeq \tau_{cool}/4$ to 2000 s $\simeq 2\,\tau_{cool}$.

Table 3.1: Parameters of the simulations.

Heating regime	Run #	t_C (s)	H_P[a] (10^{24} erg)	H_{max}[b] (erg cm^{-3} s^{-1})	$\langle H \rangle$[c] (10^{21} erg s^{-1})
UNIFORM STEADY	1	—	1	5×10^{-4}	4
UNIFORM IMPULSIVE	2	250	1	2×10^{-3}	4
	3	500	1	2×10^{-3}	2
	4	1000	1	2×10^{-3}	1
	5	2000	1	2×10^{-3}	0.5
LOCALISED STEADY	6	—	1	4×10^{-3}	4
LOCALISED IMPULSIVE	7	250	0.125	2.75×10^{-3}	0.5
	8	250	0.25	5.5×10^{-3}	1
	9	250	0.5	1.1×10^{-2}	2
	10	250	1	2.2×10^{-2}	4
	11	250	2	4.4×10^{-2}	8
	12	250	4	8.8×10^{-2}	16
	13	500	0.25	5.5×10^{-3}	0.5
	14	500	0.5	1.1×10^{-2}	1
	15	500	1	2.2×10^{-2}	2
	16	500	2	4.4×10^{-2}	4
	17	1000	1	2.2×10^{-2}	1
	18	1000	4	8.8×10^{-2}	4
	19	2000	1	2.2×10^{-2}	0.5
	20	2000	8	1.76×10^{-1}	4

[a] Total energy per pulse, or, in the steady cases, total energy deposited into the loop in a time interval equal to $t_C = 250$ s.

[b] Maximum heating rate per unit volume; note that in the steady heating cases this is equal to H_S.

[c] Average amount of energy supplied to the loop per unit time.

Table 3.2: Recent hydrodynamic numerical simulations of coronal loops compared with our model.

	L (Mm)	T_{apex} (MK)	t_C/τ_{cool}	λ/L
Our model	40	0.75	2, 1, 1/2, 1/4	1/4
Karpen & Antiochos (2008)	142	2.9	1, 1/4	0.04, 0.007
Testa et al. (2005)	100	3, 10	1/2, 1/4	1/3, 1/5, 1/10
Müller et al. (2004)	50	0.7	Steady	0.12, 0.1, 0.06, 0.04
Müller et al. (2003)	5	0.7	Steady	0.3, 0.25, 0.2, 0.15, 0.1

We also consider different values for H_P in order to vary the amount of energy supplied to the loop by the sequence of heating pulses and investigate the related effects on plasma hydrodynamics.

Note that in the following chapters we will present results only for some representative cases, focusing the most important features. Figures relevant to runs that will not be explicitly discussed are collected together in Appendix A.

3.2.4 *Differences and analogies with previous works*

Table 3.2 summarizes the initial conditions and the key parameters of our hydrodynamic simulations of loop heating as compared with those of some other previous works.

Our loop model is very similar, in terms of loop semi-length and initial apex temperature, to that treated by Müller et al. (2004), even though they focused the plasma response to the steady heating only. In their works, they considered the heating localised at the loop footpoints with different scale-lengths.

Testa et al. (2005) analysed the effects of impulsive, footpoint-localised heating, by varying either the pulse cadence time, the pulse energy, and the heating scale-length. They modelled a flux-tube nearly twice longer than ours, starting from initial temperatures higher than $T_{apex} \sim 3$ MK and run simulations lasting for up to 10000 s, since they were interested to find solutions corresponding to hot loops in steady-state conditions over long time-scales.

Karpen & Antiochos (2008) studied the dynamic behaviour of a loop model under the action of impulsive heating strongly localised near the loop footpoints. They considered a slightly dipped flux-tube nearly 4 times longer than ours, with an initial apex temperature of about 3 MK; moreover, they explored several parameters, like the pulse cadence, the pulse duration, the heating scale-length, and the presence or not of a background uniform heating, focusing the formation and the evolution of plasma condensations, in order to investigate possible links with prominence formation processes.

With respect to these works, we analysed all the possible combinations among steady or impulsive, uniform or footpoint-localised heating. In particular, we made a comprehensive survey of the cadence and magnitude of impulsive coronal heating and investigated the influence of these parameters on the dynamic behaviour of the loop by considering repetition times both shorter and longer than the characteristic loop cooling time and by varying the amount of energy supplied by a single nanoflare in a relatively large range of values (see Table 3.1). Moreover, we extended our simulations up to 30000 s to examine the long-term effects of the different heating regimes on the loop model evolution.

4

RESULTS AND DISCUSSION: 1. PLASMA DYNAMICS

4.1 LOOP TEMPORAL EVOLUTION

4.1.1 *Uniform heating*

Figure 4.1 shows the initial part of the temporal evolution of the plasma temperature, density, and velocity averaged along the upper 3/4 of the loop coronal part (see, e.g., Patsourakos & Klimchuk, 2005) for the uniform heating runs characterized by the same mean dissipated energy (run 1 and 2).

In the steady case (run 1), after the start of the additional heating, the spatially-averaged temperature rises rapidly (during the first $\sim$ 10 minutes) to a maximum of about 2.1 MK. In this phase, an intense heat flux drives a strong chromospheric evaporation with upflow velocities reaching $\sim$ 35 km s^{-1}. In the next hour, the temperature slightly decreases and stabilizes to a value of about 1.9 MK. The density increases more gradually, reaching a maximum value of about 10^9 cm^{-3} in the first hour after the onset of the heating. Note that the material continues to evaporate into the loop also during the slight cooling that follows the steep temperature rise. After this initial dynamic phase due to the abrupt onset of the heating, the loop model settles into a new quasi-static equilibrium state, characterized by nearly constant temperature, density and velocity. Long time after the onset of the additional heating, the averaged plasma temperature and density for this state are consistent with the RTV hydrostatic scaling laws (see Eq. 2.28).

In the impulsive case (run 2), the average loop temperature, density, and velocity behave as the corresponding ones obtained for the steady case (run 1), besides the small oscillations, lower then 10%, due to the sequence of energy pulses. This is expected when the cadence of nanoflares is very rapid as compared with the loop plasma radiative cooling time (see, e.g., Walsh et al., 1997; Testa et al., 2005; Klimchuk, 2006). In this case, in fact, the high frequency of

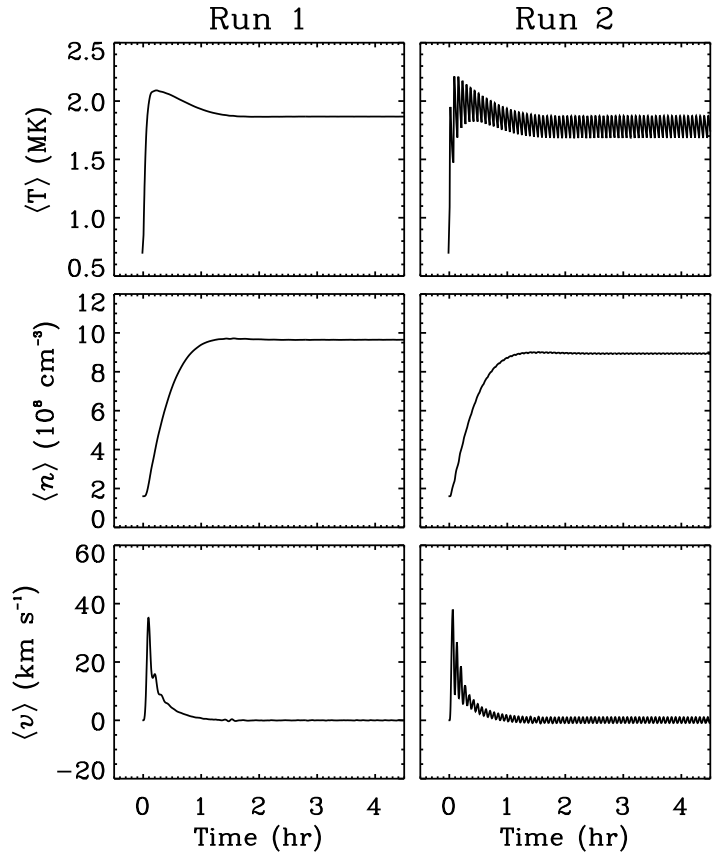

Figure 4.1: Initial part of the temporal evolution of the loop model temperature (top panels), density (middle panels), and velocity (bottom panels), averaged over the upper 3/4 of the loop coronal part, for run 1 (left panels) and 2 (right panels).

the energy pulses prevents a significant cooling of the plasma, so that the loop effectively perceives the pulsed heating as in quasi-steady situation. In our cases a cadence time equal to $\tau_{cool}/4$ already gives a nearly steady heating situation.

The evolution of the spatially-averaged plasma parameters for the impulsive heating cases in which the cadence time is longer than the plasma cooling time (runs 3, 4, and 5; see Fig. 4.2) confirms this explanation. In this cases, after the initial dynamic phase (characterized by a velocity peak of ~ 45 km s^{-1}), the temperature in the upper part of the loop coronal region shows pronounced oscillations, whose amplitude increases with t_C, since there is enough time between pulses for the plasma to cool down and sink downwards onto the chromosphere

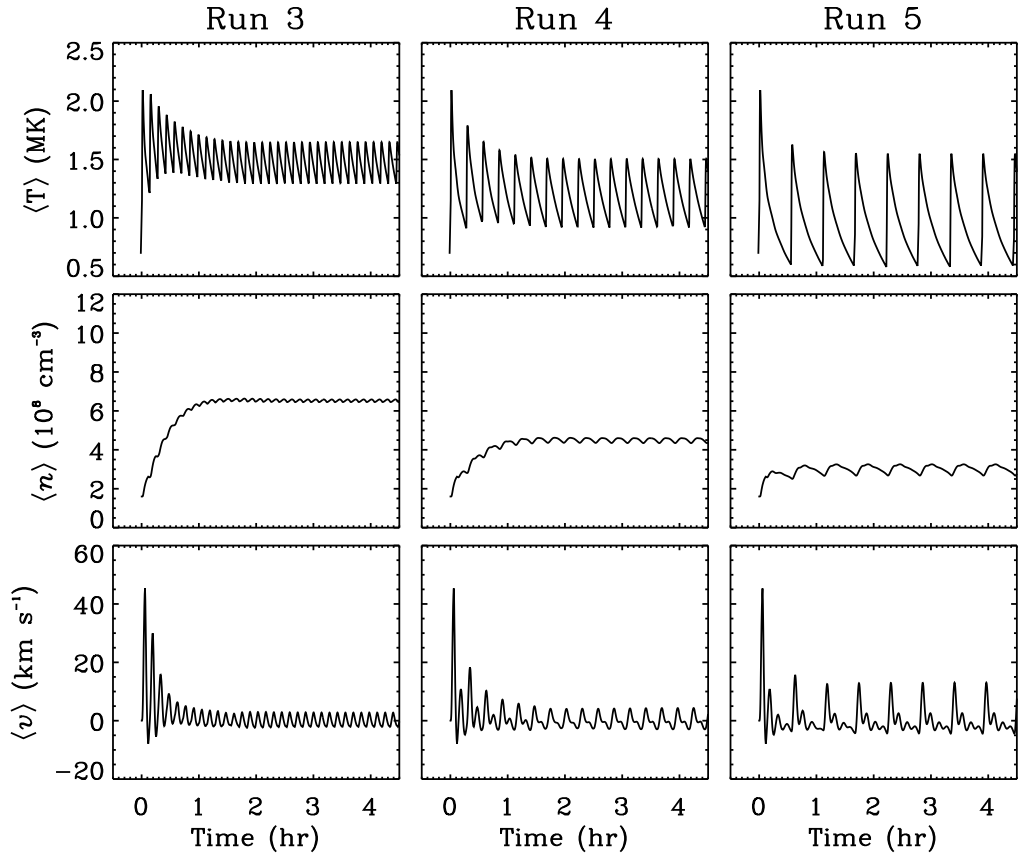

Figure 4.2: Same as in Fig. 4.1, for run 3 (left panels), 4 (middle panels), and 5 (right panels).

(as confirmed by the moderate downward velocities of the plasma noticed in between the pulses). Density has small variations and its time-averaged value decreases with increasing t_C well after the onset of the additional heating. On the contrary, velocity shows strongly damped oscillations with a rather high peak at the beginning of each energy pulse, whose amplitude depends slightly on the pulse cadence time.

In particular, we note that, during every nanoflare, the variations of temperature and density are not simultaneous, but there is a time lag (of about $t_C/2$) between the time at which the maximum temperature is reached (corresponding to the maximum of the heating-rate; see Fig. 4.3) and the time at which coronal sinking starts. This response of plasma to the impulsive heating is well known

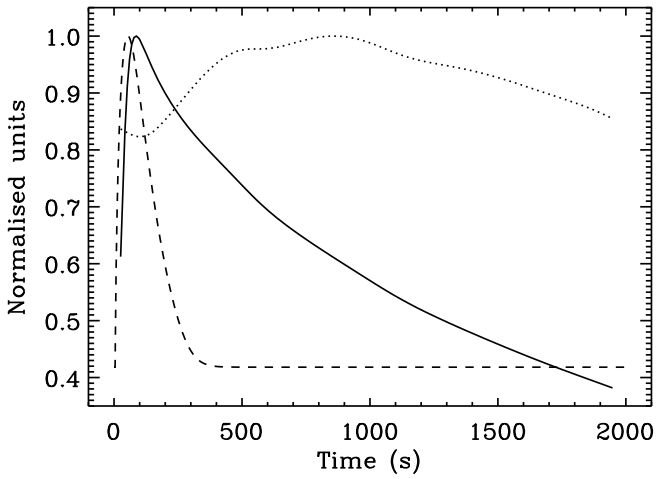

Figure 4.3: Spatially-averaged temperature (solid line) and density (dotted line) versus time, for a single energy pulse of run 5 ($t_C = 2000$ s), together with the logarithm of the heating-rate function (dashed line) applied in that case. The values are normalised to their respective maxima for a better comparison.

(e.g., Cargill, 1994; Spadaro et al., 2003; Klimchuk, 2006) and indicates that the initial cooling is dominated by thermal conduction, while, as temperature falls and density rises, radiation becomes progressively more important, eventually taking over as the primary cooling mechanism.

4.1.2 *Localised heating*

Asymmetric heating localised near the loop footpoints, both steady (run 6) and impulsive with $t_C = 250$ s ($t_C \simeq \tau_{cool}/4$, run 10), causes a more dynamic plasma evolution for similar values of the heating parameters, with respect to uniform heating simulations (see Fig. 4.4). The most evident feature is the presence of long-term, quasi-periodic fluctuations of temperature and density (after an initial steep increase) due to cycles of plasma condensation formation, motion along the loop, and falling onto the nearest and less heated footpoint (note that the first cycle only is reported in Fig. 4.4).

In the following we describe the temporal behaviour of the plasma in the steady heating case. Figure 4.5 shows the temperature profile at five different

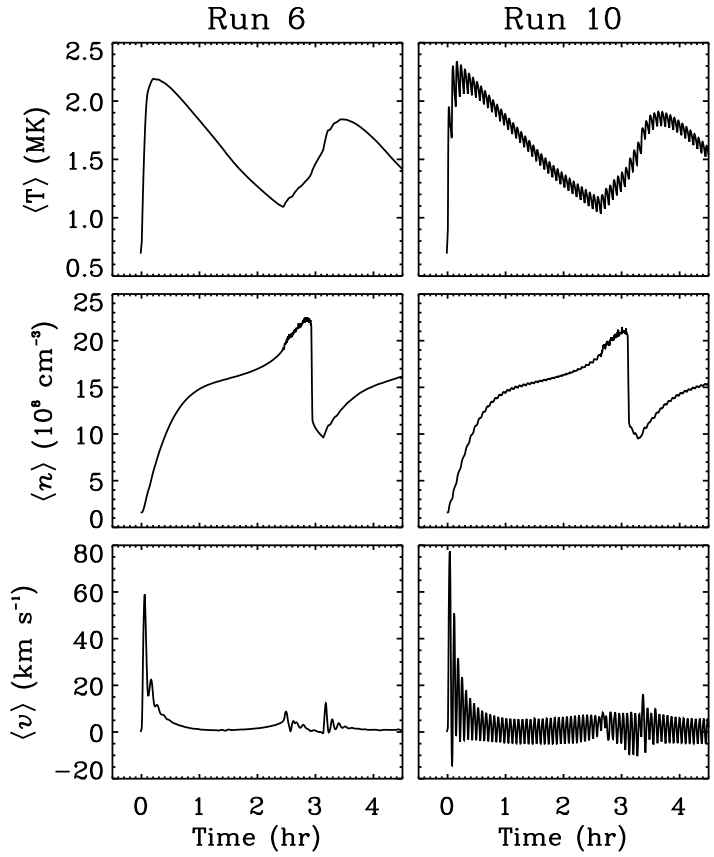

Figure 4.4: Initial part of the temporal evolution of the loop model temperature (top panels), density (middle panels), and velocity (bottom panels), averaged over the upper 3/4 of the loop coronal part, for run 6 (left panels) and 10 (right panels).

times during the first condensation cycle for run 6. After the start of the heating ($t = 0$ s), the loop rapidly heats and reaches a peak temperature $T_{max} \simeq 2.2$ MK at $t \simeq 750$ s. The steep temperature rise is accompanied by upflow velocities reaching ~ 60 km s^{-1}. Then, a relatively long period of slow cooling follows. It is worth noting that the maximum temperature occurs close to the more strongly heated footpoint (the left one), at a height slightly exceeding the heating scale-length $\lambda = 10$ Mm. The strong downward heat flux from the maximum temperature point drives an intense chromospheric evaporation from both footpoints that leads in turn to a continuous accumulation of material in the corona (see Fig. 4.5, dotted line). The increase of density near the loop top to values that

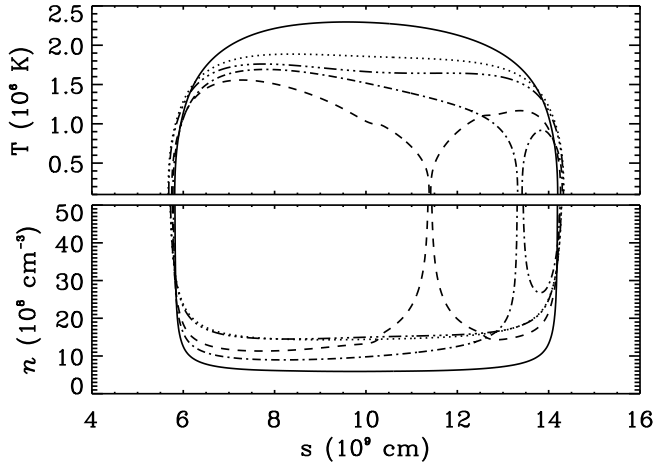

Figure 4.5: Temperature (top panel) and density (bottom panel) as functions of distance along the loop over its coronal section, for run 6. Different curves refer to different times after the start of the heating: $t \simeq 750$ s (solid line), $t \simeq 1$ hr (dotted line), $t \simeq 2.47$ hr (dashed line), $t \simeq 3$ hr (dot-dashed line), and $t \simeq 4$ hr (triple-dot-dashed line).

exceed the local equilibrium conditions induces an enhancement of the radiative losses that cannot be balanced by the relatively weak coronal heating, so that the plasma cools. After ~ 2.5 hours the temperature decreases at the chromospheric value of about 30000 K and a condensation appears at a position $s \simeq 115$ Mm (see Fig. 4.5, dashed line), i.e. ~ 25 Mm above the footpoint of the loop that was more weakly heated (the right one). Subsequently, the condensation starts moving towards the right footpoint, with increasingly higher velocities, and it eventually falls onto the chromosphere at $t \simeq 3$ hours, i.e., nearly half-an-hour after its formation. An explanation for the initial position of the condensation and its motion direction is derived in the next section by using scaling law arguments. After the sinking phase and the evacuation of the loop, a new cycle repeats, with a periodicity of about 3 hours. This result is in good agreement with that obtained by Müller et al. (2003, 2004) for similar values of the heating parameters.

The time-averaged plasma temperature, density, and velocity in the impulsive case do not show appreciable differences with respect to the corresponding steady case, as it appears from Fig. 4.4. We only note that, in the former case, there

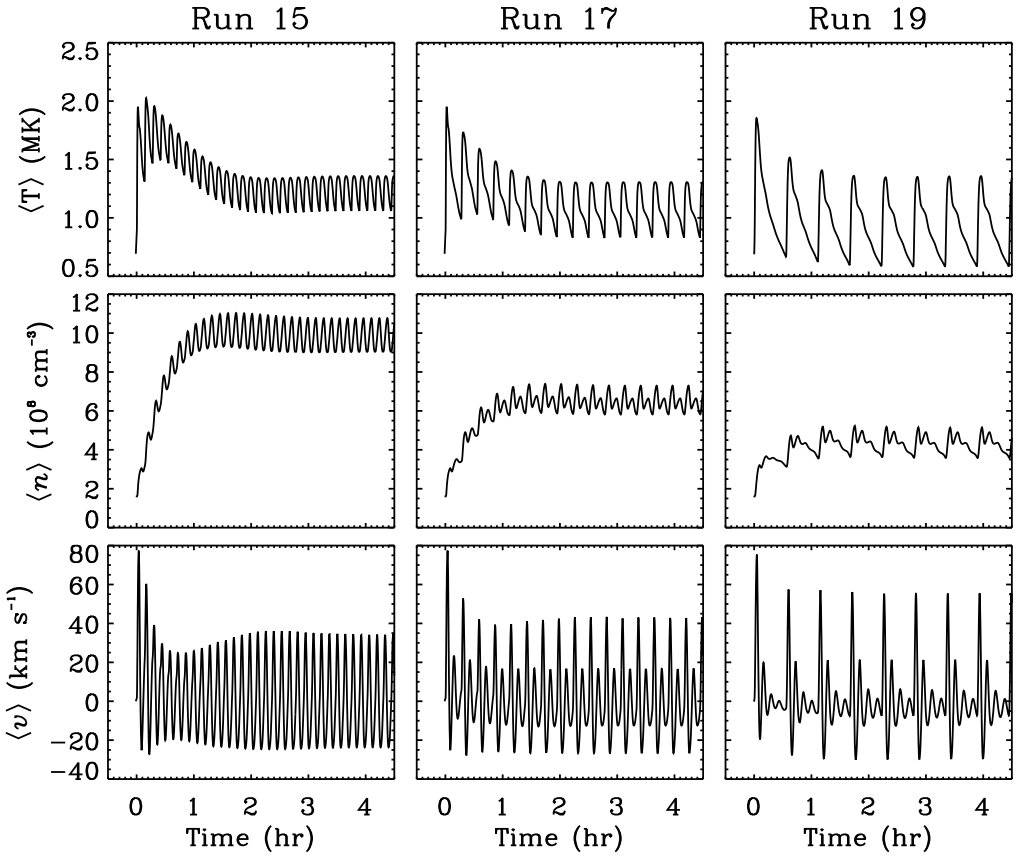

Figure 4.6: Same as in Fig. 4.4, for run 15 (left panels), 17 (middle panels), and 19 (right panels).

is a more dynamic initial phase with velocities up to nearly 80 km s^{-1}, while the condensation phase is accompanied by moderate downward velocities up to 10 km s^{-1}.

The remarkable differences between uniform and localised heating regimes suggest that the localisation of the heating near the loop footpoints plays a fundamental role in the plasma condensation formation when the energy deposition is both steady and impulsive, with a cadence time well below the loop cooling time. Note that a nanoflare cadence time of the order of $\tau_{cool}/4$ is yet sufficient to produce quasi-steady conditions. Our results, obtained for a ratio of the heating scale-length (λ) to the loop semi-length equal to $1/4$, are in general agreement with those of other works that model footpoint-heated loops in similar conditions

(e.g., Müller et al., 2003, 2004; Testa et al., 2005). Note that an even more concentrated heating can produce either a stable loop with a single, long-standing condensation (as found by Karpen & Antiochos, 2008, in the absence of a background heating) or a totally unstable loop with an irregular, chaotic evolution where periodic condensation regions are recurrently formed in a cool coronal core (as obtained, for instance, by Müller et al., 2004).

The temporal behaviour of the plasma parameters for the impulsive heating runs with $t_C \simeq \tau_{cool}/2$ (run 15), $t_C \simeq \tau_{cool}$ (run 17), and $t_C \simeq 2\,\tau_{cool}$ (run 19; see Fig. 4.6) closely resembles that of the corresponding uniform cases (see Fig. 4.2) with, however, much ample oscillations, particularly in the density and velocity curves.

We note that no condensation forms in these cases, because the intermittent heating prevents the accumulation of plasma at the loop top, and thus the thermal instability. This result is partially in contrast with that found by Karpen & Antiochos (2008), whose model developed a condensation for pulse cadence times comparable with the radiative cooling time. In their case, however, the heating was much more localised near the loop footpoints ($\lambda/L \simeq 0.04$). Therefore, it is reasonable to think that a smoother concentration of the energy supplied to the loop, as in our case ($\lambda/L = 4$), can prevent the occurrence of a thermal instability even when a rather high frequency of the energy pulses could favour the accumulation of material in the corona and the consequent enhancement of the radiative losses.

However, although the heating localisation and a high frequency pulse repetition are necessary to yield a catastrophic cooling phase during the loop evolution, they are not always sufficient. The crucial point is the balance between the energy supplied to the loop top by the sequence of heating pulses and the radiative losses of the plasma accumulated therein. In fact, by increasing sufficiently the amount of energy supplied by each pulse, even without changing the other parameters of the heating regime, such a balance can be achieved, thus preventing the thermal instability and the consequent plasma condensation formation. This is the case of run 11 ($H_P = 2 \times 10^{24}$) and run 12 ($H_P = 4 \times 10^{24}$; see Fig. 4.7), for which $t_C \simeq \tau_{cool}/4$. Note that in both the cases a catastrophic cooling phase is not developed during their evolution. A simple energy balance analysis (see

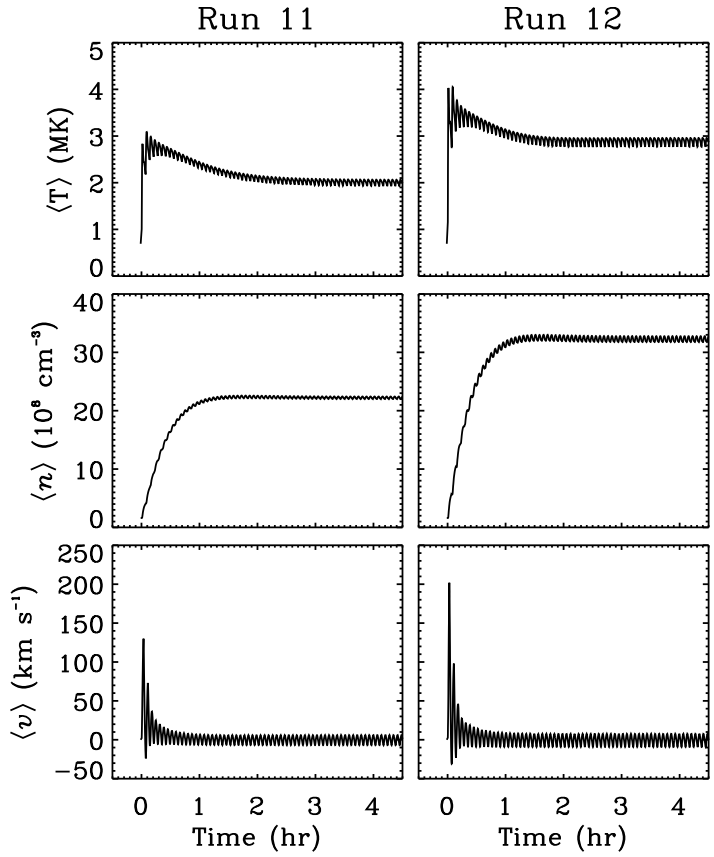

Figure 4.7: Same as in Fig. 4.4, for run 11 (left panels) and 12 (right panels).

Fig. 4.8) shows that in these cases the sum of heating, radiative losses, conductive losses, and enthalpy at different times during the loop evolution generally vanishes, at least between the loop top and the right footpoint, where a condensation is expected to form.

This result suggests that condensation formation is possible, at least for impulsive heating regimes with nanoflare repetition times smaller than the loop cooling time, only when the pulse energy is below a certain threshold (see Fig. 4.9). The global behaviour of the plasma parameters in these high-energy regimes does not differ substantially from that of the uniform heating cases (see Fig.s 4.1 and 4.2), except for the higher temperatures (up to 3 MK) and densities (up to $\sim 3 \times 10^9$ cm^{-3}) reached well after the heating has started. Note that the in-

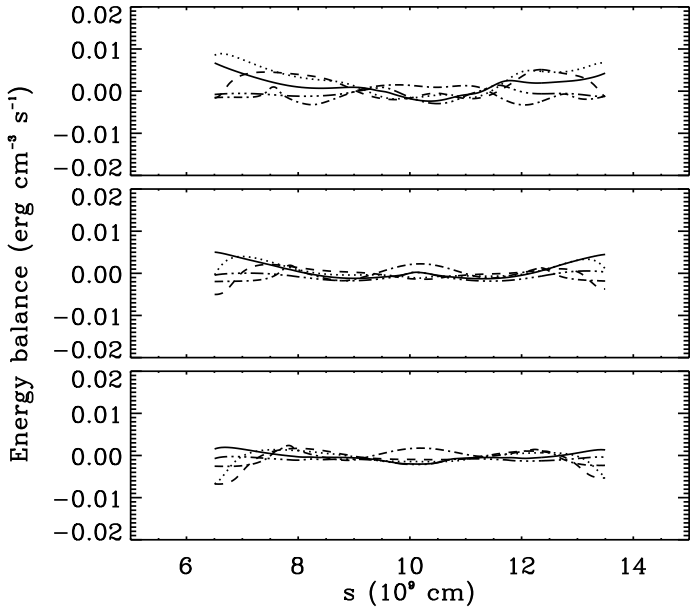

Figure 4.8: Energy balance ($H - \nabla \cdot F_{enth} - n^2\Lambda(T) - \nabla \cdot F_C$) as a function of the distance along the coronal part of the loop, at different times during a single nanoflare event, for runs 10 (top panel), 11 (middle panel), and 12 (bottom panel). Different curves refer to different instants after the start of the selected 250 s long pulse: 0 s (solid line), 25 s (maximum heating-rate, dashed line), 50 s (dotted line), 150 s (vanishing heating-rate, dot-dashed line), and 250 s (end of the pulse, triple-dot-dashed line).

crease in the average plasma temperature may have some little effect on the loop characteristic cooling time, which depends on $T_{max}^{-1/2}$ (see Eq. 3.12). Hence, we cannot rule out the possibility that the decrease of the cooling time, owing to the higher temperature, and the consequent increase of the ratio t_C/τ_{cool} to values nearer to unity may also contribute in preventing the occurrence of a thermal instability in these cases.

4.1.3 *Condensation dynamics*

As a condensation forms, it lies somewhere between the midpoint of the loop and the less heated footpoint, at a location where the upflows from each side of the loop are approximately balanced. Each section of the loop can be considered

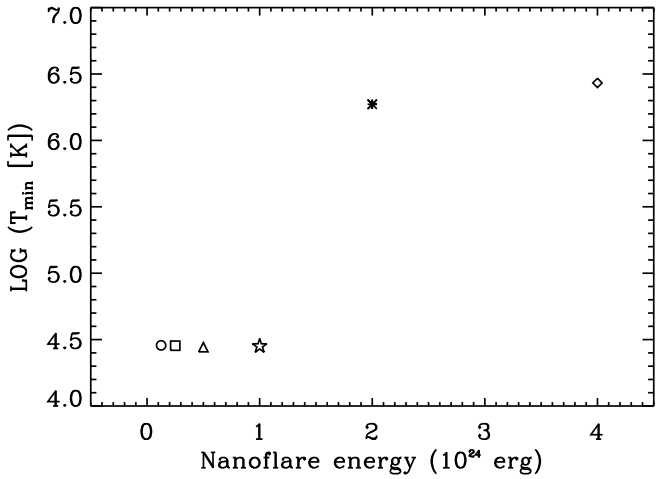

Figure 4.9: Minimum plasma temperature along the coronal part of the loop versus the nanoflare energy, for the six impulsive heating runs with $t_C = 250$ s $\ll \tau_{cool}$. Run 7 (circle), run 8 (square), run 9 (triangle), run 10 (star), run 11 (asterisk), run 12 (diamond). Note that loop models with $H_P \leq 10^{24}$ erg also develop a condensation during their evolution.

as an individual flux-tube, since the condensation region can be regarded as a discontinuity point that prevents heat and mass exchange from one side to the other one (Antiochos et al., 2000).

Each of these "loops" is heated only along a small fraction of its length near one footpoint, so that the energy to sustain radiative and conductive losses must be deposited into a large part of the loop by an enthalpy flux rather than by a heat flux. Substituting the enthalpy flux ($F_{enth} = \frac{5}{2}pv$) into the scaling laws yields

$$\frac{5}{2}\frac{pv}{L} \sim \frac{T^{7/2}}{L^2} \sim n^2 T^{\alpha}, \tag{4.1}$$

where all the variables have their usual meaning. The velocity v can be eliminated by using the additional scaling law that the enthalpy flux must be of the order of the total energy flux deposited into each loop leg:

$$\frac{5}{2}pv \sim H_0\lambda, \tag{4.2}$$

where H_0 is the heating rate at the base of the corona. Combining relations (4.1) and (4.2), it is possible to determine the loop pressure in each loop section as a function of energy input and loop length only:

$$p \sim H_0^{(11-2\alpha)/14} L^{-(2\alpha+3)/14}. \tag{4.3}$$

By assuming that the condensation is located at some position such that L_R and L_L are the lengths of the right and left loop sections, Eq. (4.3) implies that for the pressure on the right to be equal to that on the left we must have:

$$\frac{L_R}{L_L} = f^{(11-2\alpha)/(3+2\alpha)}, \tag{4.4}$$

where f is the asymmetry parameter ($f = H_R/H_L$). For $\alpha = -\frac{1}{2}$, this relation yields

$$\frac{L_R}{L_L} = f^6. \tag{4.5}$$

Since in our case $f < 1$, it results $L_R \ll L_L$. Thus, as the condensation forms, the pressure imbalance between the two sections of the loop forces it to move towards a new equilibrium position located just above the right footpoint, where, however, it cannot be sustained against the gravity due to the loop geometry.

The average velocities, accelerations, and masses of the condensations developed by runs 6, 9, and 10 throughout their lifetimes are shown in Fig. 4.10. The condensation region is defined as the interval in which the plasma temperature drops below $T = 10^5$ K in the coronal part of the loop. Velocities and accelerations refer to the midpoint of this region. The masses are computed by simply integrating the plasma density over the condensation region and assuming a constant cross-sectional area of 10^{15} cm^2. We report these quantities during the second condensation cycle, i.e. long after any memory of the initial static conditions has been cancelled.

The whole condensation phase lasts for $\sim$ 40 minutes and seems not to be strongly influenced by the variation of the mean energy dissipated into the loop. The period of the condensation cycle is of $\sim$ 200 minutes in the steady heating

case and only slightly longer in the impulsive cases; this implies that condensation's formation, motion, and falling onto the chromosphere take on average $\sim 20\%$ of the loop model evolution time.

In the steady heating case (run 6), the blob velocity initially increases up to about 15 km s^{-1} with an acceleration that is slightly lower than the free-fall one, $g_{\parallel}(s)$. Then the condensation is decelerated well below 10 km s^{-1}, probably because the pressure of the compressed plasma underneath has abruptly become quite large. After reaching the minimum velocity value, the blob continues falling down with monotonically increasing speed, until it sinks onto the chromosphere with a velocity that is something less than 30 km s^{-1} and nearly one order of magnitude lower than the maximum free-fall speed $v_{max} = \sqrt{2g_{\odot}h} \simeq 284$ km s^{-1}. In this phase, the acceleration curve exhibits a quite constant value of about 50 m s^{-2}, well below $g_{\parallel}(s)$: as the condensation moves towards the footpoint, the pressure on the left leg begins to drop and that on the right one increases because of the length dependence in Eq. (4.3), and this eventually prevents the blob of plasma from accelerating more and more during its fall. Note that this behaviour is very similar to that described in Müller et al. (2004), even if with different values of both velocity and acceleration. Note also that we do not find the oscillatory-like motions found by Antiochos et al. (2000) in their steady heating simulations and ascribed by these authors to the shocks produced by the initial "kick" of the condensation formation.

On the contrary, rather ample oscillations characterize the velocity and acceleration curves in both the impulsive heating cases shown in Fig. 4.10 (runs 10 and 9). They are superimposed on a net drift motion with a positive[1] velocity of about $10 - 15$ km s^{-1}. The period of oscillations is approximately 250 s, so that they can be interpreted as the effect of the energy pulses injected into the loop rather than the consequence of shock fronts produced by the condensation formation. The alternation of acceleration and deceleration phases may be due to the more intense chromospheric evaporation and sinking effects taking place near the left footpoint with respect to the right one; the condensation material probably sloshes back and forth in response to the different variations of pressure

1 Note that a *positive* velocity component on the right leg corresponds to a *positive* velocity component along the line-of-sight when the loop is observed from above.

between the two sections of the loop. The oscillations are eventually damped as the blob of plasma approaches the right footpoint; when it collapses onto the chromosphere it has a velocity of nearly 30 km s^{-1} in both cases.

The estimated mass of the condensation appears to increase monotonically in all cases. The average growth-rate seems not to depend on the steadiness or impulsiveness of the heating, but rather on the nanoflare energy, being lower for lower values of H_P. This sounds reasonable, since a higher heating-rate drives a stronger chromospheric evaporation and, in turn, a bigger accumulation of material.

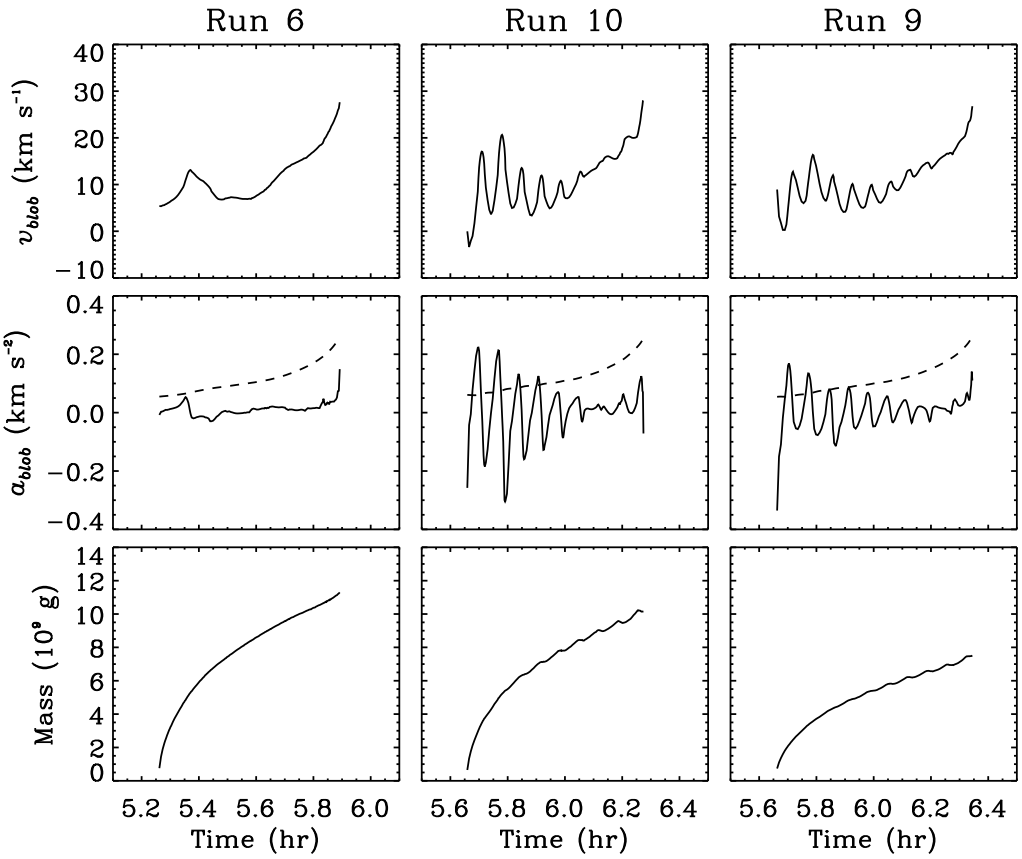

Figure 4.10: Velocity (top panels), acceleration (middle panels), and mass (bottom panel) of the condensations developed by the loop models of run 6 (left panels), 10 (middle panels), and 9 (right panels), as functions of time. The evolution of the second condensation cycle is only reported. The dashed lines in the middle panels show the effective gravitational acceleration, $g_{\parallel}(s)$, at the respective position of the condensation region. Note that the horizontal axis of the left-column plots has a different scale than those of the middle- and right-column plots.

4.2 LIMIT CYCLE OF LOOP EVOLUTION

To better illustrate the cyclic pattern of the thermal evolution of the model and its behaviour with respect to the hydrostatic equilibrium, we plot in Fig.s 4.11 and 4.12 the mean density as a function of the mean temperature for some representative loops, together with the hydrostatic scaling law relationship. Note that the RTV scaling law expressed by Eq. (2.28) may be rewritten as

$$n = 1.32 \times 10^6 \frac{T_{max}^2}{L}, \text{ i.e., } \log n \propto 2 \log T_{max}, \tag{4.6}$$

upon substituting p_0 from the ideal gas law.

We note that, in the initial phase of their evolution (lasting for about one hour), all the examined loops exhibit densities significantly smaller than those predicted by the scaling laws, in both steady and impulsive cases. Even though the onset of the heating produces an increase in the loop temperature and a large conductive heat flux at the base of corona, driving the upward chromospheric evaporation (Antiochos & Sturrock, 1978), there is a time lag in the corresponding increase of the coronal density (see Fig. 4.3), so that the loops appear to be hot and underdense. The initial displacement from the equilibrium position depends on the energy supplied to the loop by each pulse, H_P. The greater the nanoflare energy, the higher the temperature that is reached after the first pulse has occurred.

The subsequent evolution of the loop depends on the characteristics of the plasma heating.

In the uniform cases, when the heating is steady (run 1) or impulsive with a cadence time well below the radiative cooling time (run 2), the loop evolves towards a new state almost consistent with the hydrostatic scaling laws (only slightly underdense). When t_C increases and becomes comparable with or longer than the radiative cooling time (e.g., run 5) the loop begins to move along nearly cyclic sequences, spanning from hot ($T \simeq 1.2$ MK), underdense conditions to cool ($T \simeq 0.5$ MK), overdense ones. Note, however, that the range of density values (in dex) is significantly smaller than that covered in temperature. Moreover, the loops appear significantly overdense only at temperatures well below 1 MK.

In the localised cases, when the heating is steady (run 6) or impulsive with $t_C < \tau_{cool}$ (e.g., run 10), the evolution is considerably different than that of the uniform cases: as the temperature decreases, the plasma continues to evaporate and the density continues to rise, overshooting by a factor of ~ 5 the equilibrium values predicted for static loops with the same coronal temperatures, until a plasma condensation forms near the loop apex. The periodically condensing loops trace out limit cycles always remaining slightly overdense, even if the fall of material onto the chromosphere during the sinking phase causes an abrupt decrease of the average density to values closer to the hydrostatic equilibrium. Hence, these heating conditions can give rise to warm ($T \simeq 1-2$ MK), overdense loops with lifetimes of some hours, such as those observed by TRACE and SOHO.

Cadence times comparable with or longer than the cooling time (e.g., run 19) give rise to a loop evolution in general agreement with that found in the uniform cases for similar values of this parameter, although the plots reproducing the sequences exhibit some significant differences, particularly at the higher temperatures. The hydrodynamic behaviour during a single pulse is very similar to that described by Spadaro et al. (2003), who considered localized transient heating on time-scales comparable to the loop cooling time. Note that no condensation forms near the loop apex in these cases.

Increasing the amount of energy supplied by each pulse, even without changing the other characteristics of the heating regime (run 12), causes the loop to evolve towards a hot ($T \geq 2-3$ MK), quasi-static, slightly overdense state, where they settle after a balance is achieved between the energy supplied to the loop top and the radiative losses therein. It is worth noting that run 12 might apply to the case of the hot (~ 3 MK) loops seen by the *Yohkoh* Soft X-ray Telescope, without a corresponding warm counterpart (~ 1 MK) observed by TRACE (see, e.g., Nitta, 2000; Klimchuk, 2006). If these loops are impulsively heated, then the nanoflares must occur frequently enough for avoiding the plasma to cool to temperatures observed by TRACE.

It is worth noting that, if the loop were regarded as a bundle of independently heated magnetic strands then obviously there would be a wide variety of temperatures and densities present within its cross-section. Such a multi-stranded loop

could be obtained, for instance, by simply time-averaging one simulation over several time steps, as well as by averaging instantaneous snapshots taken from different simulations. If one simply assumes that all the strands in a given loop are identical except for the heating phase (i.e., they all undergo the same heating regime with *nearly* the same heating characteristics), then models like that of run 12 would produce underdense multi-stranded loops without cool counterparts, while models like that of run 6 would give rise to warm, overdense loops without a hot component.

We argue that it seems unlikely that all the strands in a given loop bundle would be identical except for their phases. It is much more reasonable that the heating mechanisms at work in the corona produce an energy deposition into each single strand in a rather wide range of parameters. Hence, composite loops that have a more realistic mixture of strands with different heating properties will also present hot and warm plasma components at the same time within their cross-sections. Consequently, they should be detectable almost simultaneously by both *Yohkoh* and TRACE.

However, there is no strong observational evidence of co-spatiality of hot and warm loops. Several authors tried to investigate the relationship between *Yohkoh* hot loops and cooler loops observed by SOHO EIT and TRACE. Hot loops are sometimes observed at the locations of warm loops (e.g., Winebarger & Warren, 2005), but not always. For instance, Nagata et al. (2003) and Schmieder (2004) found that little correlation exists beetween hot loops observed in soft X-rays and warm loops observed in EUV. In particular, they found that: i) their location and temporal evolution were significantly different; ii) their anti-correlation was conserved for a duration much longer than the estimated cooling time-scales. Moreover, recent *Hinode* EIS and XRT observations of the core of an active region (see Warren et al., 2009) showed a lack of evidence for warm emission spatially correlated with hot emission.

On the basis of our results, these observational concerns might suggest that, if loops are impulsively heated, then nanoflares within each strand should have a similar magnitude and recur with a similar frequency in order to produce different (and not correlated) conditions in the resulting loop bundle, depending on the magnitude of the dissipated energy.

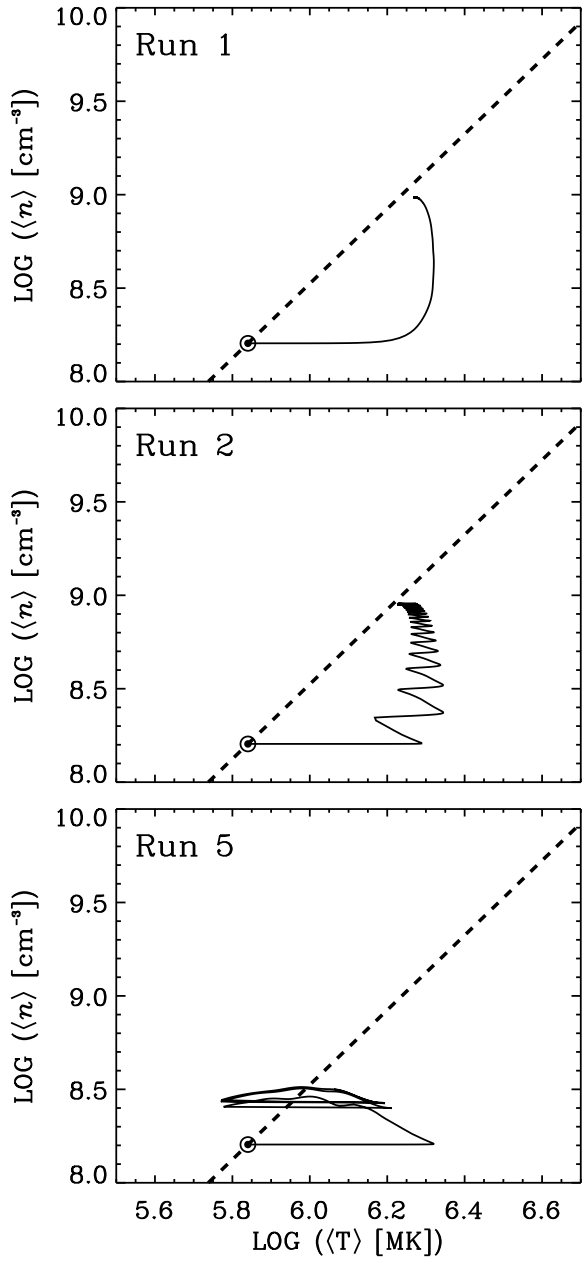

Figure 4.11: Evolution of the mean loop density and temperature for some uniform heating cases: run 1 (top panel), 2 (middle panel), and 5 (bottom panel). The hydrostatic scaling law (thick dashed line, see Eq. 4.6) is also reported, gauged according to the initial quasi-static state (indicated by the dotted circle).

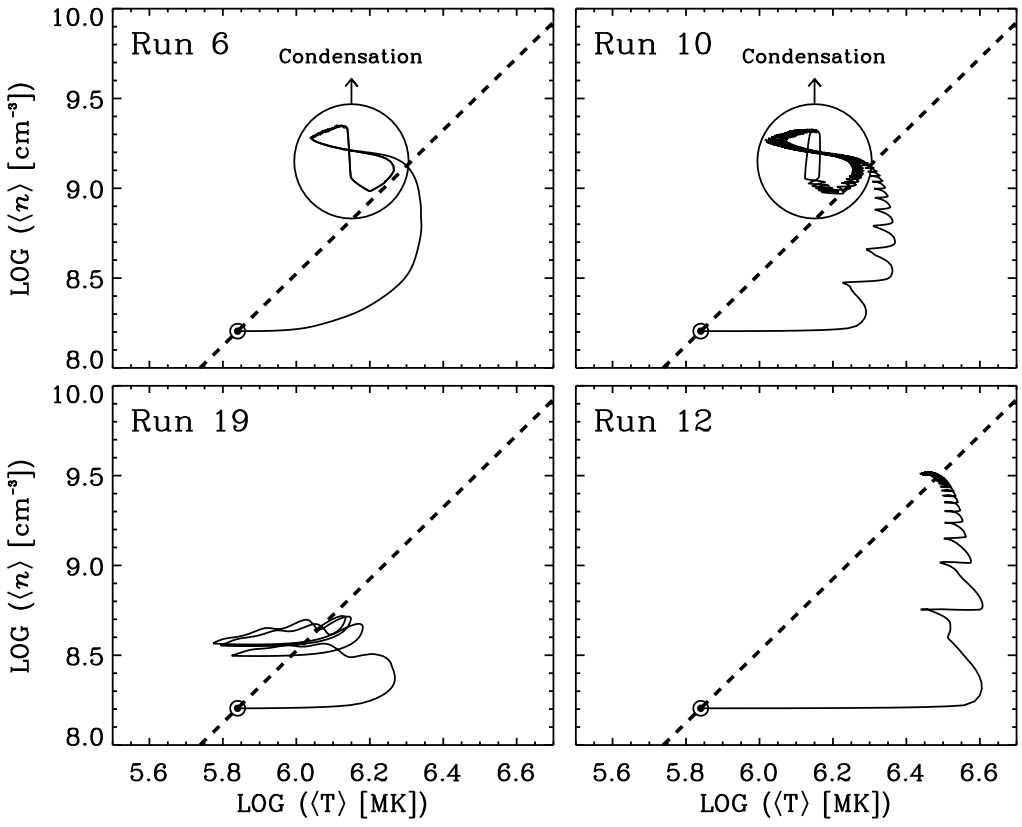

Figure 4.12: Same as in Fig. 4.11, for some representative localised heating cases: run 6 (top-left panel), 10 (top-right panel), 12 (bottom-left panel), and 19 (bottom-right panel). In the top panels, the evolution characterized by condensation formation cycles occurs within the encircled region labelled “condensation”.

5

RESULTS AND DISCUSSION: 2. PLASMA DIAGNOSTICS

The solar spectrum in EUV and soft X-rays contains a wealth of emission lines that depend on temperature and density in reasonably well-understood ways. They are produced by a variety of processes, which occur when an incoming photon or electron interacts with an atom or ion. Spectral lines are the result of the photon emission that follows such atomic interactions. Analysis of these lines can provide useful information about the properties of the emitting plasma (e.g., Dere & Mason, 1981; Mariska, 1992; Klimchuk & Cargill, 2001).

Here we investigate the possible signatures of the different heating regimes considered in our models on some plasma-related spectral quantities, such as the Doppler velocities of several spectral lines in the transition region and coronal and the differential emission measure emerging from the loop.

5.1 EMISSION LINE SPECTROSCOPY

5.1.1 *Line emissivity*

In the extremely rare and hot coronal plasma it is often assumed that: i) an emitted or diffused photon has a negligible probability to be absorbed or scattered by another particle (i.e., the plasma is optically thin); ii) the collisional excitation processes are faster than the ionisation and recombination time-scales, so that collisional excitation determines the population of excited states (the so-called coronal approximation).

The intensity $I(\nu_{ij})$ of an optically thin spectral line of frequency ν_{ij}, produced by photons via spontaneous atomic transitions from a higher level j to a lower level i, is defined as

$$I(\nu_{ij}) = \int_z \epsilon_{ij}\, dz = \frac{h\nu_{ij}}{4\pi} A_{ji} \int_z n_j(X^{+m})\, dz \quad (\text{erg cm}^{-2}\ \text{s}^{-1}\ \text{sr}^{-1}), \tag{5.1}$$

where ϵ_{ij} is the total line emissivity (units of erg cm^{-3} s^{-1} sr^{-1}), h the Planck constant, X^{+m} the m-fold ionised emitting ion, $n_j(X^{+m})$ the number density of the upper level j, A_{ji} the Einstein coefficient for spontaneous emission, and z is the line-of-sight direction through the emitting plasma.

The population of level j is generally expressed in a more useful way as a chain of ratios:

$$n_j(X^{+m}) = \frac{n_j(X^{+m})}{n(X^{+m})} \frac{n(X^{+m})}{n(X)} \frac{n(X)}{n_H} \frac{n_H}{n_e} n_e, \tag{5.2}$$

where $n(X^{+m})/n(X)$ is the ionisation ratio of the ion X^{+m} relative to the total number density of the element X, $n(X)/n_H = A_X$ is the elemental abundance relative to hydrogen, and n_H/n_e is the hydrogen to the free electron density ratio. The level population $n_j(X^{+m})/n(X^{+m})$ may be calculated by solving the statistical equilibrium for a number of low levels including all important collisional and radiative excitation and de-excitation mechanisms.

All the atomic parameters in Eq. (5.2) can customarily be combined into the so-called contribution function $C(\nu_{ij}, T, n_e)$, which is defined as

$$C(\nu_{ij}, T, n_e) = \frac{h\nu_{ij}}{4\pi} \frac{n_j(X^{+m})}{n(X^{+m})} \frac{n(X^{+m})}{n(X)} \frac{A_{ji}}{n_e}, \tag{5.3}$$

so that Eq. (5.1) may be rewritten as

$$I(\nu_{ij}) = \int_z A_X \, C(\nu_{ij}, T, n_e) n_e n_H \, dz. \tag{5.4}$$

An explicit expression for the contribution function may be found, for instance, in Stern et al. (1978):

$$C(\nu_{ij}, T, n_e) = \frac{\pi e^2}{m_e c} f_T \, f_{ion} \, G T^{-1/2} \exp\left(-\frac{h\nu_{ij}}{k_B T}\right), \tag{5.5}$$

where e is the electron charge, c the light speed, f_T the oscillator strength for the considered transition, f_{ion} the ionisation ratio of the involved atomic species,

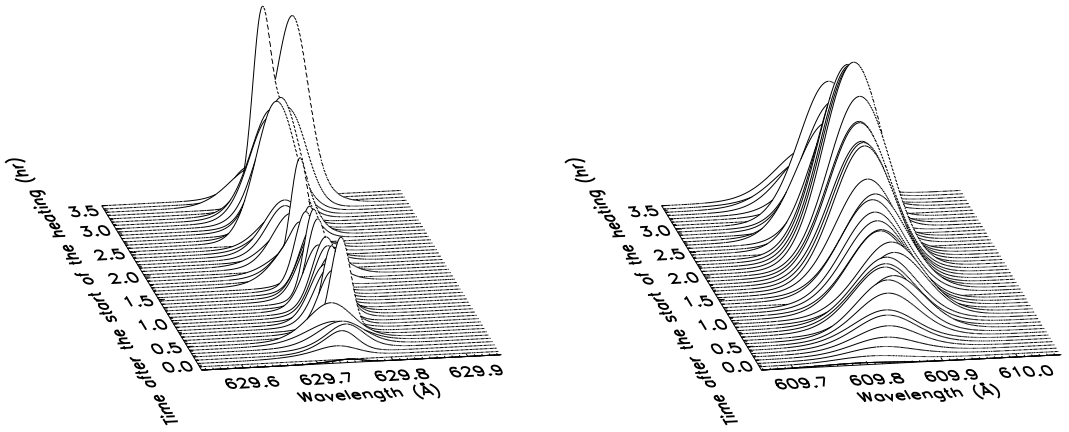

Figure 5.1: Examples of line profiles of O V (λ629 Å, left panel) and Mg X (λ609 Å, right panel) during the first part of the temporal evolution of the loop model of run 10 (localised impulsive heating) as seen from above. The quantities are integrated over the right half of the loop and are shown in arbitrary units for a better comparison.

and G is the Gaunt factor. Hence, by combining together equations (5.1), (5.4), and (5.5), it follows:

$$\epsilon_{ij} = \frac{\pi e^2}{m_e c} A_X f_T f_{ion} n_e^2 G T^{-1/2} \exp\left(-\frac{h\nu_{ij}}{k_B T}\right). \tag{5.6}$$

In this work, we computed the total emissivity in the lines of C IV λ1548 Å (formation temperature $T_f \simeq 10^5$ K), O V λ629 Å ($T_f \simeq 2.5 \times 10^5$ K), Ne VIII λ770 Å ($T_f \simeq 6.3 \times 10^5$ K), and Mg X λ610 Å ($T_f \simeq 1.25 \times 10^6$ K), using Eq (5.6). Note that O V and Mg X lines are good proxies of transition region and coronal conditions, respectively. Moreover, emission in C IV and O V lines is of particular interest since the 160 nm passband filter of TRACE is dominated by the former, while the latter is frequently observed with SOHO/CDS.

The local instantaneous profile of a given spectral line, forming in a coronal loop as seen from above, is obtained by multiplying the evaluated total emissivity in the line, ϵ_{ij}, for a purely Gaussian profile with thermal broadening given by

$$\Delta\lambda = \frac{\lambda_0}{c}\sqrt{\frac{2k_B T(s,t)}{m}}, \tag{5.7}$$

where λ_0 is the rest wavelength of the transition and m the atomic mass of the involved element, and centroid wavelength

$$\lambda_C = \frac{\lambda_0}{c} v_z(s,t) = \frac{\lambda_0}{c} \frac{ds}{dz} v(s,t), \tag{5.8}$$

where $v_z(s,t)$ is the component of plasma velocity along the line of sight and ds/dz the projection factor given by the loop geometry. Note that non-thermal broadening has been neglected in Eq. 5.7. An example of intensity profiles computed for different spectral lines is shown in Fig. 5.1.

As a first step, we evaluated the ionisation ratios in Eq. (5.6) by using the ionisation and recombination rates given by Arnaud & Rothenflug (1985) and assuming ionisation equilibrium. Clearly, this assumption may be only approximately correct, in particular when the time-scales of the temperature evolution are much shorter than the ionisation and recombination time-scales. In this case, the plasma ionisation degree could be very different from the equilibrium conditions corresponding to the local electron temperature (e.g., Orlando et al., 1999; Klimchuk, 2006). During a fast temperature increase, the plasma ions could be at a lower ionisation stage than the equilibrium state corresponding to the instantaneous temperature. Reale & Orlando (2008) showed that ionisation non-equilibrium effects are significant if the heating-rate temporal variations have time-scales of the order of a few seconds, irrespective of the heating magnitude. This applies, for instance, to nanoflare-heated loops when the energy pulses are strongly peaked. Non-equilibrium ionisation effects consist in a flattening of the temperature distribution of the plasma, leading the emitted spectra to never show temperatures higher than $2-3$ MK, even though the electron temperature overcomes 10 MK.

However, these authors pointed out that either very long nanoflare cadence times, so long to have a rather rarified loop ($n \sim 10^8$ cm^{-3}) before a new heating ignition, or more frequent energy pulses in a denser plasma ($n > 10^9$ cm^{-3}), which is faster to adjust to ionisation equilibrium, would lead to less non-equilibrium ionisation effects. Note that this is precisely our case (compare, for instance, Fig.s 4.11 and 4.12). Hence, we can assume our evaluation of the spectral emissivity fairly valid, at least as a first-approximation estimate, in all cases.

5.1.2 *Differential emission measure*

It is possible to express the line intensity defined in Eq. (5.4) in the simple form of an integral over the temperature, introducing another convenient quantity, the differential emission measure, DEM(T), that is a measure of the amount of plasma along the line-of-sight that contributes to the emission at the temperature T (see, e.g., Craig & Brown, 1976):

$$\mathrm{DEM}(T)\,dT = n_e n_H\,dz \approx n_e^2\,dz, \text{ i.e. } \mathrm{DEM}(T) = n_e^2 \left(\frac{dT}{dz}\right)^{-1}. \tag{5.9}$$

Thus, Eq. (5.4) may be rewritten as

$$I(\nu_{ij}) = A_X \int_T C(\nu_{ij}, T, n_e)\xi(T)\,dT. \tag{5.10}$$

By using a number of measured line intensities $I(\nu_{ij})$ and choosing a predefined set of elemental abundances A_X (e.g., Meyer, 1985; Feldman, 1992) and ionisation equilibrium data (e.g., Arnaud & Raymond, 1992), it is possible to calculate the contribution functions for each atomic transition (for instance, by the CHIANTI spectral code; see, e.g., Dere et al., 1997; Landi et al., 1999) and to determine the best-fitting differential emission measure distribution that is consistent with the data. If observations allow for a geometric model, the knowledge of DEM(T) can provide in turn a measure of the average density $n_e(T)$ for the range of temperatures corresponding to the formation temperatures of the selected lines. However, since equation (5.10) is highly unstable, its inversion constitutes a so-called ill-posed problem and a quite large range of different DEM(T) functions may be found to be consistent with the same spectral data. Therefore, a large number of emission lines with very high signal-to-noise ratios need to be selected from the observed spectrum, in order to constrain a single DEM(T) curve to consistently fit the data, because the uncertainties in the observed intensities are considerably amplified by the inversion procedure.

Figure 5.2 shows, as an example, a comparison between various differential emission measure distributions obtained for different solar environments. Observed DEM curves from active regions and the quiet Sun tend to be peaked

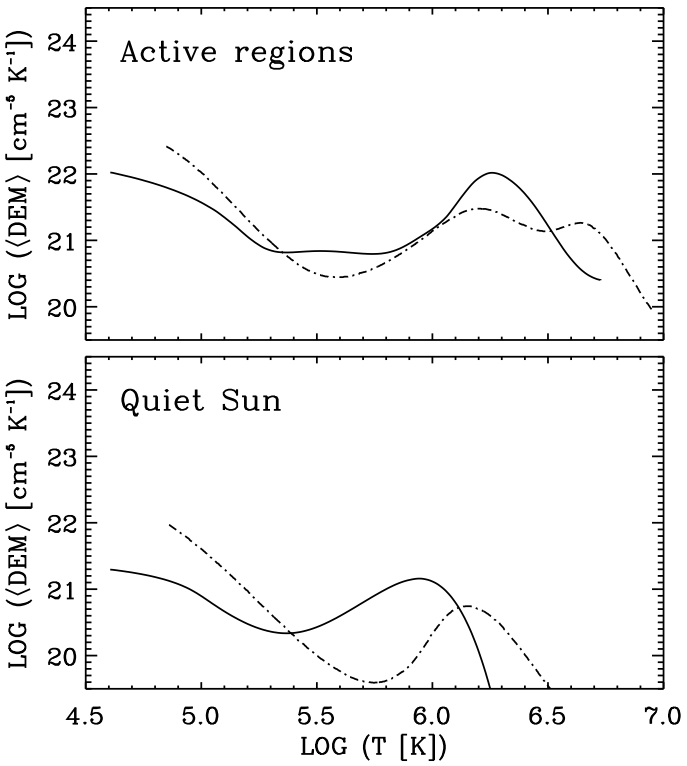

Figure 5.2: Differential emission measure distributions, DEM(T), for two solar active regions (top panel: SERTS-89 data from Lanzafame et al. 2002, solid line; SERTS-93 data from Brosius et al. 1996, dot-dashed line) and two quiet-Sun regions (bottom panel: CDS data from Lanzafame et al. 2005, solid line; SERTS-93 data from Brosius et al. 1996, dot-dashed line).

near $\log T \simeq 6.5$ and $\log T \simeq 6.1$, respectively. Moreover, the slope of the $\log \mathrm{DEM} - \log T$ relation[1] at temperatures lower than that of the peak is determined by the physical processes responsible for the energy balance (see, e.g., Antiochos, 1980). Observed DEMs generally have a slope $\beta \gtrsim \frac{1}{2}$ (e.g., Craig et al., 1978; Raymond & Doyle, 1981).

We evaluated differential emission measure distributions of our individual loop models as follows (see, e.g., Peter et al., 2006; Karpen & Antiochos, 2008). We replaced into Eq. (5.9) the column depth dz with the loop segment ds and we

1 Expressed by the temperature power law index β such as $\mathrm{DEM} \propto T^{\beta}$.

computed the differential emission measure at a given temperature, DEM(T), by averaging the resulting expression over a fixed temperature interval around T. Since the emission lines from transition region and corona are typically formed over a range of 0.2 in $\log T$, we employed a fixed logarithmic temperature interval $\Delta \log T = 0.2$, thus obtaining the logarithmic differential emission measure:

$$\mathrm{DEM}_{log}(T) = \frac{1}{\Delta \log T} \sum_i n_i^2 \, ds_i, \quad (\mathrm{cm}^{-5}) \tag{5.11}$$

where the subscript i indicates the i-th cell of the computational domain and the sum is extended to all the cells whose temperature T_i falls in the interval $[\log T - 0.1, \log T + 0.1]$. Finally, we set:

$$\mathrm{DEM}(T) = \frac{1}{T \ln(10)} \mathrm{DEM}_{log}(T), \quad (\mathrm{cm}^{-5}\ \mathrm{K}^{-1}) \tag{5.12}$$

according, e.g., to Klimchuk et al. (2008). The differential emission measure defined in Eq. (5.12) indicates the amount of loop plasma, $n^2 \Delta s$, that is present in a temperature interval ΔT, and can directly be compared to differential emission measure distributions derived from observations.

5.2 TEMPORAL AVERAGES

Line emissivities and differential emission measure distributions computed at each time step during a given simulation, as described in the previous section, are representative of the evolution of an individual magnetic strand.

To simulate more realistic temperature and density measurements from our models, such as those obtained from multi-stranded loop observations, we averaged these quantities over a sample of $n = 300$ time steps randomly selected throughout each simulation. By doing so, we assume that the states of the model at n random times can be used to describe the behaviour of n independent strands observed at the same time (see, e.g. Patsourakos & Klimchuk, 2005). Thus, a single simulated snapshot of a multi-stranded loop is obtained.

We averaged instantaneous line profiles for each spectral line over the selected sample of times to obtain a single mean intensity profile at each loop location. We then derived, from such mean profiles, Doppler-shifts of the centroids of the lines as functions of the distance along the simulated loop bundle.

As far as the differential emission measure distributions are concerned, we simply averaged the theoretical single-strand DEMs computed at the different randomly selected time steps of the sample using Eq. (5.12).

5.3 SPECTRAL SIGNATURES OF HEATING REGIMES

5.3.1 *Doppler-shifts*

In Fig.s 5.3 and 5.4 we plot the mean Doppler-shifts converted to velocity units, $\langle v_D \rangle$, derived for C IV, O V, Ne VIII, and Mg X lines, as functions of the distance along the coronal part of the loop, for the same representative models discussed in Sect. 4.2.

In the uniform cases (runs 1, 2, and 5), the synthesised lines do not exhibit appreciable shifts of their centroids with respect to their rest wavelengths, irrespective of the steadiness or impulsiveness of the heating. This is due to the negligible dynamics that characterize these models (see, e.g., Fig.s 4.1 and 4.2). We only note, in the impulsive heating case with $t_C \gg \tau_{cool}$ (run 5), moderate blue-shifts of the Mg X and Ne VIII lines (less than -5 km s^{-1}) located in the proximity of the loop footpoints, in correspondence of slight red-shifts (of the same order of magnitude) of the O V line. The coronal Mg X line probably traces out the upward motions of hot plasma driven by the chromospheric evaporation that follows the ignition of the heating pulses, while the O V lines (which forms at transition region temperatures) trace out the downflows of the plasma cooling and sinking towards the solar surface. The values inferred for the Mg X line are consistent with those recently obtained by Brooks & Warren (2009) from *Hinode* EIS data in the line of Fe XII λ195 Å (which forms at a similar temperature than the Mg X line), recorded in the moss within a flaring active region. The moss is believed to correspond to the $\sim$ 1 MK footpoints of hot loops with coronal temperatures of $\sim 3-5$ MK.

In the localised cases, both steady and impulsive with $t_C = 250$ s $\simeq 1/4\,\tau_{cool}$ (run 6 and 10, respectively), the most evident feature is that transition region lines (i.e., C IV and O V lines) are strongly red-shifted, with Doppler velocities $\langle v_D \rangle \simeq 20$ km s^{-1}, at locations near the right footpoint of the loop. The Ne VIII line shows, at the same position, only a moderate red-shift, less than 5 km s^{-1}, and even less the coronal Mg X line. Conversely, all the spectral lines exhibit slight blue-shifts with velocities of ~ -5 km s^{-1} near the left footpoint.

The remarkable differences with respect to the corresponding uniform cases are due to condensation formation that occurs during the evolution of the localised heating runs. The C IV and O V red-shifted line emission is most probably produced by the cool plasma ($T \simeq 0.1 - 0.2$ MK) that lies in the thin transition regions forming at both sides of the condensation, and, consequently, it traces out the motion of the blob towards the right footpoint. Note that the maximum shift velocity inferred for these lines is comparable to the maximum speed of the falling condensation during the draining phase (see Fig. 4.10). Heating localisation also causes a more intense chromospheric evaporation, particularly near the left and more strongly heated footpoint, and this may account for the significant upflows that are evident therein.

When the nanoflare cadence time increases to values longer than the loop cooling time (e.g., run 19), the prominent red-shifts of C IV and O V lines on the right-hand side of the loop disappear, since condensation does not form in this cases, while rather pronounced blue-shifts of the Mg X line (and, to a lower extent, of the Ne VIII line) are evident at both loop footpoints. The different velocities inferred for the Mg X line at the left footpoint ($\langle v_D \rangle \simeq -20$ km s^{-1}) and at the right one ($\langle v_D \rangle \simeq -10$ km s^{-1}) are a clear signature of the asymmetric heating. Such significant blue-shifts can be attributed to hot material ($T \simeq 1$ MK) that is evaporating into the loop, while the cooler plasma that is being pushed downwards by the consequent pressure enhancement due to the evaporative heat flux might account for the slight red-shifts (implying velocities lower than 5 km s^{-1}) that are evident in the O V Doppler-shift curve. Note that these results partially agree with those obtained, for instance, by Hara et al. (2008), who analysed *Hinode* EIS data from a solar active region and found evidence of significant blue-shifts at the base of coronal loops, with Doppler velocities of the order of 10 km s^{-1} and

gradually decreasing with height. However, they considered in their work only the lines of Fe XIV λ274 Å and Fe XV λ284 Å, that form at higher temperatures ($T \simeq 2$ MK) than the Mg X line. Conversely, Del Zanna (2008) found a lack of signatures of any upflows in either leg of some coronal loops observed with EIS and showed that blue-shifts are generally located in sharp regions at the boundary of active regions and that shifts are higher in higher-temperature coronal lines (for instance, they measured velocities of typically $5 - 20$ km s^{-1} in the Fe XII λ195 Å line).

Spectral lines synthesised for the impulsive cases with high pulse energy (e.g., run 12) do not exhibit substantial shifts, besides marginal red-shifts (with Doppler velocities lower than ~ 5 km s^{-1}) near the right footpoint of the loop, visible in all the examined lines. This confirms that impulsive heating with very high pulse frequency produces quasi-static states, at least in absence of condensation formation, which seems to occur only when the nanoflare energy is below a certain threshold.

Our results suggest that the analysis of Doppler-shifts of coronal lines could help in discriminating between localised heating regimes in which the nanoflare cadence time is longer or shorter than the cooling time of the loop. Conversely, Doppler-shifts of transition region lines are strongly sensitive to condensation formation processes, and, consequently, to high-frequency pulsed heating regimes with mean energy rates below a certain threshold. However, these results further imply that it is impossible to distinguish among uniform heating regimes, both steady and impulsive, and localised ones, when the nanoflare repetition time is shorter than the loop cooling time and the mean energy rate is above the same threshold.

5.3.2 *Differential emission measure*

Figure 5.5 shows the differential emission measure distributions corresponding to the initial steady equilibrium conditions achieved at the end of the relaxation phase (see Sect. 3.2.2), and the uniform, steady heating case of run 1. The initial-state DEM was computed by averaging instantaneous DEMs over the last 2 minutes before the start of the additional heating.

In spite of the about one-order-of-magnitude higher values shown by the DEM relative to run 1 with respect to that of the initial-state, the two curves both exhibit the same gross behaviour. They peak at the respective maximum temperature ($\log T_{peak} \simeq 6.2$ in the former case, $\log T_{peak} \simeq 5.8$ in the latter), then they show a rather flat plateau at temperatures lower than that of the peak and an increasing tail below $\log T \simeq 5.1$, due to the overwhelming contribution of transition region plasma. Obviously, the similar trend of the curves reflects the similar equilibrium conditions attained by the loop in the two cases, and all the differences are simply due to the different heating-rate applied.

It is worth noting that the DEM computed for run 1 is quite consistent, in terms of magnitude and location of the peak, with some observed DEM curves from active regions (e.g., Brosius et al., 1996; Lanzafame et al., 2005, see Fig. 5.2), at least at coronal temperatures, while it is totally discrepant at lower temperatures ($\log T < 5.5$), owing to the strong contribution from the transition region. However, it is possible that absorption from chromospheric material such as spicules significantly attenuates the intensities of transition region lines used to construct the DEM curves (see, e.g., Klimchuk et al., 2008; De Pontieu et al., 2009).

To avoid cool plasma contamination from the transition region sections of the loop, we also computed the differential emission measure excluding from calculation all the grid cells located less than 10 Mm above the footpoints (see, e.g., Karpen & Antiochos, 2008). The corresponding curve (Fig. 5.5, dotted line) is very peaked in temperature, meaning that the upper 3/4 of the loop contribute only in a rather narrow range of temperatures (~ 0.2 dex, centred around $\log T \simeq 6.3$). The transition region contribution of course dominates at low temperatures, but it is also significant at hotter temperatures that are normally associated with the corona. Note that such coronal DEM again is inconsistent with the curves derived from on-disk observations plotted in Fig. 5.2, at least at low temperatures.

Uniform impulsive heating

DEMs obtained from uniform, impulsive heating simulations, computed either including or excluding the transition region contribution as described above, are reported in Fig. 5.6.

The impulsive model with the lowest cadence time (run 2) do not show appreciable differences with respect to the corresponding steady model (run 1), as expected.

Increasing the nanoflare cadence time up to $t_C = 2000$ s $> \tau_{cool}$ (e.g., run 5) causes a general decrease in the DEM values, up to something less than one order of magnitude on average, and a displacement of the coronal peak towards lower temperatures ($\Delta \log T_{peak} \simeq 0.35$). Note, however, that in these cases the DEM is controlled essentially by the mean energy dissipated per unit time, which actually determines the temperature at which the DEM is at its maximum, as well as its magnitude. The runs reported in Fig. 5.6 have fixed $H_P = 10^{24}$ erg, and therefore the longer t_C, the lower $\langle H \rangle$.

As it appears from the transition-region-free DEMs, longer cadence times produce much broader emission measure distributions at coronal temperatures. This sensitivity of the DEM to the nanoflare frequency derives from the fact that, when t_C increases well above τ_{cool}, the bulk of the plasma has a temperature oscillating over a rather large range (see Sect. 4.1.1 and discussion therein). In the full-loop DEM curves, such broadening produces a smearing of the DEM and eventually leads to the disappearing of the rather pronounced coronal peak.

We note, in particular, that DEMs computed for the runs with low $\langle H \rangle$ (i.e., those with $t_C \gtrsim \tau_{cool}$: runs 4 and 5) might almost reproduce the coronal part of some observed quiet Sun DEM curves (e.g., Brosius et al., 1996; Lanzafame et al., 2002, see Fig. 5.2), even if they are completely inconsistent at low temperatures, either considering or not the contribution from transition region. However, we report cases in which DEM curves obtained from CDS and TRACE observations after background subtraction (see Schmelz et al., 2009) closely resemble the transition-region-free DEMs inferred from our uniform heating models.

Localised heating

In Fig. 5.7 we consider DEMs obtained for the localised impulsive heating models with the same parameters as the uniform cases of Fig. 5.6 (runs 10, 15, 17, and 19). The DEMs are calculated either including or not the contribution from the transition region. We do not plot the DEM for the steady case (run 6), since it practically overlaps that of the corresponding impulsive case (run 10).

The first evident feature is that the full-loop differential emission measure derived for the localised heating models is almost identical to that of the corresponding uniform models. In particular, the differences between the localised case in which condensation occurs (e.g. run 10) and the uniform one in which it does not occur (e.g. run 2) are too small to be appreciated in practice. Condensation does not produce appreciable variations in the DEM because the bulk of the plasma maintains a temperature above $\sim$ 1 MK throughout the loop evolution (compare, for instance, with Fig.s 4.11 and 4.12). This suggests that differential emission measure could be not a good diagnostic for plasma condensation formation processes.

On the contrary, when the contribution from transition region is neglected, a systematic difference in shape appears between the run that formed condensation (run 10) and those that did not (runs 15, 17, and 19). The former exhibits a broad, shallow minimum approximately located at $\log T \simeq 5.5$ MK, whereas the condensation-free DEMs are measurable only at coronal temperatures, as in the previous cases. Note that the transition-region-free DEM for run 10 qualitatively agrees with the observed active region DEM curves cited above, both in terms of position of the minimum, slope of the curve at higher temperatures, and position of the coronal peak. Nevertheless, it must be kept in mind that the DEMs plotted in Fig. 5.2 result from on-disk observations and should in principle include the transition region component.

We plot in Fig. 5.8 DEMs obtained from models with different combinations of t_C and H_P giving the same mean energy rate. Choosing $\langle H \rangle = 4 \times 10^{21}$ erg s^{-1} (runs 10, 16, 18, and 20), we obtain a DEM peak similar to that observed in active regions, while for $\langle H \rangle = 0.5 \times 10^{21}$ erg s^{-1} (runs 7, 13, and 19), we obtain DEMs comparable to those inferred for quiet Sun regions. Again, the dependence of the DEM shape on t_C as described above is maintained.

However, also in these cases, the simulations are unable to reproduce the whole observed DEM structure. By appropriately selecting t_C and H_P, it is possible to reproduce the DEM in the high temperature range or around the minimum, but it is not possible to reproduce the DEM in both ranges with a single (t_C, H_P) pair.

We tried also to compute DEMs by averaging together models with different heating properties. In particular, we considered runs with the same cadence time

($t_C = 250$ s) but different pulse energy and models with the same nanoflare energy ($H_P = 10^{24}$ erg) but different repetition times. Such composite DEMs are reported in Fig. 5.9. The curves exhibit a similar gross behaviour as in the previous cases and are unable to fit simultaneously the low- and high-temperature part of the observed DEMs, both for active regions and quiet Sun.

In conclusion, the assumption of multi-stranded structures subject to localised impulsive heating is not sufficient to explain the well known discrepancies with observations, which probably depend on physical processes not included in our simulation. The recent suggestion by Judge (2008) of cross-field diffusion of neutral atoms from cool threads extending into the corona might help in solving these kinds of problems. Moreover, it has been shown that the discrepancy between the predicted and the observed EUV brightness of the transition region could be due to the absorption of EUV light with wavelengths below 912 Å by the resonance continua of neutral hydrogen and helium, expected to occur in the moss, i.e. the low-lying transition region of hot, active region loops, that is co-located with cool chromospheric features (e.g., De Pontieu et al., 2009).

Nevertheless, we suggest that, despite such discrepancies, the systematic behaviour of the average DEM with t_C would maintain its validity even if the models are not sufficiently detailed, and would help in discriminating at least among the high- and low-cadence regimes. In fact, despite the small sensitivity of the DEM to variations in t_C, when this increases well above τ_{cool}, the coronal DEM peak tends to disappear. Such changes in the DEM shape can be reliably verified by comparison with observations, since they are well above the uncertainties in the DEM reconstruction due to regularisation smoothing. The very existence of the coronal DEM peak, therefore, could be an indication of the existence of heating pulse cadence time shorter than τ_{cool}.

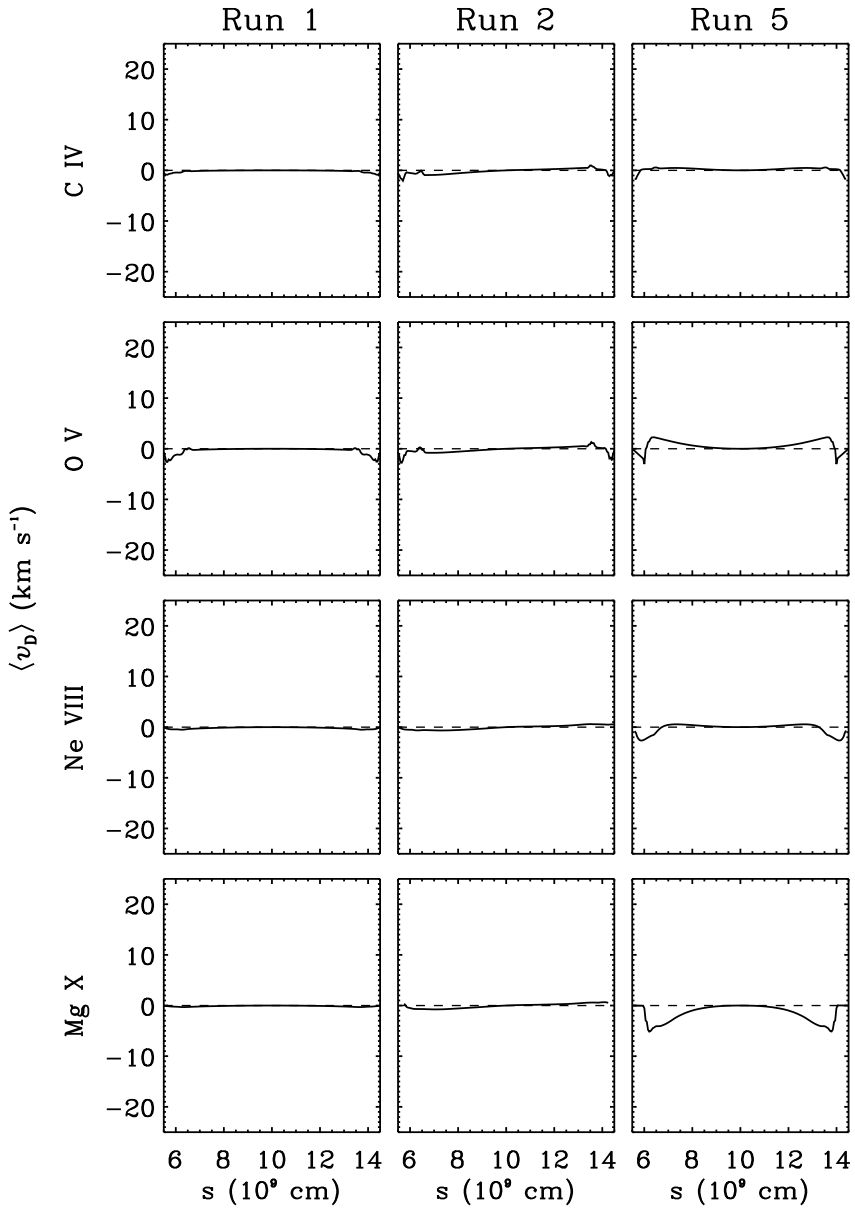

Figure 5.3: Time-averaged Doppler velocities, deduced from the synthesised emission in the lines of C IV λ1548 Å, O V λ629 Å, Ne VIII λ770 Å, and Mg X λ610 Å, plotted versus distance along the coronal part of the loop, for the uniform heating models of run 1 (left panels), 2 (middle panels), and 5 (right panels). Note that positive (negative) velocities correspond to downflows (upflows).

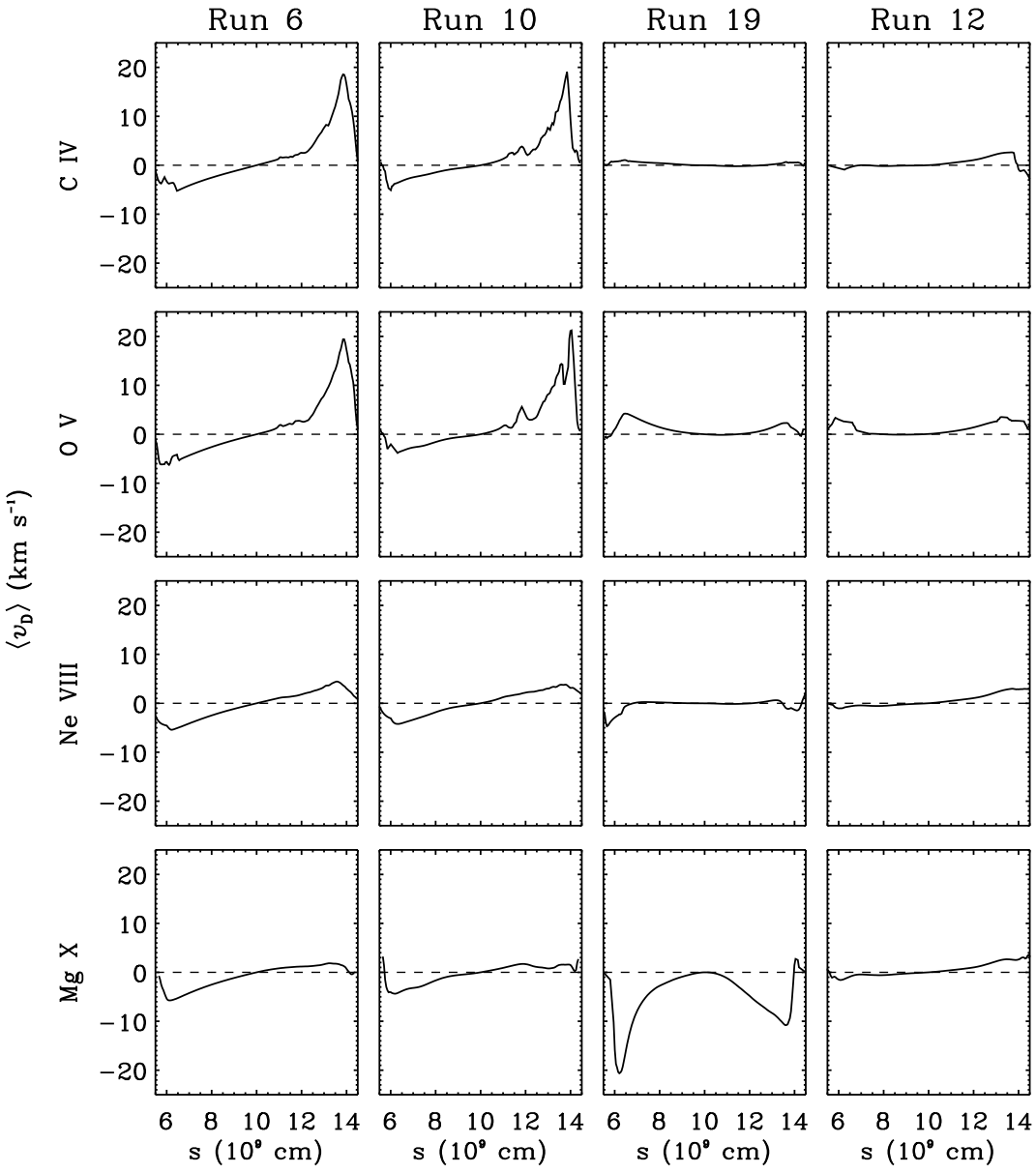

Figure 5.4: Same as Fig. 5.3, for some representative localised heating cases: run 6 (left column), 10 (second column), 19 (third column), and 12 (right column).

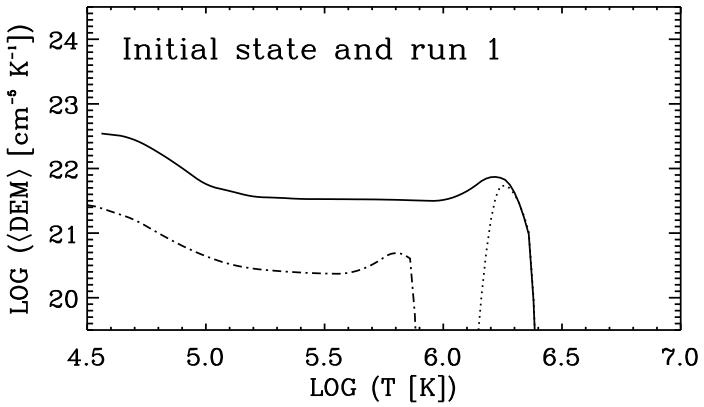

Figure 5.5: Average differential emission measure (DEM) computed for the initial steady equilibrium conditions adopted in our simulations (dot-dashed line) and the uniform steady heating case with $\langle H \rangle = 4 \times 10^{21}$ erg s^{-1} (run 1), both including (solid line) and excluding (dotted line) the contribution of the transition region sections of the loop.

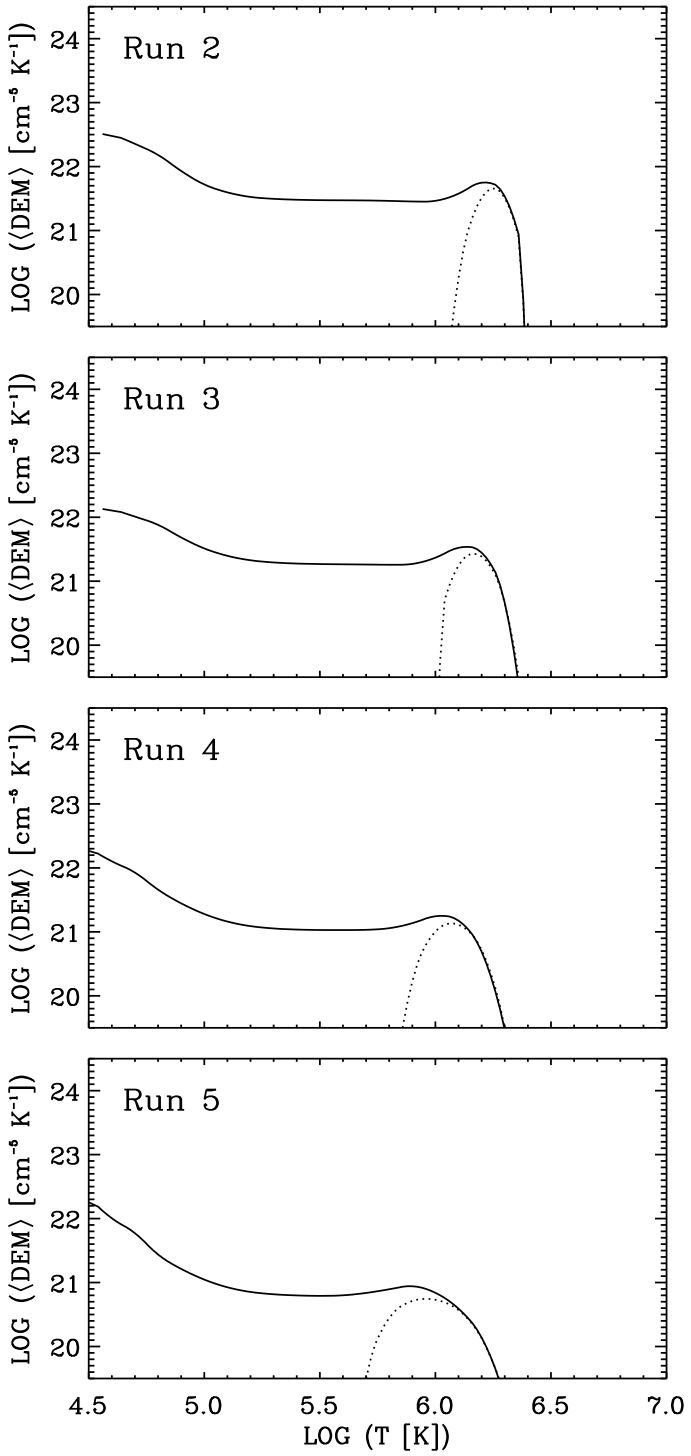

Figure 5.6: As in Fig. 5.5, for the uniform impulsive models of run 2, 3, 4, and 5 (from top to bottom).

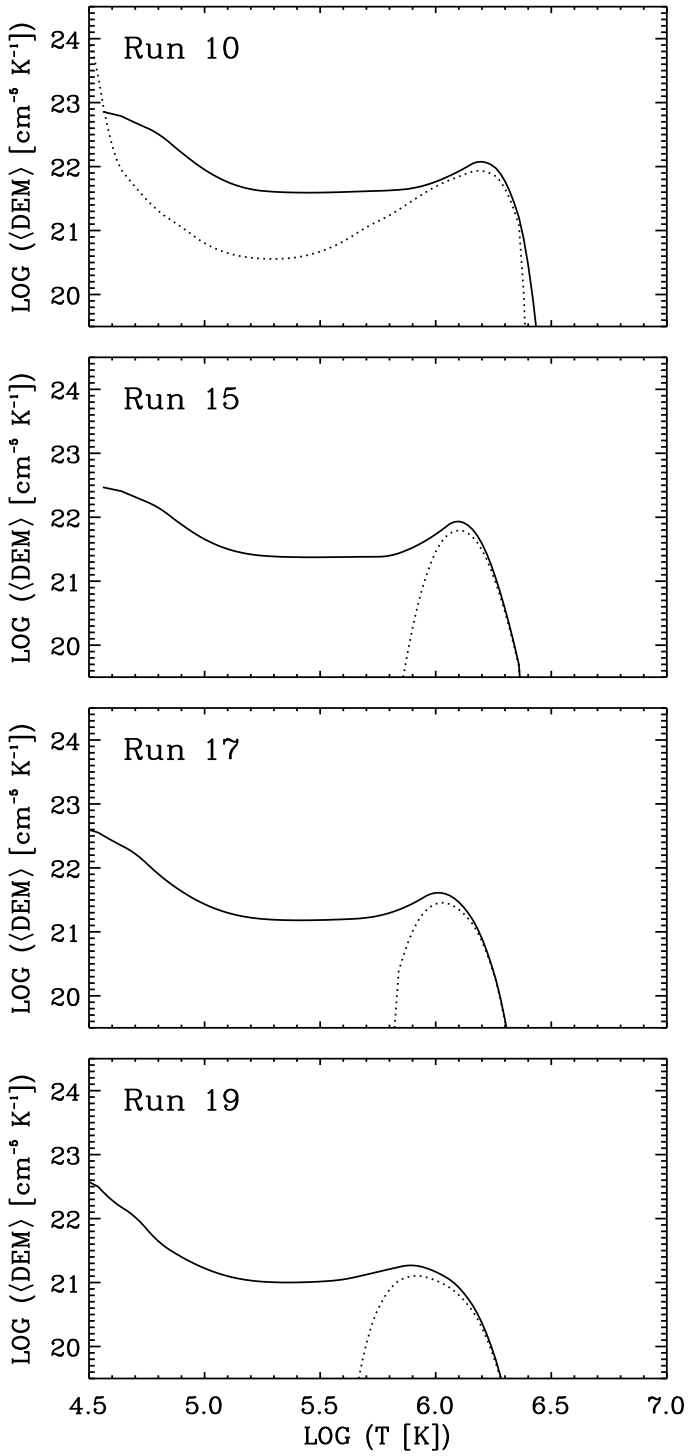

Figure 5.7: As in Fig. 5.5, for the localised impulsive models of run 10, 15, 17, and 19 (from top to bottom).

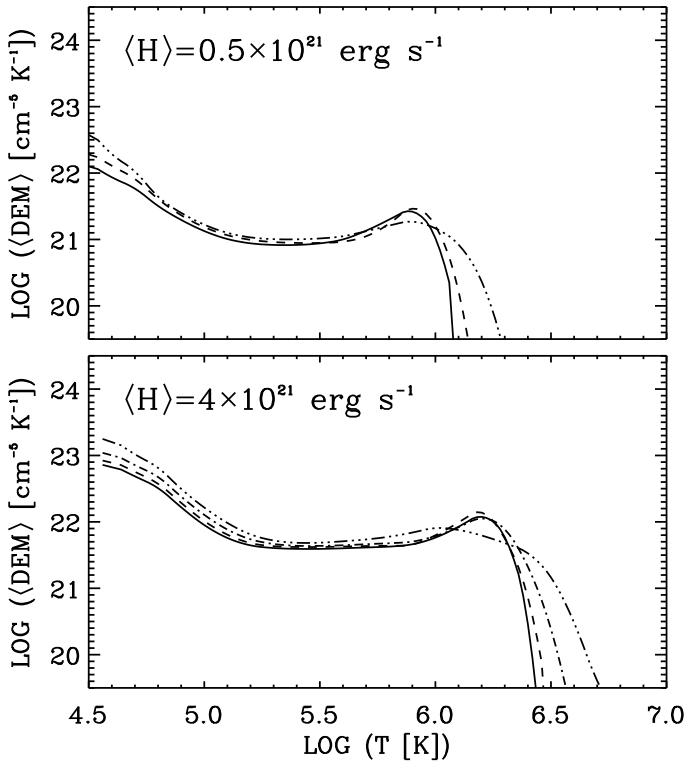

Figure 5.8: Average DEMs for localised impulsive models with different combination of t_C and H_P giving the same mean energy. *Top panel:* $\langle H \rangle = 0.5 \times 10^{21}$ erg s^{-1} (run 7, solid line; run 13, dashed line; run 19, triple-dot-dashed line). *Bottom panel:* $\langle H \rangle = 4 \times 10^{21}$ erg s^{-1} (run 10, solid line; run 16, dashed line; run 18, dot-dashed line; run 20, triple-dot-dashed line).

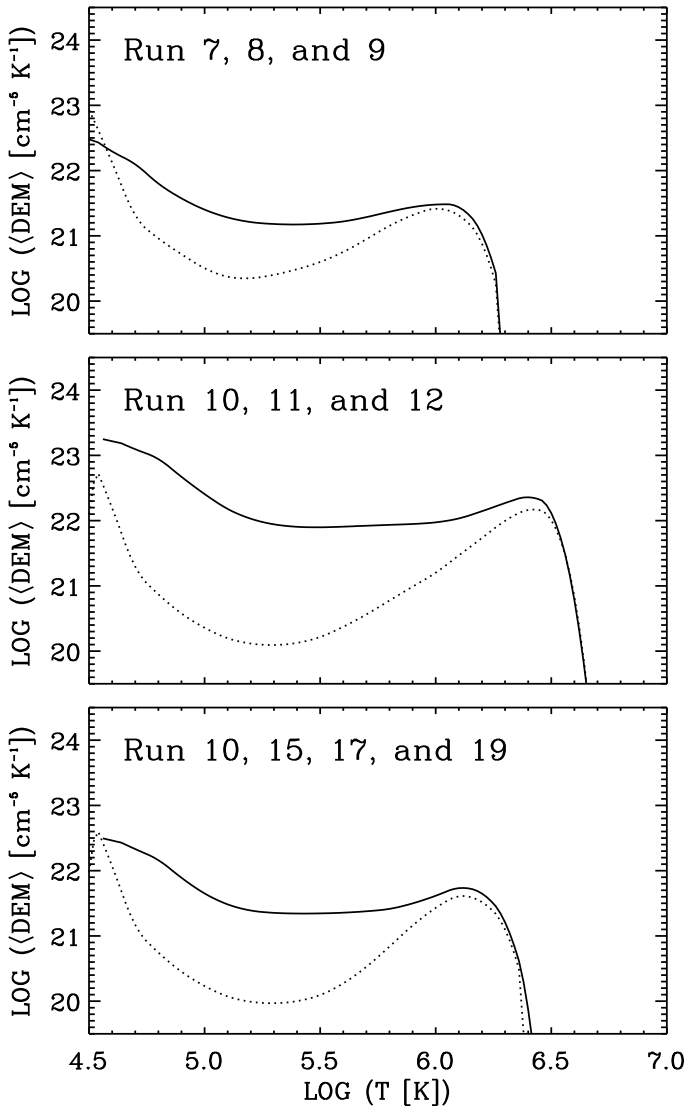

Figure 5.9: DEMs obtained by time-averaging together different localised impulsive models. *Top panel:* models with same cadence time ($t_C = 250$ s) and different pulse energies (run 7, 8, and 9). *Middle panel:* models with same cadence times ($t_C = 250$ s) and different pulse energies (run 10, 11, and 12). *Bottom panel:* models with same pulse energies ($H_P = 10^{24}$ erg) and different pulse candence times (run 10, 15, 17, and 19).

6

CONCLUSIONS

In this work we have performed hydrodynamic simulations of a multi-stranded coronal loop undergoing different kinds of heating regimes with a numerical code capable of resolving the transition region sections of the loop and following their evolution, outlining possible signatures of the heating regime in some plasma-related observables, such as Doppler-shifts of several EUV spectral lines and differential emission measure distributions.

We considered heating either uniformly distributed along the coronal part of the loop or localised close to the chromospheric footpoints, with a damping-length, λ, equal to $1/4$ of the loop semi-length and a 75% asymmetry between the heating-rates in the two legs of the loop. Moreover, we examined both the cases of steady and impulsive heating. Specifically, we varied the mean energy dissipated into the loop, $\langle H \rangle$, as well as the nanoflare cadence time, t_C (in the impulsive heating cases). The major findings of our analysis are summarised in Table 6.1.

Uniform or localised impulsive heating with a cadence time $\sim 1/4$ of the plasma cooling time, τ_{cool}, produces a plasma evolution that is essentially indistinguishable from the corresponding steady cases.

Localised heating yields a catastrophic cooling phase due to thermal non-equilibrium during the loop evolution for a limited range of heating parameters. Plasma condensation formation cycles occur when heating is steady or impulsive with cadence times significantly shorter than the loop cooling time (in our case $t_C = 1/4\,\tau_{cool}$) and mean energy rates below a certain threshold (here $\langle H \rangle \leq 4 \times 10^{21}$ erg s^{-1}). In these cases, a blob of material at chromospheric temperatures (set $\sim$ 30000 K in the model) forms along the less heated leg of the loop (owing to the gas pressure imbalance between the two sections in which the loop is divided by the blob itself), moves towards the corresponding foot-

Table 6.1: Summary of the results of this work.

Heating regime		Pulse cadence time	Pulse energy	General characteristics
Uniform	Steady	—	10^{24} erg	Steady state
	Impulsive	$\ll \tau_{cool}$	10^{24} erg	Steady state
		$\geq \tau_{cool}$	10^{24} erg	Dynamic state, moderate blue-shifts in coronal lines
Localised	Steady	—	10^{24} erg	Condensation cycle, strong red-shifts in TR lines
	Impulsive	$\ll \tau_{cool}$	$< 2 \times 10^{24}$ erg	Condensation cycle, strong red-shifts in TR lines
			$\geq 2 \times 10^{24}$ erg	No condensation, steady state
		$\geq \tau_{cool}$	$< 2 \times 10^{24}$ erg	Dynamic state, strong blue-shifts in coronal lines
			$\geq 2 \times 10^{24}$ erg	Highly dynamic state, moderate blue-shifts in coronal lines

point, and eventually falls onto the chromosphere with velocities of the order of 30 km s^{-1}.

We argue that the heating localisation is necessary to trigger condensation formation during the loop evolution, but it is not always sufficient. The crucial point is indeed the balance between the energy supplied to the loop top and the radiative losses therein. Hence, the variation of the heating parameters (such as the pulse cadence, the pulse energy, or the heating damping-length) with respect to the global characteristics of the model (the radiative cooling time or the loop length) could, in some cases, prevent the occurrence of a dynamic cycle of plasma condensation formation even in the presence of energy localisation. Our results show that this may happen, for instance, by increasing the heating rate at the loop footpoints or considering nanoflare cadence times comparable with or longer than the characteristic cooling time, but we know from previous works

that also increasing the ratio of the heating damping-length to the loop length can prevent the occurrence of thermal non-equilibrium.

However, we stress on the fact that it is the combination of all heating parameters (t_C, H_P, and λ), rather than the energy localisation alone, that affects the thermal stability of the loop during its evolution. As a future work, we plan to investigate to what extent the pulse energy threshold, that separates between condensation-forming and condensation-free models, depends on the ratio λ/L, in order to check whether loops that are quasi-stable in a given range of heating parameters become thermally unstable with an even more concentrated energy deposition.

An interesting implication of our results is that heating mechanisms that produce a footpoint-localised energy release can lead to very different final states that depend only on the magnitude of the mean dissipated energy. In this sense, the warm overdense and hot underdense loops recently observed by TRACE, SOHO, *Yohkoh*, and *Hinode* could be explained by the dynamic evolution of the plasma inferred from our models with high-frequency impulsive heating. In particular, heating producing plasma condensation cycles can give rise to warm ($T \simeq 2$ MK), overdense loops with lifetimes of some hours, such as those observed by TRACE and SOHO (e.g., Aschwanden et al., 1999, 2001; Winebarger et al., 2003). Moreover, the increase of the amount of energy supplied by each pulse prevents the plasma condensation formation and causes the loops to settle in a hot ($T \simeq 2$–3 MK), quasi-static, slightly overdense state, which can reproduce the case of hot loops seen by *Yohkoh* SXT (Porter & Klimchuk, 1995; Nitta, 2000) and *Hinode* XRT (Warren et al., 2009), without a spatially correlated warm counterpart. This explanation remains valid even if the loop is regarded as a bundle of nanoflare-heated strands, assuming that all the nanoflares within each strand have a similar magnitude and recur with a similar frequency. However, further investigation is necessary to determine how critical this assumption is.

Doppler-shifts computed for the spectral lines of C IV (λ1548 Å), O V (λ629 Å), Ne VIII (λ770 Å), and Mg X (λ610 Å) appear to be influenced in different ways by the heating regime.

In the uniform heating cases, the synthesised lines do not exhibit appreciable shifts of their centroids with respect to their rest wavelengths, irrespective of the

steadiness or impulsiveness of heating, due to the negligible dynamics characterizing these models.

Conversely, localised heating producing plasma condensations affects significantly lines that form at transition region temperatures ($T \simeq 0.1 - 0.5$ MK), such as the C IV and O V lines, which bear strong red-shifts (indicating downflows of up to ~ 20 km s^{-1}) located in proximity of the less heated footpoint of the loop. Downflows are the consequence of the falling of the condensations towards the solar surface. Observational evidence of persistent red-shifts in lower transition region lines, located close to the footpoint regions of coronal loops (e.g., Peter, 1999; Tripathi et al., 2008), might therefore be a signature of plasma condensation formation and, in turn, of thermal non-equilibrium due to localised heating occurring along the loops.

Coronal lines, such as the Mg X line, could help in discriminating between localised impulsive heating regimes in which the pulse cadence time is longer or shorter than the characteristic cooling time of the loop, since they exhibit rather pronounced blue-shifts (corresponding to upflows of ~ 20 km s^{-1}) located close to the loop footpoints when $t_C > \tau_{cool}$. Significant up-flows have been recently observed by *Hinode* EIS in spectral lines forming at coronal temperatures ($T \gtrsim 1$ MK) at the base of coronal loops (e.g., Hara et al., 2008; Brooks & Warren, 2009) or in sharp regions at the boundary of active regions (Del Zanna, 2008), but with velocities generally lower than those deduced from our calculations. This may indicate a predominance of conditions in which the cadence time is of the order or slightly longer than the plasma cooling time. Nanoflare repetition times shorter than those of the loop cooling produce, on the contrary, marginal blue-shifts (with velocities ~ 5 km s^{-1}) close to the strongly heated footpoint.

However, we underline that our results concerning Doppler-shifts are only a first approximation estimate, since we computed spectral emission assuming ionisation equilibrium. This assumption is strictly correct only when the time-scales of the temperature evolution are much longer than ionisation and recombination time-scales, but it has been pointed out that it may be almost valid in case of impulsive heating with very long nanoflare cadence times in a rarefied loop or short repetition times in a denser plasma (see, e.g., Reale & Orlando, 2008). A more complete analysis in which the effects of ionisation non-equilibrium are included in the computation of the spectral emissivity is in progress.

The differential emission measure (DEM) is found to be insensitive to the presence of condensation because the sequence of catastrophic cooling, sinking towards the loop footpoint, re-heating and evaporation does not effectively redistribute the temperature of plasma and the global distribution remains very close to the corresponding steady configuration. On the contrary, energy pulses with cadence times longer than the plasma cooling time produce temperature oscillations in the bulk of the plasma that effectively smear the coronal DEM structure. The effects are observable since the coronal DEM peak tends to disappear when the pulse cadence is about two times the plasma cooling time.

The DEM pronounced peak observed in active regions would indicate a predominance of conditions in which the cadence time is shorter or of the order of the plasma cooling time, whilst the structure of the quiet-Sun DEMs suggests a cadence time longer than the plasma cooling time. Nevertheless, our simulations are unable to reproduce both the transition region and the coronal DEM structure with a unique set of heating parameters, even in the case of composite loops with a more reasonable mixture of strands subject to different heating regimes, as obtained by averaging together different models. We conclude that the assumption of multi-stranded structures subject to localized impulsive heating is not sufficient to solve the long-standing problem of the transition region and coronal emission and that some other physical processes, like that proposed by Judge (2008), Klimchuk et al. (2008), and De Pontieu et al. (2009) must be taking place.

Comparing the results of the current calculations with detailed observations could help in placing further constraints on the spatial and temporal characteristics of coronal heating mechanisms in a more quantitative way. High-resolution and high-speed spectroscopic observations are critically needed as well to isolate the important small-scale structures (i.e., magnetic strands or current-sheets between the magnetic flux tubes) that are presently not resolved and for a diagnostic of the rapid plasma evolution produced by impulsive heating.

ACKNOWLEDGEMENTS

I wish to gratefully acknowledge helpful and invaluable discussions with Prof. Eric Priest, Dr. Claire Parnell, Dr. Spiro Antiochos, Dr. Jim Klimchuk, Prof. Fabio Reale, and Dr. Robert Walsh. Special thanks go to Prof. Lucio Paternò, Dr. Daniele Spadaro, Prof. Alessandro Lanzafame, and Dr. Nuccio Lanza. This work was supported in part by the Agenzia Spaziale Italiana (contract I/015/07/0 and agreement ASI/INAF I/023/09/0). Financial support by the European Commission through the SOLAIRE Network (MTRN-CT-2006-035484) is also acknowledged.

REFERENCES

Antiochos, S. K. 1980, ApJ, 236, 270

Antiochos, S. K., MacNeice, P. J., Spicer, D. S., & Klimchuk, J. A. 1999, ApJ, 512, 985

Antiochos, S. K., MacNeice, P. J., & Spicer, D. S. 2000, ApJ, 536, 494

Antiochos, S. K., & Sturrock, P A. 1978,ApJ, 220, 1137

Antolin, P. & Shibata, K. 2009, ApJ, submitted

Anzer, U., & Heinzel, P. 2000, A&A, 358, L75

Arnaud, M., & Rothenflug, R. 1985, A&AS, 60, 425

Arnaud, M., & Raymond, J. 1992, ApJ, 398, 394

Aschwanden, M. J. 2002, ApJ, 580, L79

Aschwanden, M. J. 2004, *Physics of the Solar Corona*, Springer

Aschwanden, M. J., Newmark, J. S., Delaboudinière, J.-P., Neupart, W. M., Klimchuk, J. A., Gary, G. A. et al. 1999, ApJ, 515, 842

Aschwanden, M. J., Nightingale, R. W., & Alexander, D. 2000, ApJ, 541, 1059

Aschwanden, M., Schrijver, C. J., & Alexander, D. 2001, ApJ, 550, 1036

Brooks, D. H. & Warren, H. P. 2009, ApJ, submitted

Brosius, J. W., Davila, J. M., Thomas, R. J., & Monsignori Fossi, B. C. 1996, ApJS, 106, 143

Cargill, P. J. 1994, ApJ, 422, 381

Cargill, P. J. & Klimchuk, J. A. 2004, ApJ, 605, 911

Cook, J. W., Cheng, C. C., Jacobs, V. L. et al. 1989, ApJ, 338, 1176

Cox, D. P. & Tucker, W. H. 1969, ApJ, 157, 1157

Craig, I. J. D. & Brown, J. C. 1976, A&A, 49, 239

Craig, I. J. D., McClymont, A. N., & Underwood, J. H. 1978, A&A, 70, 1

De Pontieu, B., Hansteen, V. H., McIntosh, S. W., & Patsourakos, S. 2009, ApJ, 702, 1016

Dahlburg, R. B., Klimchuk, J. A., & Antiochos, S. K. 2003, Adv. Space Res. 32, 1029

Dahlburg, R. B., Klimchuk, J. A., & Antiochos, S. K. 2005, ApJ, 622, 1191

De Groof, A., Berghmans, D., van Driel-Gesztelyi, L., & Poedts, S. 2004, A&A, 415, 1141

Del Zanna, G. 2008, A&A, 481, L49

Del Zanna, G., & Mason, H. E. 2003, A&A, 406, 1089

Dere, K. P., Landi, E., Mason, H. E., Monsignori Fossi, B. C., & Young, P. R. 1997, A&AS, 125, 149

Dere, K. P., & Mason, H. 1981, *Solar Active Regions*, Colorado Associated Univ. Press, 129

Edlén, B. 1942, Zs. Ap. 22, 30

Feldman, U. 1992, *Physica Scripta*, 46, 202

Field, G. B. 1965, ApJ, 142, 531

Golub, L. & Pasachoff, J. M. 1997, *The Solar Corona*, Cambridge Univ. Press

Grotrian, W. 1939, *Naturwissenschaften*, 27, 214

Gudiksen, B., & Nordlund, A. 2005, ApJ, 618, 1020

Hara, H., Watanabe, T., Harra, L. K., et al. 2008, ApJ, 678, L67

Hirsch, C. 1990, *Numerical Computation of Internal and External Flows*, Wiley

Hollweg, J. V. 1981, Sol. Phys., 70, 25

Hollweg, J. V. 1984, ApJ, 277, 392

Ionson, J. A. 1978, ApJ, 226, 65

Judge, P. 2008, ApJ, 683, L87

Karpen, J. T., Antiochos, S. K., Hohensee, M., Klimchuk, J. A., & MacNeice, P. J. 2001, ApJ, 553, L85

Karpen, J. T., Antiochos, S. K., Klimchuk, J. A., & MacNeice, P. J. 2003, ApJ, 593, 1187

Karpen, J. T., Antiochos, S. K., & Klimchuk, J. A. 2006, ApJ, 637, 531

Karpen, J. T. & Antiochos, S. K. 2008, ApJ, 676, 658

Kjeldseth-Moe, O., & Brekke, P. 1998, Sol. Phys., 182, 73

Klimchuk, J. A. 2000, Sol. Phys., 193, 53

Klimchuk, J. A. 2006, Sol. Phys., 234, 41

Klimchuk, J. A. & Cargill, P. J. 2001, ApJ, 553, 440

Klimchuk, J. A., Karpen, J. T., & Antiochos, S. K. 2009, ApJ, submitted

Klimchuk, J. A., Patsourakos, S., & Cargill, P. J. 2008, ApJ, 682, 1351

Landi, E., Landini, M., Dere, K. P. et al. 1999, A&AS, 135, 339

Landini, M. & Monsignori Fossi, B. C. 1990, A&AS., 82, 229

Laney, C. B. 1998, *Computational Gasdynamics*, Cambridge Univ. Press

Lanzafame, A. C., Brooks, D. H., Lang, J., Summers, H. P., Thomas, R. J., & Thompson, A. M. 2002, A&A, 384, 242

Lanzafame, A. C., Brooks, D. H., & Lang, J. 2005, A&A, 432, 1063

López Fuentes, M. C., Klimchuk, J. A., & Démoulin, P. 2006, ApJ, 639, 459

MacNeice, P. J., Olson, K. M., Mobarry, C., de Fainchtein, R., & Packer, C. 2000, Comput. Phys. Commun., 126, 330

Mariska, J. T. 1992, *Solar Transition Region*, Cambridge Univ. Press

Martens, P. C. H., Cirtain, J. W., & Schmelz, J. T. 2002, ApJ, 577, L115

Martens, P. C. H., Kankelborg, C. C., & Berger, T. E. 2000, ApJ, 537, 471

Meyer, J.-P. 1985, ApJS, 57, 173

Müller, D. A. N., Hansteen, V. H., & Peter, H. 2003, A&A, 411, 605

Müller, D. A. N., Peter, & H., Hansteen, V. H. 2004, A&A, 424, 289

Nagata, S., Hara, H., Kano, R., Kobayashi, K., Sakao, T., Shimizu, T. et al. 2003, ApJ, 590, 1095

Narain, U. & Ulmschneider, P. 1996, Space Sci. Rev. 75, 453

Neupert, W. M., et al. 1998, Sol. Phys., 183, 305

Nitta, N. 2000, Sol. Phys., 195, 123

Ofman, L., Klimchuk, J. A., & Davila, J. M. 1998, ApJ, 493, 474

Orlando, S., Bocchino, F., & Peres, G. 1999, A&A, 346, 1003

O'Shea, E., Banerjee, D., & Doyle, J. G. 2007, A&A, 475, L25

Parker, E. N. 1953, ApJ, 117, 431

Parker, E. N. 1983, ApJ, 264, 642

Parker, E. N. 1988, ApJ, 330, 474

Patsourakos, S., Klimchuk, J. A., & MacNeice, P. J. 2004, ApJ, 603, 322

Patsourakos, S. & Klimchuk, J. A. 2005, ApJ, 628, 1023

Peter, H. 1999, ApJ, 516, 490

Peter, H., Gudiksen, B. V., & Nordlund, A. 2006, ApJ, 638, 1086

Petschek, H. E. 1964, Proc-1964-Hess, 425

Poedts, S., Belien, J. C., & Goedbloed, J. P. 1994, Sol. Phys., 151, 271

Porter, L. J. & Klimchuk, J. A. 1995, ApJ, 454, 499

Priest, E. R. 1982, *Solar Magneto-hydrodynamics*, Kluwer Academic Publishers

Priest, E. R., Foley, C. R., Heyvaerts, J., Arber, T. D., Culhane, J. L., & Acton, L. W. 1998, Nature, 393, 545

Raymond, J. C. & Doyle, J. G. 1981, ApJ, 247, 686

Reale, F. 2002, ApJ, 580, 566

Reale, F., Nigro, G., Malara, F., Peres, G., & Veltri, P. 2005, ApJ, 633, 489

Reale, F. & Orlando, S. 2008, ApJ, 684, 715

Rosner, R., Tucker, W. H., & Vaiana, G. S. 1978, ApJ, 220, 643

Schmelz, J. T., Scopes, R. T., Cirtain, J. W., Winter, H. D., & Allen, J. D. 2001, ApJ, 556, 896

Schmelz, J. T. 2002, ApJ, 578, L161

Schmelz, J. T., Cirtain, J. W., Beene, J. E., Blevins, H. T., Ellis, D., Medlin, D. A., Nasraoui, K., & Nevels, C. 2003, Adv. Space Res., 32, 1109

Schmelz, J. T., Nasraoui, K., Rightmire, L. A., Kimble, J. A., Del Zanna, G., Cirtain, J. W., DeLuca, E. E., & Mason, H. E. 2009, ApJ, 691, 503

Schmieder, B., Rust, D. M., Georgoulis, M. K., Demoulin, P., & Bernasconi, P. N. 2004, ApJ, 601, 530

Schrijver, C. J., Sandman, A. W., Aschwanden, M. J., & DeRosa, M. L. 2004, ApJ, 615, 512

Serio, S., Peres, G., Vaiana, G. S., Golub, L., & Rosner, R. 1981, ApJ, 243, 288

Serio, S., Reale, F., Jakimiec, J., Sylwester, B., & Sylwester, J. 1991, A&A, 241, 197

Spadaro, D., Lanza, A. F., Lanzafame, A. C., Karpen, J. T., Antiochos, S. K., Klimchuk, J. A., & MacNeice, P. J. 2003, ApJ, 582, 486

Spitzer, L. 1962, *Physics of Fully Ionized Gases*, Interscience New York

Stern, R., Wang, R., & Bowyer, S. 1978, ApJS, 37, 195

Testa, P., Peres, G., & Reale, F. 2005, ApJ, 622, 695

Tripathi, D., Mason, H. E., Young, P. R., & Del Zanna, G. 2008, A&A, 481, L53

Ulrich, R. K. 1996, ApJ, 465, 436

Van Leer, B. 1979, J. Comput. Phys., 32, 101

Walsh, R. W., Bell, G. E., & Hood, A. W. 1997, Sol. Phys., 171, 81

Warren, H. P. & Winebarger, A. R. 2006, ApJ, 645, 711

Warren, H. P., Winebarger, A. R., & Brooks, D. H. 2009, ApJ, submitted

Winebarger, A. R., Warren, H. P., & Mariska, J. T. 2003, ApJ, 587, 439

Winebarger, A. R. & Warren, H. P. 2005, ApJ, 626, 543

Withbroe, G. L. & Noyes, R. W. 1977, Ann. Rev. A&A15, 363

Wragg, M. A. & Priest, E. R. 1982, Sol. Phys., 80, 309

APPENDICES

A

FIGURES NOT INCLUDED IN THE TEXT

In this section we report all the figures relevant to runs that are not explicitly discussed in Chapters 4 and 5. They are ordered following the same scheme as in the text. A brief description of the main features can be found in the respective labels.

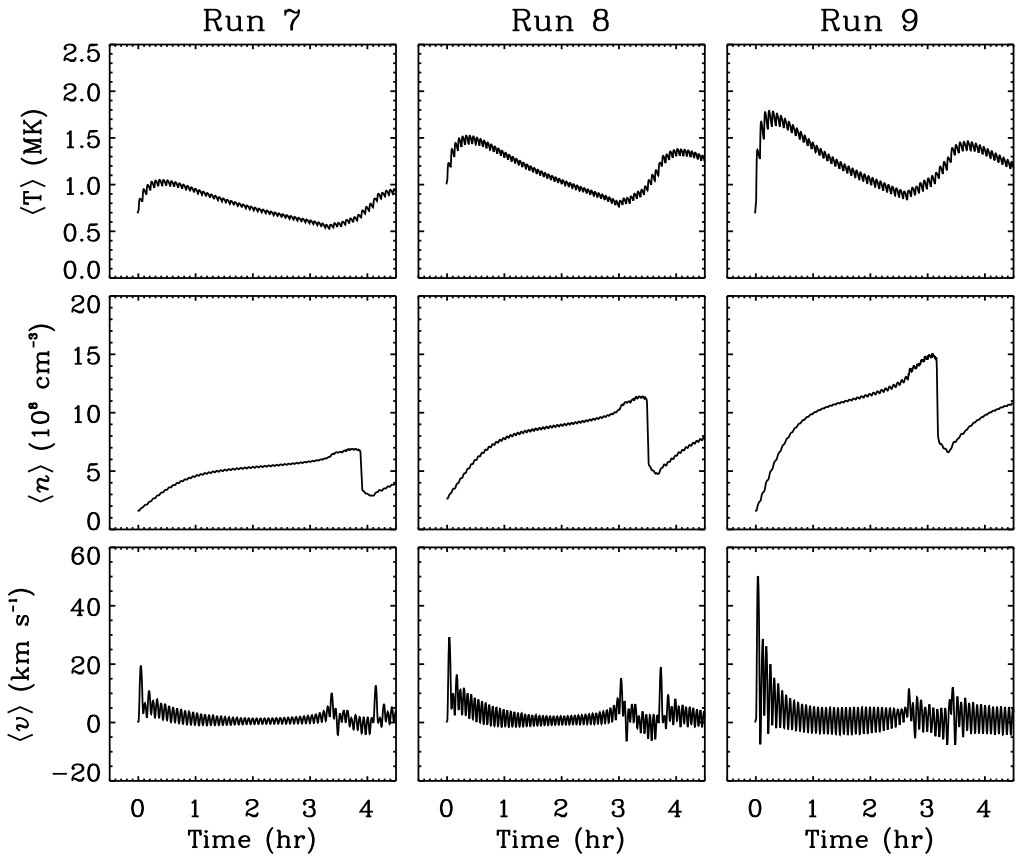

Figure A.1: Initial part of the temporal evolution of the loop model temperature (top panels), density (middle panels), and velocity (bottom panels), averaged over the upper 3/4 of the loop coronal part, for run 7 ($t_C = 250$ s, $H_P = 0.125 \times 10^{24}$ erg, left panels), 8 ($t_C = 250$ s, $H_P = 0.25 \times 10^{24}$ erg, middle panels), and 9 ($t_C = 250$ s, $H_P = 0.5 \times 10^{24}$ erg, right panels). In all cases a condensation develops between the midpoint and the right footpoint of the loop.

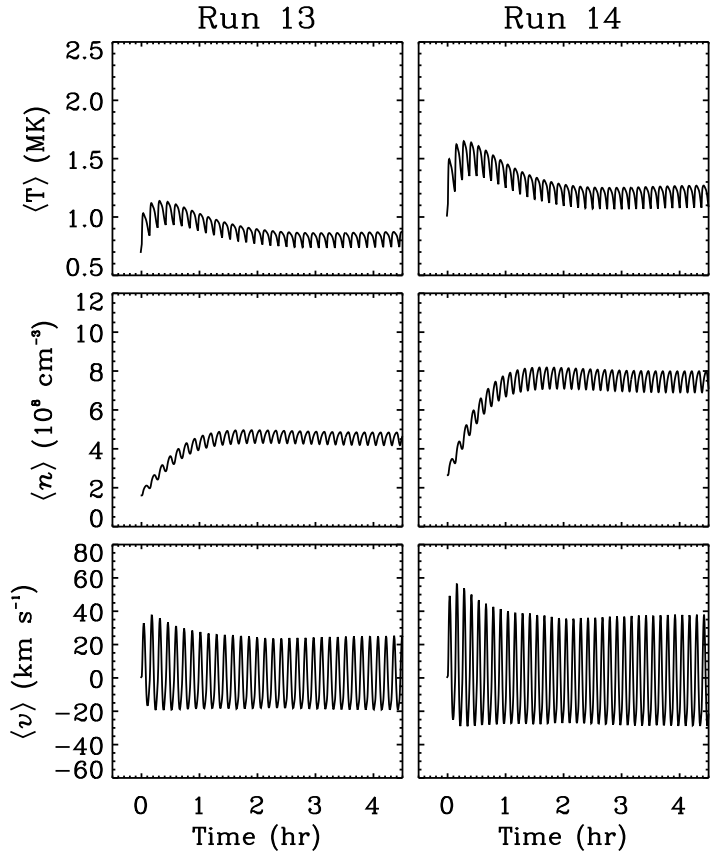

Figure A.2: Same as in Fig. A.1, for run 13 ($t_C = 500$ s, $H_P = 0.25 \times 10^{24}$ erg, left panels) and 14 ($t_C = 500$ s, $H_P = 0.5 \times 10^{24}$ erg, right panels). In these cases condensation formation does not occur.

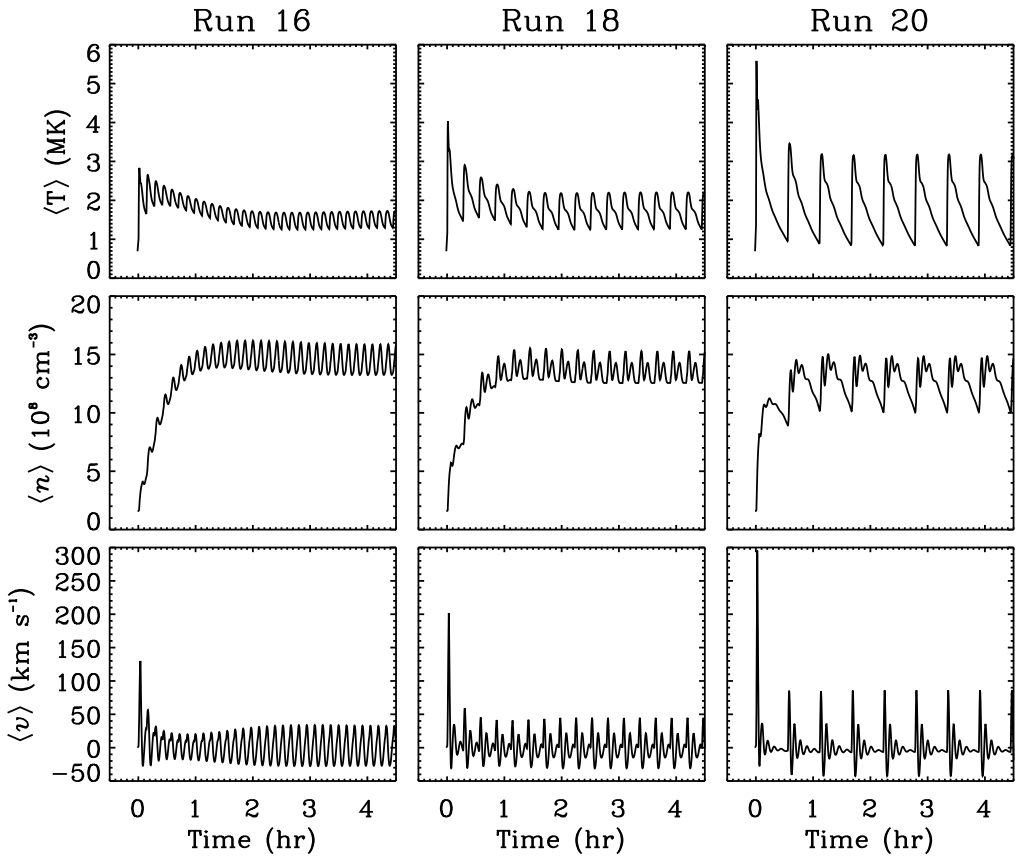

Figure A.3: Same as in Fig. A.1, for run 16 ($t_C = 500$ s, $H_P = 2 \times 10^{24}$ erg, left panels), 18 ($t_C = 1000$ s, $H_P = 4 \times 10^{24}$ erg, middle panels), and 20 ($t_C = 2000$ s, $H_P = 8 \times 10^{24}$ erg, right panels). Note that in these cases the mean energy dissipated into the loop is the same ($\langle H \rangle = 4 \times 10^{21}$ erg s^{-1}).

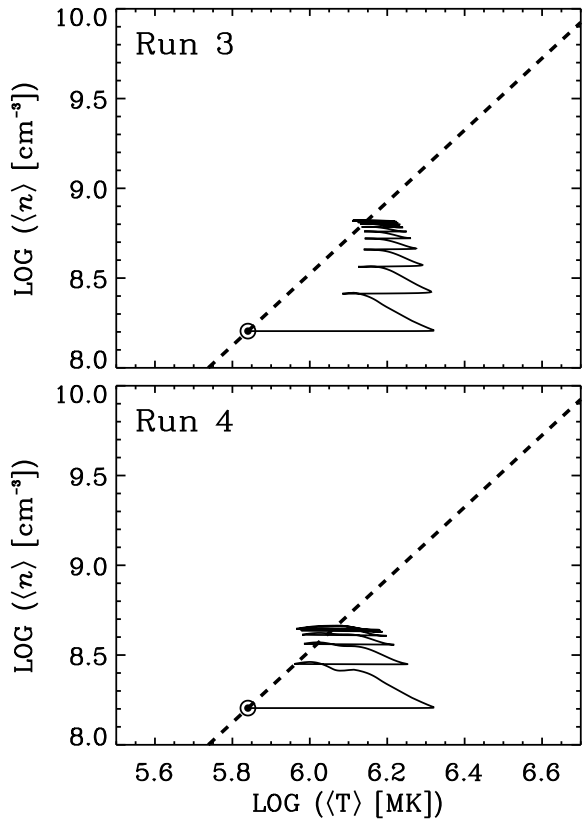

Figure A.4: Evolution of the mean loop density and temperature the uniform heating cases of run 3 ($t_C = 500$ s, $H_P = 10^{24}$ erg, top panel), and 4 ($t_C = 1000$ s, $H_P = 10^{24}$ erg, bottom panel). The hydrostatic scaling law (thick dashed line, see Eq. 4.6) is also reported, gauged according to the initial quasi-static state (indicated by the dotted circle). Note that no condensation forms in these cases.

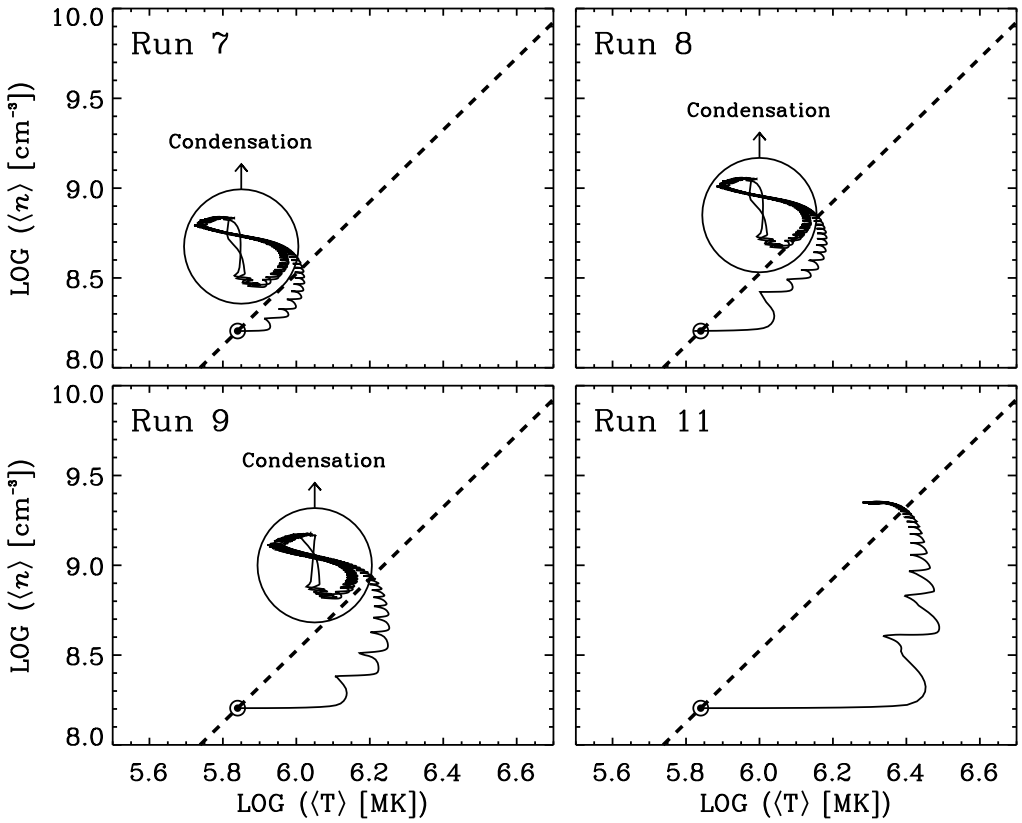

Figure A.5: Same as in Fig. A.4, for run 7 ($t_C = 250$ s, $H_P = 0.125 \times 10^{24}$ erg, top-left panel), 8 ($t_C = 250$ s, $H_P = 0.25 \times 10^{24}$ erg, top-right panel), 9 ($t_C = 250$ s, $H_P = 0.5 \times 10^{24}$ erg, bottom-left panel), and 11 ($t_C = 250$ s, $H_P = 2 \times 10^{24}$ erg, bottom-right panel). In the top and bottom-left panels, the evolution characterised by condensation formation cycles occurs within the encircled region labelled "condensation". Run 11 does not develop condensations.

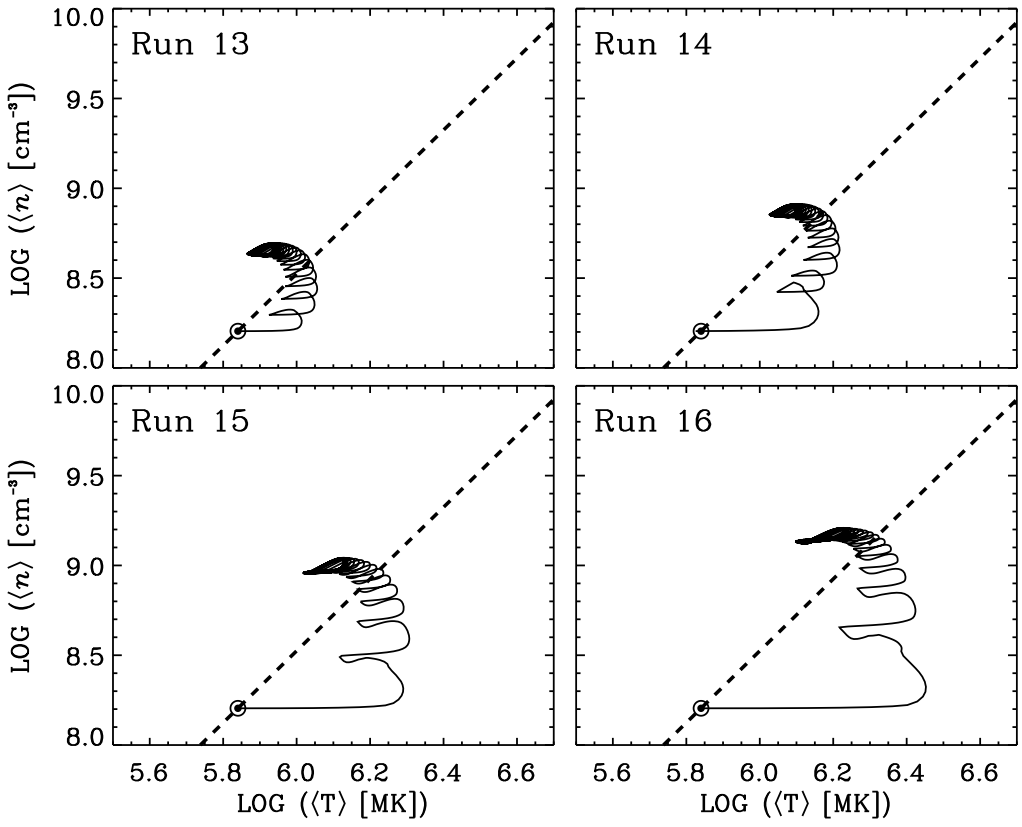

Figure A.6: Same as in Fig. A.4, for run 13 ($t_C = 500$ s, $H_P = 0.25 \times 10^{24}$ erg, top-left panel), 14 ($t_C = 500$ s, $H_P = 0.5 \times 10^{24}$ erg, top-right panel), 15 ($t_C = 500$ s, $H_P = 10^{24}$ erg, bottom-left panel), and 16 ($t_C = 500$ s, $H_P = 2 \times 10^{24}$ erg, bottom-right panel).

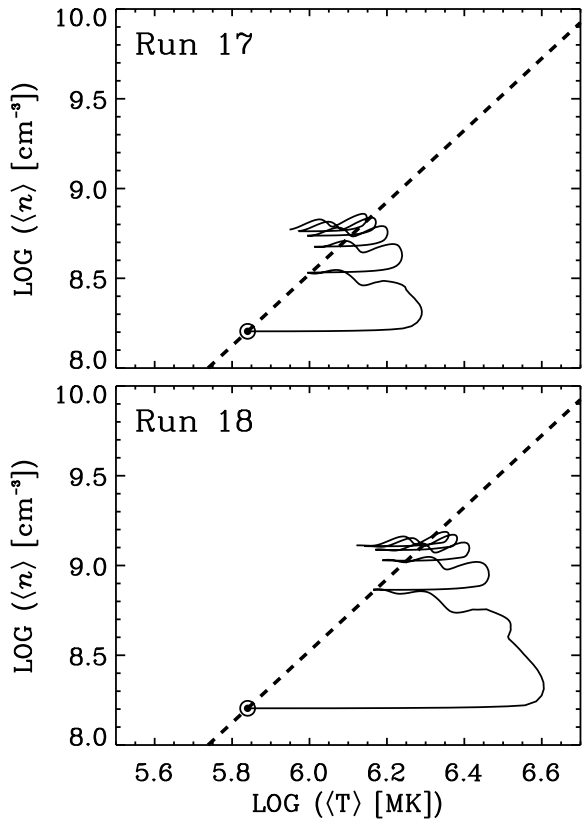

Figure A.7: Same as in Fig. A.4, for run 17 ($t_C = 1000$ s, $H_P = 10^{24}$ erg, top panel), and 16 ($t_C = 500$ s, $H_P = 4 \times 10^{24}$ erg, bottom panel).

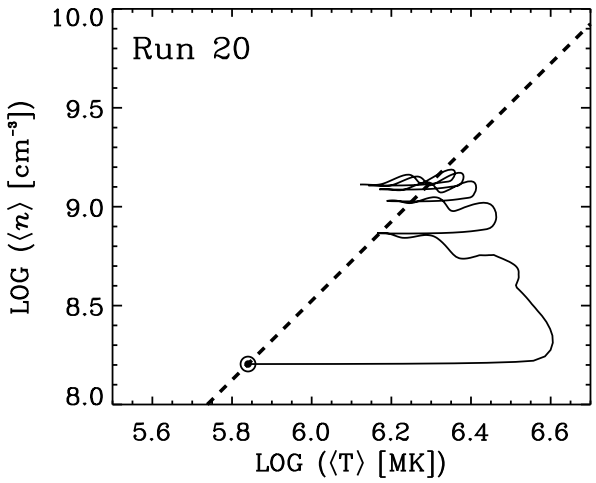

Figure A.8: Same as in Fig. A.4, for run 20 ($t_C = 2000$ s, $H_P = 8 \times 10^{24}$ erg).

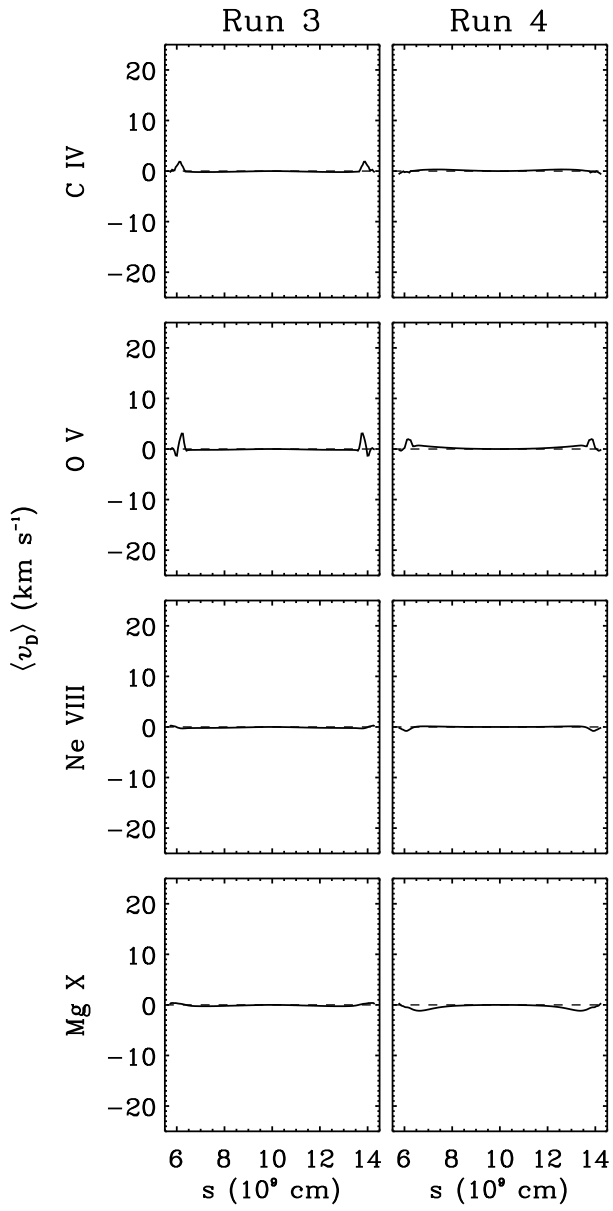

Figure A.9: Time-averaged Doppler velocities, deduced from the synthesised emission in the lines of C IV (λ1548 Å), O V (λ629 Å), Ne VIII (λ770 Å), and Mg X (λ610 Å), plotted versus distance along the coronal part of the loop, for the uniform heating models of run 3 ($t_C = 500$ s, $H_P = 10^{24}$ erg, left panels) and 4 ($t_C = 1000$ s, $H_P = 10^{24}$ erg, right panels). Note that positive (negative) velocities correspond to downflows (upflows).

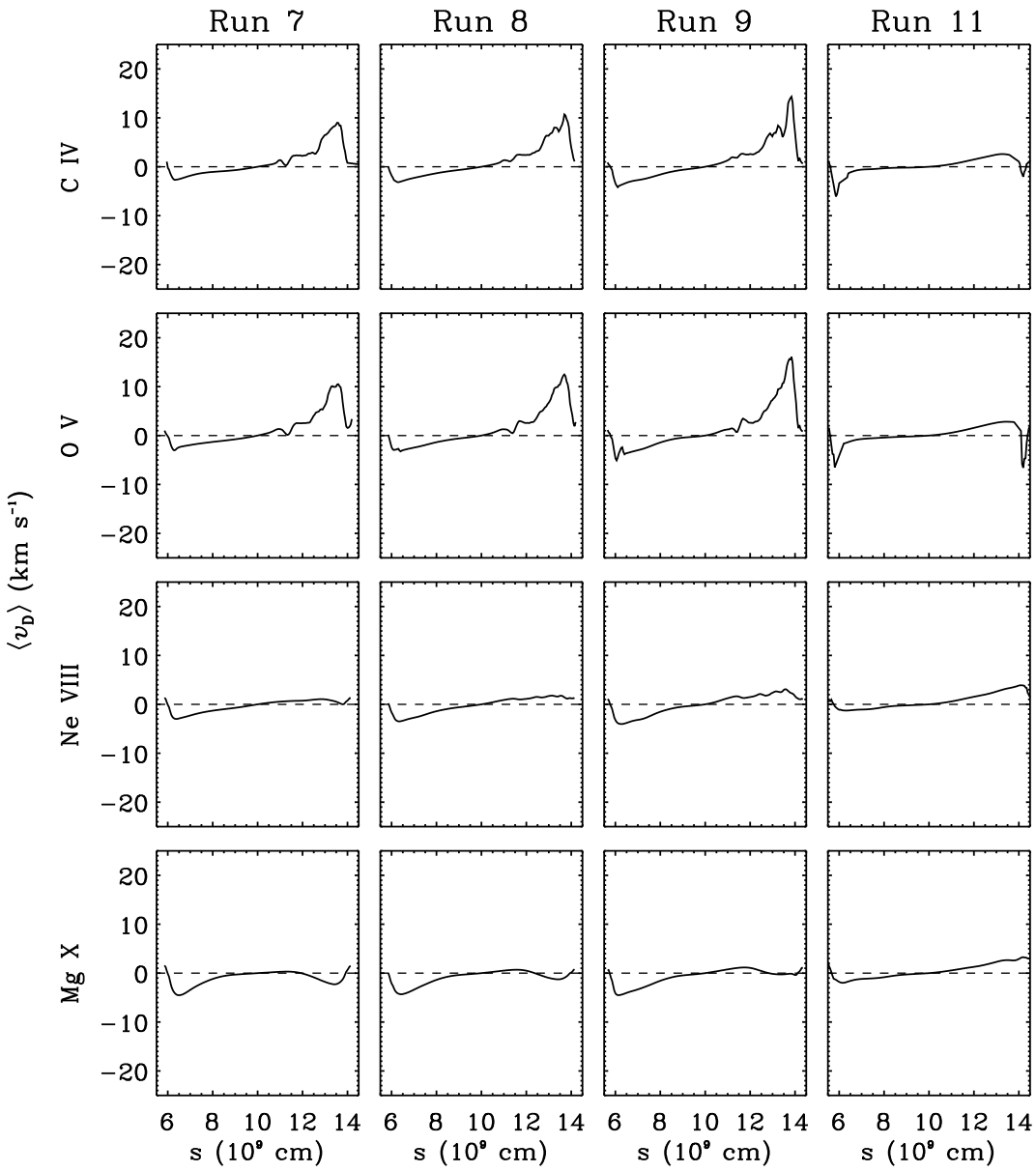

Figure A.10: Same as in Fig. A.9, for run 7 ($t_C = 250$ s, $H_P = 0.125 \times 10^{24}$ erg, left column), 8 ($t_C = 250$ s, $H_P = 0.25 \times 10^{24}$ erg, second column), 9 ($t_C = 250$ s, $H_P = 0.5 \times 10^{24}$ erg, third column), and 11 ($t_C = 250$ s, $H_P = 2 \times 10^{24}$ erg, right column). Condensation forming runs exhibit rather pronounced red-shifts in transition region lines (O V and C IV lines), indicating downflows of up to $\sim 15 - 20$ km s^{-1} located near the right footpoint of the loop.

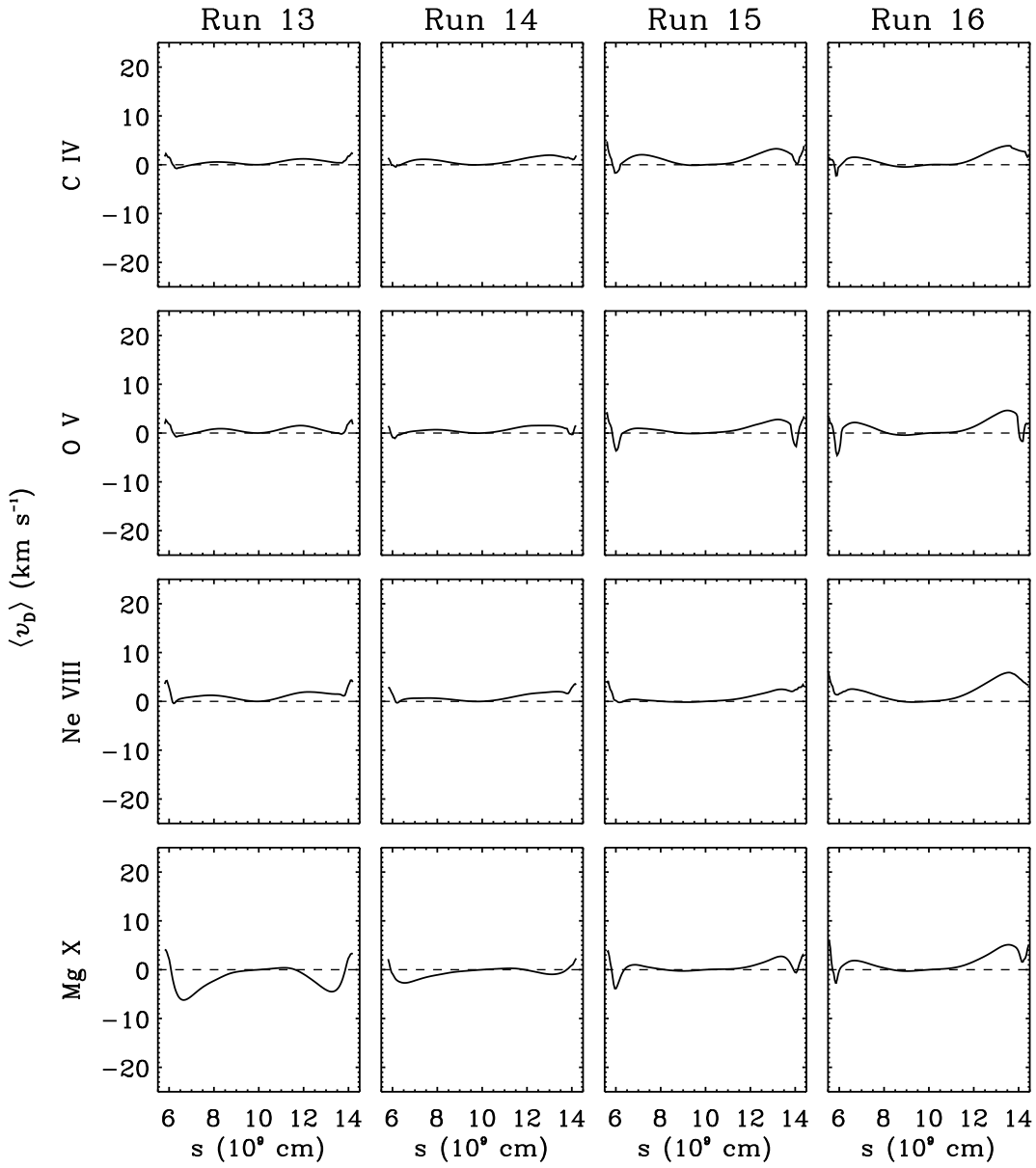

Figure A.11: Same as in Fig. A.9, for run 13 ($t_C = 500$ s, $H_P = 0.25 \times 10^{24}$ erg, left column), 14 ($t_C = 500$ s, $H_P = 0.5 \times 10^{24}$ erg, second column), 15 ($t_C = 500$ s, $H_P = 10^{24}$ erg, third column), and 16 ($t_C = 500$ s, $H_P = 2 \times 10^{24}$ erg, right column).

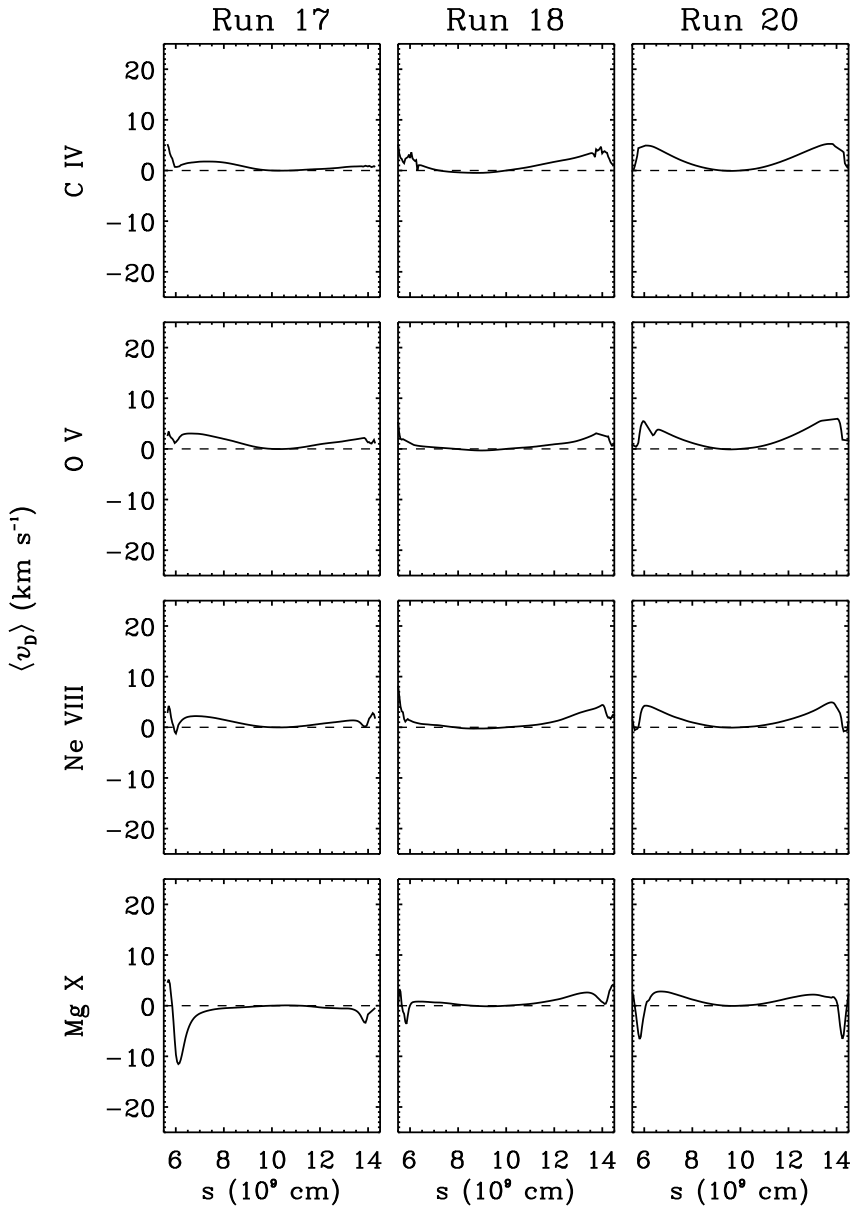

Figure A.12: Same as in Fig. A.9, for run 17 ($t_C = 1000$ s, $H_P = \times 10^{24}$ erg, left panels), 18 ($t_C = 1000$ s, $H_P = 4 \times 10^{24}$ erg, middle panels), and 20 ($t_C = 2000$ s, $H_P = 8 \times 10^{24}$ erg, right panels).

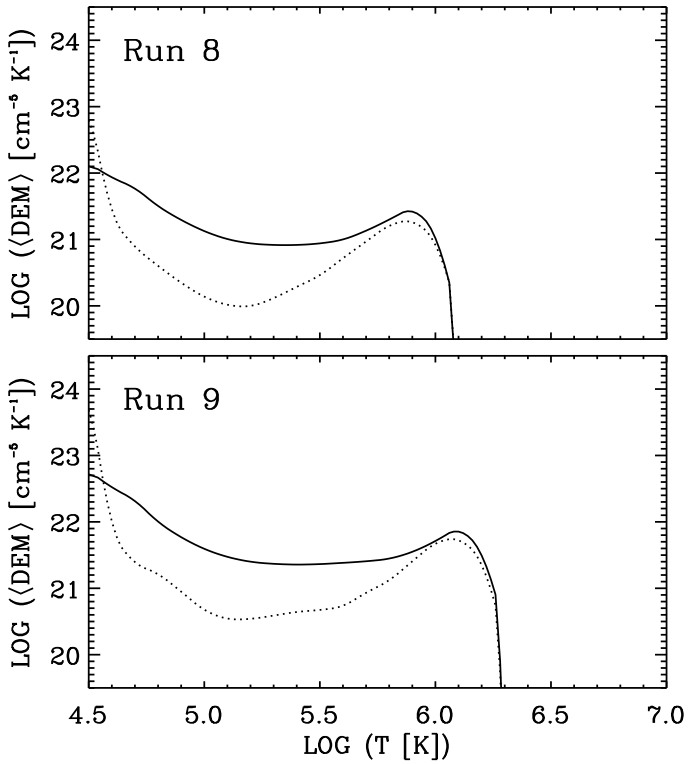

Figure A.13: Average differential emission measure (DEM) computed for run 8 (t_C = 250 s, $H_P = 0.25 \times 10^{24}$ erg, top panel) and 9 ($t_C = 250$ s, $H_P = 0.5 \times 10^{24}$ erg, bottom panel), both including (solid lines) and excluding (dotted lines) from calculation all the grid cells located less than 10 Mm above the footpoints (in order to consider or avoid the contribution of the transition region sections of the loop, respectively).

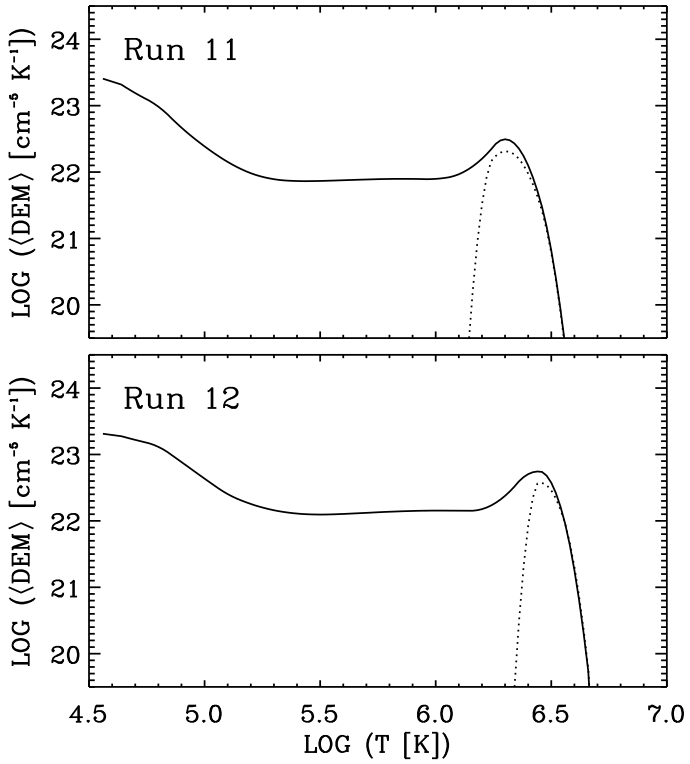

Figure A.14: Same as in Fig. A.13, for run 11 ($t_C = 250$ s, $H_P = 2 \times 10^{24}$ erg, top panel) and 12 ($t_C = 250$ s, $H_P = 4 \times 10^{24}$ erg,bottom panel).

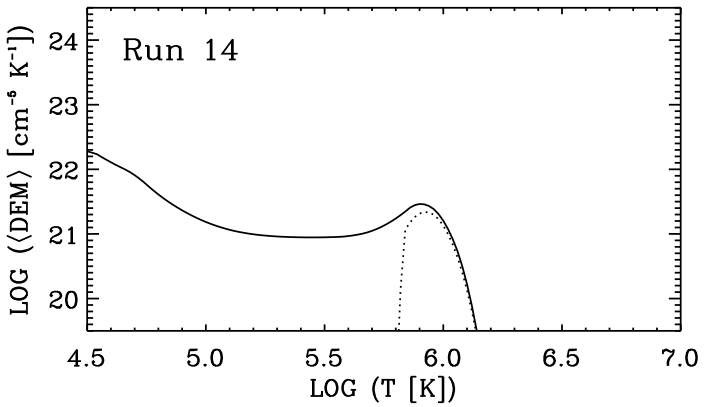

Figure A.15: Same as in Fig. A.13, for run 14 ($t_C = 500$ s, $H_P = 0.5 \times 10^{24}$ erg).

B

PUBLICATIONS

Signatures of impulsive localized heating in the temperature distribution of multi-stranded coronal loops

R. Susino[1,2], A. C. Lanzafame[1,2], A. F. Lanza[2], and D. Spadaro[2]

Received _____; accepted _____

[1]Dipartimento di Fisica e Astronomia - Sezione Astrofisica, Università di Catania, via S. Sofia 78, I-95123 Catania, Italy

[2]INAF-Osservatorio Astrofisico di Catania, via S. Sofia 78, I-95123 Catania, Italy

ABSTRACT

We study the signatures of coronal heating on the differential emission measure (DEM) by means of hydrodynamic simulations capable of resolving the chromospheric-corona transition region sections of multi-stranded coronal loops and following their evolution. We consider heating either uniformly distributed along the loop or localized close to the chromospheric footpoints, in both steady and impulsive regimes. Our simulations show that condensation at the top of the loop forms when the impulsive heating, with a pulse cadence lower than the plasma cooling time, is localized at the loop footpoints and the pulse energy is below a threshold above which the heating balances the radiative losses, thus preventing the catastrophic cooling which triggers the condensation. A condensation does not produce observable signatures in the DEM because it does not redistribute the plasma over a sufficiently large temperature range. On the other hand, the DEM coronal peak is found sensitive to the pulse cadence time when this is longer or comparable to the plasma cooling time. In this case, the heating pulses produce large oscillations in temperature in the bulk of the coronal plasma, which effectively smears out the coronal DEM structure. The pronounced DEM peak observed in active regions would indicate a predominance of conditions in which the cadence time is shorter or of the order of the plasma cooling time, whilst the structure of the quiet Sun DEM suggests a cadence time longer than the plasma cooling time. Our simulations give an explanation of the warm overdense and hot underdense loops observed by TRACE, SOHO and *Yohkoh*. However, they are unable to reproduce both the transition region and the coronal DEM structure with a unique set of parameters, which outlines the need for a more realistic description of the transition region.

Subject headings: Hydrodynamics; Sun: corona; Sun: transition region; Sun: UV radiation

1. Introduction

Solving the problem of the heating of the solar corona is one of the major issues in solar physics. In particular, the question whether the plasma heating inside coronal structures is the effect of steady or impulsive processes, uniform or localized within the structure, is still open.

Since the earliest observations, the solar corona appeared as composed by discrete bright structures, called coronal loops, consisting of magnetic flux tubes in which the hot and dense plasma is confined by the magnetic field. Coronal loops are characterized by different lengths, temperatures, activity levels, and appear to evolve with lifetimes of the order of several hours. The first models of loop heating (e.g., Rosner et al. 1978; Serio et al. 1981) considered flux tubes of constant cross-section filled with plasma in hydrostatic equilibrium, and in energy balance under the effects of uniform steady heating, conductive heat flux, and radiative losses. These models predict scaling laws relating the temperature, density, and length of a loop, and allow us to reproduce quite satisfactorily the X-rays coronal emission of both the Sun and solar-type stars.

Nevertheless, recent TRACE and SOHO observations have provided evidence that a large majority of warm coronal loops ($T \sim 1$–2 MK), although appearing in quasi-static conditions, are indeed over dense (Aschwanden et al. 1999, 2001; Winebarger et al. 2003; Patsourakos et al. 2004), while hot loops ($T > 2$ MK) observed by *Yohkoh* exhibit lower densities than predicted by loop models in hydrostatic equilibrium (Porter & Klimchuk 1995). These discrepancies could be explained if coronal loops are assumed to consist of unresolved magnetic strands, each of them heated impulsively and non-uniformly, at different times from its neighbors (Cargill 1994; Klimchuk & Cargill 2001; Spadaro et al. 2003; Cargill & Klimchuk 2004; Reale et al. 2005; Patsourakos & Klimchuk 2005; Klimchuk 2006; Klimchuk et al. 2008). The idea of impulsive coronal heating was firstly proposed by

Parker (1983, 1988), who introduced the concept of nanoflare, a local small-scale ($\lesssim 100$ km) event in which roughly 10^{24} erg of energy are released in the corona by magnetic field reconnection, after the magnetic stresses induced on the flux tubes by photospheric motions have reached a certain threshold.

In this Paper we investigate the response of magnetic loop plasma to different kinds of energy deposition by performing numerical simulations with a code capable of resolving the chromospheric-coronal transition region sections of the loop and following them as they respond to heating variations. We consider heating either uniformly distributed along the loop or localized close to the chromospheric footpoints, in both steady-state and impulsive regimes. In the impulsive case, we consider different values for the cadence of the injection of the energy pulses into the coronal segment of the loop, in order to perform a first comprehensive study of the consequences of the variation of such a parameter for the loop structure and evolution. The hydrodynamic behavior of coronal loops undergoing different heating regimes and the relevant consequences on the differential emission measure are discussed in detail, together with the indications that the variety of conditions found in this exploration give on the physical origins of coronal heating and related phenomena.

2. Numerical model and simulations

We performed numerical simulations of coronal loop hydrodynamics under different heating conditions using ARGOS (Antiochos et al. 1999; MacNeice et al. 2000), a one-dimensional code that solves the standard set of equations for the conservation of mass, momentum and energy by means of a high-order Godunov scheme and an adaptive mesh refinement. ARGOS also properly accounts for the heat flux saturation that may occur in some low-density and high-temperature regimes (see, e.g., Klimchuk 2006).

We considered a flux tube with a 80 Mm long coronal segment, to model typical active region loops, as observed, for instance, by TRACE. A detailed description of the characteristic features of the loop model can be found in Spadaro et al. (2003).

The loop was initially settled to a nearly stable equilibrium state under the action of a spatially uniform and temporally constant background heating (as described, e.g, in Antiochos et al. 1999, 2000). A heating rate $E_{\rm base} = 2 \times 10^{-5}$ erg cm^{-3} s^{-1} was chosen, according to the canonical hydrostatic scaling laws (see Rosner et al. 1978), to get an apex temperature of about 0.75 MK at the end of the relaxation phase. At this stage, the loop structure is that of a steady loop as in Rosner et al. (1978). The uniform background heating applied to achieve the initial equilibrium was turned off, within the coronal segment of the loop, when we started the additional heating ($t = 0$) and remained off for the remaining of the simulation. In the chromospheric part of the loop, the $E_{\rm base}$ heating was maintained throughout the simulation, although it has a little influence on the loop hydrodynamics, due to the high density in the chromosphere.

The additional heating rate, $E(s,t)$, is assumed to be a separable function of the curvilinear coordinate along the field lines, s, and of the time, t:

$$E(s,t) = F(s) \cdot G(t) \ \left[\text{erg cm}^{-3}\ \text{s}^{-1}\right]. \tag{1}$$

We examined all the possible combinations among two kinds of heating spatial distribution, i.e. quasi-uniform[1] or localized at the loop footpoints, and two kinds of temporal distribution, i.e. impulsive or steady.

In the localized heating cases, the heating rate has a maximum at the loop footpoint, and exponentially falls off in the corona with a fixed scale-length of 10 Mm; the location

[1]Note that in the *quasi-uniform case* the chromospheric and coronal heating rates are different.

and scale-length of the energy deposition are consistent with those deduced from TRACE observations (Aschwanden et al. 2000, 2001). We also consider the possibility of an asymmetric energy deposition between the two footpoints of the loop, since real coronal loops do not appear to be symmetric. For the impulsive heating cases, we inject into the coronal segment of the loop a sequence of energy pulses, or nanoflares, with constant cadence, duration, and energy amplitude; we model each nanoflare with a Maxwellian function, such that the energy release $E(s,t)$ during a single event has a steep rise, followed by a more gradual decrease. Specifically:

$$\begin{aligned} F(s) &= \begin{cases} f \exp\left(-\frac{s-s_1}{\lambda}\right), s \geq s_1 & \text{localized heating} \\ 1 & \text{quasi-uniform heating} \end{cases} \\ G(t) &= \begin{cases} E_I \frac{1}{2\tau^3} t^2 \exp\left(-\frac{t}{\tau}\right) & \text{impulsive heating} \\ E_S & \text{steady heating} \end{cases} \end{aligned} \tag{2}$$

where $f = 0.75$ or 1.0 measures the constant ratio of the localized heating at the right footpoint to that at the left one, s_1 is the initial position of the top of the chromosphere at each footpoint, $\lambda = 10$ Mm is the scale-length of the heating distribution, E_I gives the volumetric heating per nanoflare event in the impulsive case, τ is a characteristic parameter related to the duration of the energy pulses (here always equal to 12.5 s), and E_S is the constant heating rate in the steady case. Table 1 lists the values of the parameters adopted in the simulations performed for this study.

We chose the value of E_I so that

$$\int_V dV \int_0^{t_c} E(s,t)\, dt = E_P \ \ [\text{erg}]\,, \tag{3}$$

where V is the volume of the coronal section of the loop, t_c is the cadence time between two consecutive nanoflares, and E_P is the amount of energy supplied by each pulse. For the steady heating cases, the value of E_S was adjusted so that the total energy deposited into the loop in a time interval t_c was equal to E_P, as listed in Table 1. In this case E_S is equal

Table 1: Parameters of the simulations

Run	λ	t_c	E_P[a]	E_{max}[b]	$<E>$[c]	Class
#	(Mm)	(s)	(10^{24} erg)	(erg cm^{-3} s^{-1})	(10^{21} erg s^{-1})	
1	Quasi-uniform	Steady	1	5×10^{-4}	4	Steady
2	Quasi-uniform	250	1	2×10^{-3}	4	Steady
3	Quasi-uniform	500	1	2×10^{-3}	2	Dynamic
4	Quasi-uniform	1000	1	2×10^{-3}	1	Dynamic
5	Quasi-uniform	2000	1	2×10^{-3}	0.5	Dynamic
6	10	Steady	1	4×10^{-3}	4	Condensation
7	10	250	0.125	2.75×10^{-3}	0.5	Condensation
8	10	250	0.5	1.1×10^{-2}	2	Condensation
9	10	250	1	2.2×10^{-2}	4	Condensation
10	10	250	2	4.4×10^{-2}	8	Steady
11	10	250	4	8.8×10^{-2}	16	Steady
12	10	500	0.25	5.5×10^{-3}	0.5	Dynamic
13	10	500	1	2.2×10^{-2}	2	Dynamic
14	10	500	2	4.4×10^{-2}	4	Dynamic
15	10	1000	1	2.2×10^{-2}	1	Dynamic
16	10	1000	4	8.8×10^{-2}	4	Dynamic
17	10	2000	1	2.2×10^{-2}	0.5	Dynamic
18	10	2000	8	1.76×10^{-1}	4	Dynamic

[a]Total energy per pulse, or, in the steady cases, total energy deposited into the loop in a time interval equal to $t_c = 250$ s.

[b]Maximum heating rate per unit volume.

[c]Average amount of energy supplied to the loop per unit time.

to E_{max}, as reported in Table 1.

The value of the time interval between the pulses, i.e. the cadence t_c, was fixed taking into account the characteristic radiative cooling time of the loop, $\tau_{\rm cool}$. For a loop with a semilength $L = 40$ Mm and an apex temperature $T_{\rm apex} = 2$ MK, it results $\tau_{\rm cool} \approx 1000$ s, according to, e.g., Serio et al. (1991). Here we report results obtained with t_c ranging from 250 s $\approx \tau_{\rm cool}/4$ to 2000 s $\approx 2\,\tau_{\rm cool}$.

We also considered different values for E_P, in order to change the amount of energy supplied to the loop by the sequence of heating pulses and investigate the related effects on the plasma hydrodynamics.

3. Results and discussion

3.1. Plasma dynamics

Figure 1 shows the initial part of the temporal evolution of the plasma temperature, density, and velocity averaged over a relevant portion (3/4) of the loop coronal segment (see, e.g., Patsourakos & Klimchuk 2005) in some representative cases.

In the impulsive quasi-uniform heating case with $E_P = 10^{24}$ erg and $t_c = 250$ s (run 2), the loop model simply settles into a new quasi-static equilibrium state, characterized by nearly constant temperature, density and velocity, apart from small oscillations, lower then 10%, due to the sequence of energy pulses. Note that the average values of these parameters behave as the corresponding ones obtained for the steady quasi-uniform heating case (run 1). After the start of the additional heating, the temperature of the loop immediately reaches a value of about 2.3 MK; then, in the next hour, it decreases and stabilizes around a value slightly lower than 2 MK. The density monotonically increases from 1.4×10^8 cm^{-3} to $\sim 9.0 \times 10^8$ cm^{-3}, while the plasma velocity, after a first highly dynamic phase caused by the

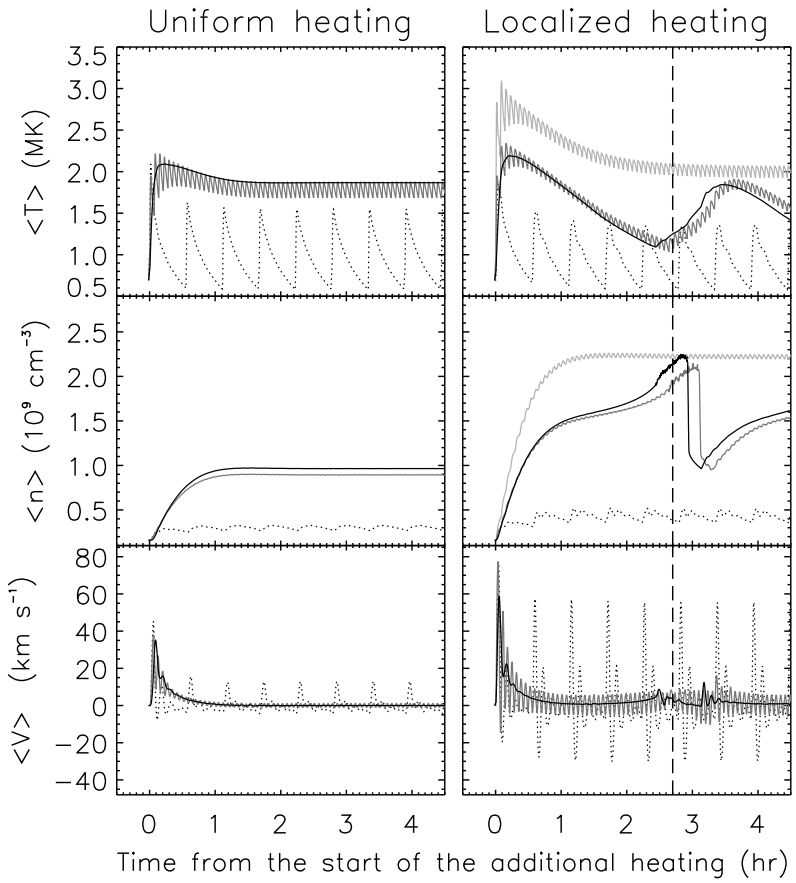

Fig. 1.— Initial part of the temporal evolution of the model temperature (top panels), density (middle panels), and velocity (bottom panels), averaged over the upper 3/4 of the loop coronal segment, for run 1, 2, and 5 (left panels; black, heavy gray and dotted lines, respectively), and run 6, 9, 10, and 17 (right panels; black, heavy gray, light gray, and dotted lines, respectively). The velocity is almost identical in runs 9 and 10 and therefore only the run 9 velocity is reported in the bottom-right panel. The vertical dashed lines in the right panels approximatively correspond to the maximum of the condensation phase for run 9, whose snapshot is given in Fig. 2.

abrupt increase of the heating rate and characterized by upflow velocities up to 40 km s^{-1}, approaches very low values of some km s^{-1}. The time-averaged plasma temperature and density for this loop model are consistent with the hydrostatic scaling laws defined by Rosner et al. (1978).

Conversely, asymmetric heating localized near the loop footpoints, both steady (run 6) and impulsive with $t_c = 250$ s (run 9), causes a more dynamic evolution for similar values of the heating parameters, with long-term fluctuations of temperature and density (after an initial steep increase) due to cycles of plasma condensation formation, motion along the loop, and falling onto the nearest and less heated footpoint (note that the first cycle only is reported in Fig. 1).

The phenomenon of plasma condensation formation is well known and extensively described in the literature (e.g., Antiochos et al. 1999, 2000; Karpen et al. 2001, 2006; Karpen & Antiochos 2008; Klimchuk et al. 2009; Müller et al. 2003, 2004; Testa et al. 2005). Recently, it has also been observed in coronal non-flaring loops (e.g., O'Shea et al. 2007). It is the effect of a thermal instability occurring near the top of the loop, where the energy supply is not sufficient to balance the radiative losses induced by the increase of the plasma density owing to the strong chromospheric evaporation. This eventually leads to a catastrophic cooling, down to chromospheric temperatures, of the material located close to the loop apex and, consequently, to the formation of a region of low-temperature and high-density plasma. This is clearly visible in Fig. 2, which shows the instantaneous plasma temperature and density profiles along the loop (run 9) at a stage of its evolution characterized by the presence of a condensation. The blob of cool and dense plasma subsequently starts moving slowly toward the less heated footpoint, because of the differences in pressure induced by the asymmetric energy release in the two legs of the loop, and finally drains onto the chromosphere. The depleted loop then reheats quickly and a new

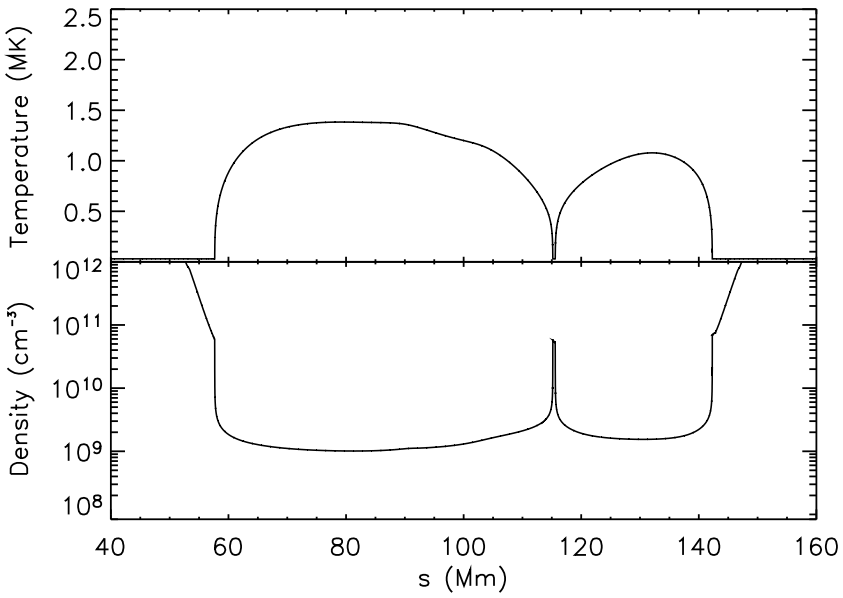

Fig. 2.— Instantaneous profiles of the loop model temperature (upper panel) and density (lower panel) vs. the curvilinear coordinates for run 9, at 2.7 hours after the start of the additional heating, marked with a vertical line in Fig. 1. The chromospheric segments have been truncated to highlight the coronal portion of the loop.

cycle of chromospheric evaporation, plasma condensation and draining takes place. In the present model the first catastrophic cooling phase approximatively begins 2.5 hours after the start of the additional heating and lasts for about one hour; its total duration slightly depends on whether the energy deposition is impulsive or steady, in the latter case being nearly 20 minutes shorter. The periodicity of the described cycle is about three hours.

The temporal evolution of run 7 and 8 (with $E_P < 10^{24}$ erg, not shown in Fig. 1) is very similar to that of run 9, with, however, lower temperatures, densities, and velocities, but again with the onset of a dynamic cycle of plasma condensation formation.

Therefore, the impulsive heating cases, both quasi-uniform (run 2) and localized (run 7, 8, and 9), do not exhibit appreciable differences with respect to the corresponding steady cases (run 1 and 6, respectively). This is expected when the cadence of nanoflares is very rapid compared to the loop plasma cooling time (see, e.g., Walsh et al. 1997; Testa et al. 2005; Klimchuk 2006). In our cases a cadence time equal to $\tau_{\rm cool}/4$ already gives a nearly steady heating situation. On the other hand, it appears evident that the localization of the heating near the loop footpoints plays a fundamental role in the plasma condensation formation when the energy deposition is steady or impulsive with a cadence time well below the loop cooling time. These results, obtained for a ratio of the heating damping-length (λ) to the loop semilength equal to 1/4, are in agreement with those of other works modeling footpoint-heated loops in similar conditions (e.g., Müller et al. 2003, 2004; Testa et al. 2005).

Run 5 and 17 illustrate both quasi-uniform and localized heating cases in which the cadence time is longer than the loop plasma cooling time ($t_c > \tau_{\rm cool}$). In this cases (dotted-line curves in Fig. 1) the temperature in the upper part of the loop coronal segment shows pronounced oscillations since there is enough time between pulses for the plasma to cool down and drain downward to the chromospheric region (as confirmed by the downward

velocities of the plasma noticed in between the pulses). Density has small variations, but velocity shows strongly damped oscillations with a rather high peak at the beginning of each energy pulse. No condensation forms in this case, because the intermittent heating prevents the accumulation of plasma at the loop top, and thus the thermal instability. A similar behavior is also obtained when $t_c \simeq \tau_{\rm cool}$ (run 4, 15, and 16) or equal to $\tau_{\rm cool}/2$ (run 3, 12, 13, and 14).

Note, however, that although the heating localization and a high frequency pulse cadence are necessary to yield a catastrophic cooling phase during the loop evolution, they are not always sufficient. The crucial point is the balance between the energy supplied to the loop top by the sequence of heating pulses and the radiative losses of the plasma accumulated therein. In fact, by sufficiently increasing the amount of energy supplied by each pulse, even without changing the other parameters of the heating regime, such a balance can be achieved, thus preventing the thermal instability and the consequent plasma condensation formation. This is the case of run 10 (see left panels in Fig. 1) and run 11.

As far as the quasi-uniform loop simulations (runs 1–5) are concerned, it is also worth noting that increasing t_c between runs 2–5 corresponds to a decrease by a factor of 8 in the total average energy $<E>$ put into the corona per second, because E_P is held fixed. Since no condensation forms, the average temperature and density are essentially controlled by the mean energy dissipated per unit time, as in the steady case (see also Sect. 3.2.2).

Although we expect that fixing $<E>$ while changing E_P would not change the overall outcome shown in Fig. 1 (left panels), it would show that in a time-averaged sense the impulsive heating gives the same average temperature and density as steady heating.

Figure 3 reports the average loop density and temperature during the evolution of some representative loops together with the hydrostatic scaling law relationship. We note that all the examined loops exhibit densities significantly smaller than those predicted

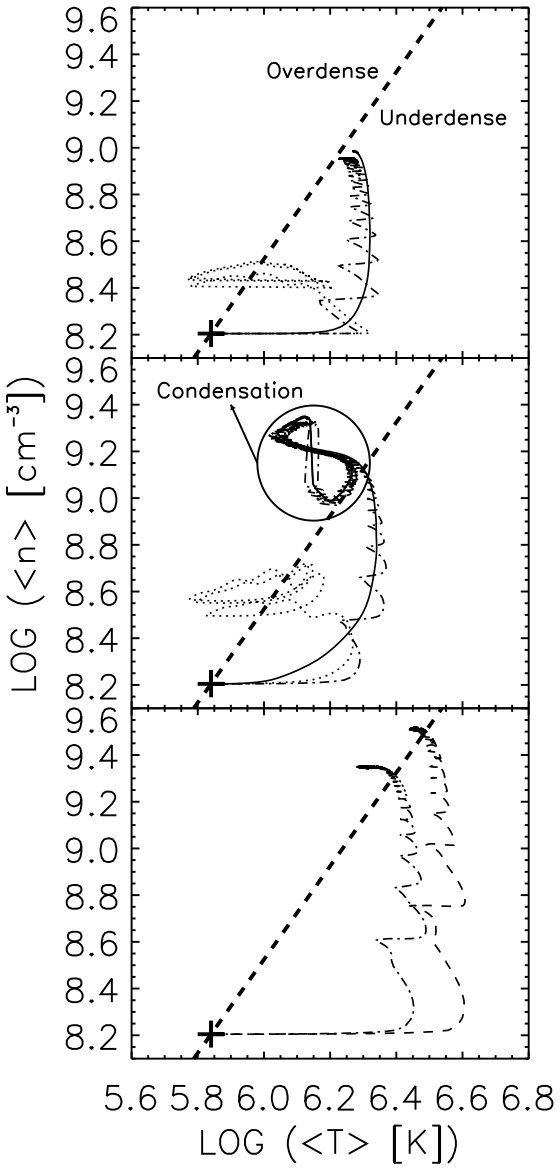

Fig. 3.— Evolution of the average loop density and temperature for runs 1, 2, and 5 (top panel; solid, dash-dotted, and dotted line, respectively), run 6, 9, and 17 (middle panel; solid, dash-dotted, and dotted line, respectively), and run 10 and 11 (bottom panel; dash-dotted and dashed line, respectively). The hydrostatic scaling law (heavy dashed line, see Rosner et al. 1978) is also reported, gauged according to the initial static equilibrium (indicated by the cross). In the middle panel, the evolution characterized by condensation formation cycles occurs within the encircled region labeled "condensation".

by the scaling laws in the initial phase of their evolution (for about one hour), in both steady-state and impulsive cases. Even if the onset of the heating produces an increase in the loop temperature and a large conductive heat flux at the coronal base of the loops, driving the upward expansion known as chromospheric evaporation (Antiochos & Sturrock 1978), there is a time lag in the corresponding increase of the coronal density, so that the loops appear to be hot and underdense.

The subsequent evolution of the loop depends on the characteristics of the plasma heating.

In the quasi-uniform cases (top panel in Fig. 3), when the heating is steady (run 1) or impulsive with a cadence time well below the loop cooling time (run 2), the loop evolves toward a new state almost consistent with the hydrostatic scaling laws (only slightly underdense). When t_c is comparable to or longer than the loop cooling time (e.g. run 5) the loops begin to move along nearly cyclic sequences, spanning from hot, underdense conditions to cool, overdense ones. Note, however, that the range of density values (in dex) is significantly smaller than that covered in temperature. Moreover, the loops appear significantly overdense only at temperatures well below 1 MK.

In the localized heating cases (middle panel in Fig. 3), cadence times comparable to or longer than the loop cooling time (e.g. run 17) give rise to a loop evolution in general agreement with that found in the quasi-uniform cases with similar cadence, although the plots reproducing the sequences exhibit some significant differences, particularly at the higher temperatures. The hydrodynamic behavior is very similar to that described by Spadaro et al. (2003), who considered localized transient heating on timescales comparable to the loop cooling time. Note that no condensation forms near the loop apex in these cases. When the localized heating is steady (run 6) or impulsive with $t_c < \tau_{\rm cool}$ (e.g. run 9), the evolution is considerably different: as the temperature decreases, the plasma

continues to evaporate and the density continues to rise, overshooting by a factor of ~ 5 the equilibrium values predicted for static loops with the same coronal temperatures, until a plasma condensation forms near the loop apex. The fall of material on to the less heated loop footpoint causes an abrupt decrease of the average density, although the loop remains slightly overdense and subsequently a new cycle of condensation formation and evolution starts. Hence these heating conditions can give rise to warm ($T \sim$ 1–2 MK), overdense loops with lifetimes of some hours, such as those observed by TRACE and SOHO.

The bottom panel in Fig. 3 shows that increasing the amount of energy supplied by each pulse, even without changing the other characteristics of the heating regime (e.g. runs 10 and 11), causes the loops to evolve toward a hot ($T \geq$ 2–3 MK), quasi-static, slightly overdense state, where they settle after a balance between the energy supplied to the loop top and the radiative losses therein is achieved. Note that run 11 might apply to the case of the hot ($\simeq$ 3 MK) loops seen by the *Yohkoh* Soft X-ray Telescope, without a corresponding warm counterpart ($\simeq$ 1 MK) observed by TRACE (see, e.g., Nitta 2000; Klimchuk 2006). If these loops are impulsively heated, then the nanoflares must occur frequently enough that the plasma does not have time to cool to TRACE temperatures.

3.2. Differential Emission Measure

Comparison of our modeling with observations is done using the differential emission measure, DEM(T) (e.g., Craig & Brown 1976), which effectively describes the plasma distribution in temperature.

We simulated the multi-strand loop DEM by averaging instantaneous DEMs calculated at $n = 300$ different times, randomly selected throughout the simulation. Although each simulation represents the evolution of a single magnetic strand, we assume that the states

of the model at n randomly selected times can be used to describe the behavior of n independent strands observed at the same time, thus giving a single simulated snapshot of a multi-stranded loop (see, e.g., Patsourakos & Klimchuk 2005). The theoretical single strand DEM is computed following Peter et al. (2006).

In what follows, the observed quiet Sun (QS) and active region (AR) DEMs are adopted from Lanzafame et al. (2005) (SOHO-CDS observations) and Lanzafame et al. (2002) (SERTS-89 observations), respectively.

3.2.1. Initial conditions and hydrostatic models

In Fig. 4 we plot the DEM corresponding to: i) the initial steady equilibrium conditions adopted in our simulations ($T_{\rm apex} \simeq 0.75$ MK, see Sect. 2); ii) the case of a spatially uniform and temporally constant background heating with $E_{\rm base} = 5 \times 10^{-4}$ erg cm^{-3} s^{-1} producing a steady loop with an apex temperature of about 2 MK at the end of the relaxation phase described in Sect. 2; iii) the quasi-uniform, steady case with $< E >= 4 \times 10^{21}$ erg s^{-1} (run 1). For comparison, the analytical DEMs computed according to the hydrostatic equilibrium laws (Rosner et al. 1978) are also shown. The divergence of the analytical results close to the top of the loop comes from the DEM formula, which is written in terms of the inverse of a temperature gradient that vanishes at the loop maximum temperature. The figure shows that our quasi-uniform, steady simulation for a multi-strand reproduces quite closely the steady equilibrium single loop structure obtained at the end of the relaxation phase with a spatially uniform and temporally constant background heating of the same level. Apex temperatures and DEM minima at the end of the relaxation phase and in the quasi-uniform, steady simulations are essentially the same as those calculated using the Rosner et al. (1978) relationships.

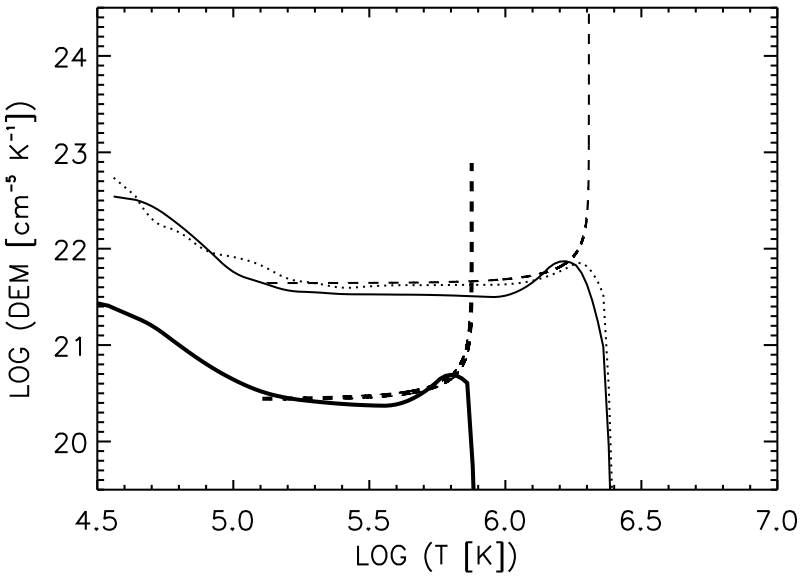

Fig. 4.— Differential emission measure (DEM) for: the initial steady equilibrium conditions adopted in our simulations with $T_{\rm apex} \simeq 0.75$ MK (thick solid line); the case of a spatially uniform and temporally constant background heating producing a steady loop with an apex temperature of $\simeq 2$ MK at the end of the relaxation phase (dotted line); the quasi-uniform, steady case with $< E >= 4 \times 10^{21}$ erg s^{-1} (run 1, thin solid line). For comparison, the analytical DEMs according to the hydrostatic scaling laws (see Eq. C4 in Rosner et al. 1978) are also shown (heavy- and light-dashed lines, respectively).

3.2.2. Quasi-uniform impulsive cases

DEMs obtained from our quasi-uniform impulsive simulations are shown in Fig. 5. Since no condensation forms, the DEM is controlled essentially by the mean energy dissipated per unit time. The runs reported in Fig. 5 have fixed $E_P = 10^{24}$ erg, and therefore the shorter t_c, the higher $< E >$. The $< E >$ values chosen in Fig. 5 correspond to cases in which the models reproduce either the observed AR DEM around $\log T = 5.5$ (and the QS DEM peak at $\log T \approx 6$), or the AR DEM temperature peak at $\log T \approx 6.3$, plus a couple of cases with energies in between. Also shown in Fig. 5 a simulation with a single pulse with $E_P = 10^{24}$ erg, which reproduces very closely the conditions explored by Klimchuk et al. (2008). From the comparison with the observed DEMs, we see that these models are unable to reproduce both the TR and coronal DEM, neither for the QS nor for the AR.

The quasi-uniform impulsive model with the highest mean energy dissipated per unit time (run 2, $t_c = 250$ s, $< E >= 4 \times 10^{21}$ erg s^{-1}) is compared with the steady-uniform model with the same mean dissipated energy rate (run 1), confirming that there is no appreciable difference between the two.

Note also that by increasing t_c well above $\tau_{\rm cool}$ (e.g. run 5 with $t_c = 2000$ s), we obtain a DEM structure very similar to that presented by Klimchuk et al. (2008). A close comparison with their simulations has been made by calculating the DEM for a single pulse and spatially uniform heating. The resulting DEM, also shown in Fig. 5, is almost identical, above $\log T = 5.5$, to those in Fig. 2 of Klimchuk et al. (2008).

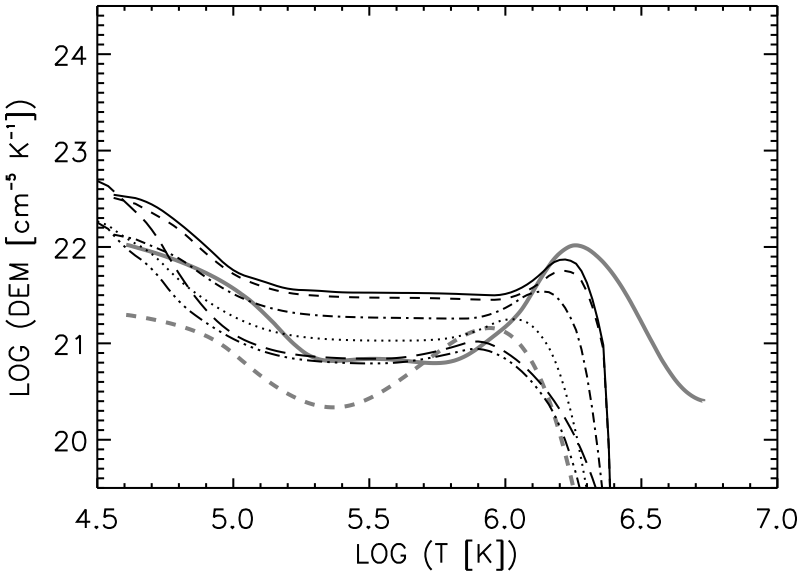

Fig. 5.— DEM from quasi-uniform impulsive simulations: run 2 (dashed line); run 3 (dash-dotted line); run 4 (dotted line); run 5 (dash-triple-dotted line). Comparison is done with QS (gray thick dashed line), AR (gray thick solid line), the quasi-uniform steady case (run 1, solid line), and a single pulse simulation (long-dashed line).

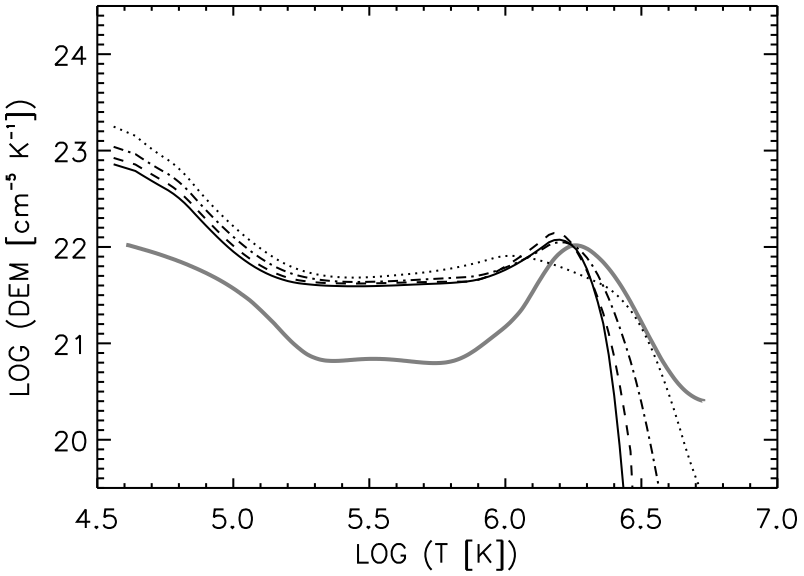

Fig. 6.— DEM for impulsive localized models with different combinations of t_c and E_P giving the same mean energy dissipated per unit time $< E >= 4 \times 10^{21}$ erg s^{-1}: run 9 (solid line); run 14 (dashed line); run 16 (dash-dotted line); run 18 (dotted line). Comparison is made with the AR DEM (gray thick solid line).

3.2.3. Localized impulsive models

In Fig. 6 we consider DEMs obtained for impulsive localized models with different combinations of t_c and E_P giving the same mean energy rate. Choosing $< E >= 4 \times 10^{21}$ erg s^{-1}, we obtain a DEM peak similar to that observed in the AR.

The mean dissipated energy determines the temperature at which the DEM is at its maximum ($T_{\rm peak}$). Increasing t_c up to $t_c \approx \tau_{\rm cool}$ causes an increase in the DEM above $T_{\rm peak}$ and a little change in the DEM slope below $T_{\rm peak}$. Increasing further t_c ($t_c > \tau_{\rm cool}$), causes a further increase in the DEM in the high temperature range (above $\log T \approx 6.5$ in the cases shown in Fig. 6) and the disappearance of the coronal DEM peak.

The differences between the cases in which condensation occurs (e.g. run 9) or does not occur (e.g. run 14) are too small to be appreciated in practice. Also, the localized steady model DEM (run 6) is almost identical to that of the localized impulsive model with the same $< E >$ and $t_c = 250$ s $< \tau_{\rm cool}$. Condensation does not produce appreciable differences in the DEM because the bulk of the plasma maintains a temperature above ~ 1 MK throughout the evolution (compare with Figs. 3 and 1). The sensitivity to t_c, on the other hand, derives from the fact that, when t_c increases well above $\tau_{\rm cool}$, condensation does not occur anymore and the bulk of the plasma has a temperature oscillating over a rather large range. In our simulations, such oscillation produces a smearing of the DEM around ~ 1 MK and eventually leads to the disappearing of the DEM peak.

Also in this case, the simulations are unable to reproduce the whole observed DEM structure. By appropriately selecting t_c and E_P, it is possible to reproduce the DEM in the high temperature range or around the minimum DEM, but it is not possible to reproduce the DEM in both ranges with a single (t_c, E_P) pair. We conclude, therefore, that the assumption of multi-strand structures subject to localized impulsive heating is not sufficient to explain the well known discrepancies with observations, which must be due to physical

processes not included in our simulation. The recent suggestion put forward by Judge (2008) of cross-field diffusion of neutral atoms from cool threads extending into the corona may help in solving problems like this. Spicular absorption of some of the plasma emission below 1 MK, as suggested by Klimchuk et al. (2008) and De Pontieu et al. (2009), might also contribute to explain the discrepancies with the observed DEM structure.

Nevertheless, we suggest that, despite such discrepancies, the systematic behavior of the simulated DEM with t_c would maintain its validity even if the models are not sufficiently detailed, and would help in discriminating at least among very different conditions. In fact, despite the small sensitivity of the DEM to variations in t_c, when this increases well above $\tau_{\rm cool}$, the coronal DEM peak tends to disappear. Such changes in the DEM shape can be reliably verified by comparison with observations, since they are well above the expected uncertainties in the DEM reconstruction. The very existence of the coronal DEM peak, therefore, is an indication of the existence of heating pulse cadence time shorter than $\tau_{\rm cool}$.

Finally, in Fig. 7 we show the simulations with $< E >= 5 \times 10^{20}$ erg s^{-1} (runs 7, 12, and 17) compared with the observed QS DEM. The dependence on t_c described above for the AR DEM is maintained at such lower energy, which corresponds to a DEM peak close to the observed QS one. The DEM peak decreases at increasing t_c, tending to disappear for $t_c > \tau_{\rm cool}$. The DEM at temperatures above $T_{\rm peak}$ increases with increasing t_c.

Comparing the simulated DEM's peaks with AR and QS observations (Figs. 6 and 7), the pronounced peak in the observed AR DEM may indicate a predominance of $t_c < \tau_{\rm cool}$ conditions. On the contrary, the less pronounced peak in the observed QS DEM may indicate that $t_c > \tau_{\rm cool}$ conditions dominate in that regime. Although the shape of the observed DEM may be affected by the smoothing imposed by the regularization technique used to reconstruct the DEM from the observed spectral line intensities, the differences implied by the models are higher than the uncertainties in the DEM reconstruction due to

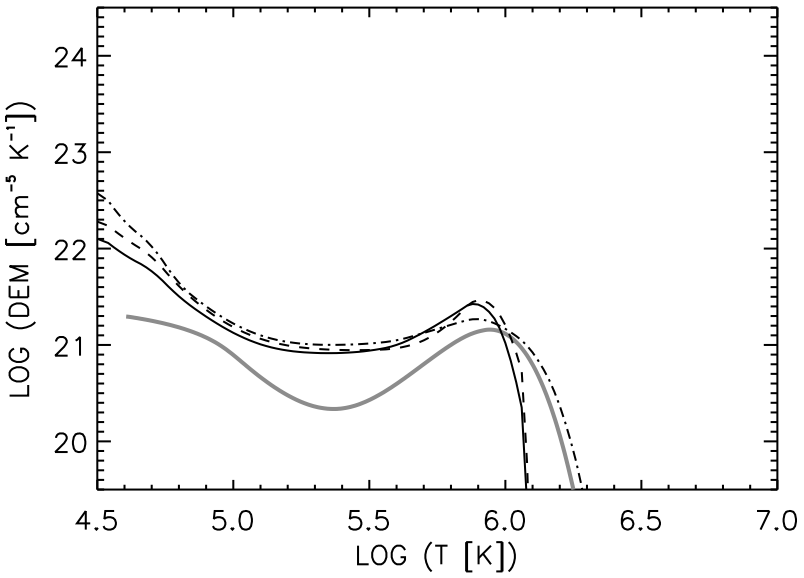

Fig. 7.— DEM for simulations with $< E >= 5 \times 10^{20}$ erg s^{-1} (run 7, solid line; run 12, dashed line; run 17, dash-dotted line) compared with the QS DEM (gray thick solid line).

regularization smoothing and intensity ratios of spectral lines formed around and above the DEM peak could be useful to discriminate among the high- and low-cadence regimes.

It is also worth noting that, despite a close fit to the observed DEM is outside the scope of this work and only a general comparison is made, models that reproduce more closely the AR DEM have a coronal electron pressure $\log P_{\rm e} \sim 15.3$ ($P_{\rm e}$ in units $\rm cm^{-3}\,K$) remarkably close to the value deducted by Lanzafame et al. (2002) using line-ratio diagnostics ($\log P_{\rm e} \sim 15.8$). In the QS case, models that reproduce more closely the observed DEM have $\log P_{\rm e} \sim 14.0$ in the coronal part, in close agreement with the Lanzafame et al. (2005) estimate ($\log P_{\rm e} \sim 13.7$ – 14.0).

4. Conclusions

We have carried out hydrodynamic simulations of multi-stranded coronal loops with a code capable of resolving the transition region sections and following their evolution in order to outline signatures of the heating regimes in the observed DEM.

Quasi-uniform or localized impulsive heating with a cadence time $\simeq 1/4$ of the plasma cooling time can produce a plasma evolution which is essentially indistinguishable from the corresponding steady cases.

Plasma condensation occurs on a limited range of heating parameters. Energy localization is necessary to yield a catastrophic cooling phase during the loop evolution, but it is not always sufficient. The crucial point is the balance between the energy supplied to the loop top and the radiative losses therein. Thus, the variation of the energy deposition parameters (such as the pulse cadence, the pulse energy, or the heating damping-length) with respect to the global characteristics of the model (the radiative cooling time or the loop length) could, in some cases, prevent the occurrence of a dynamic cycle of plasma

condensation formation even in the presence of a localized heating. This may happen, for instance, by increasing the heating rate at the loop footpoints or the ratio of the heating damping-length to the loop length, or considering nanoflare cadence times comparable to or longer than the characteristic radiative cooling time.

The DEM is found insensitive to the presence of condensation because the sequence of catastrophic cooling, draining toward the loop footpoint, reheating and evaporation does not effectively redistribute the plasma over temperature and the global distribution remains very close to the corresponding steady configuration. On the contrary, pulses with cadence longer than the plasma cooling time produce temperature oscillations in the bulk of the plasma which effectively smear the coronal DEM structure. The effects are observable since the coronal DEM peak tends to disappear when the pulse cadence is about 2 times the plasma cooling time. The pronounced DEM peak observed in active regions would indicate a predominance of conditions in which the cadence time is shorter or of the order of the plasma cooling time, whilst the structure of the quiet Sun DEM suggests a cadence time longer than the plasma cooling time.

The warm overdense and hot underdense loops observed by TRACE, SOHO (Aschwanden et al. 1999, 2001; Winebarger et al. 2003; Patsourakos et al. 2004) and *Yohkoh* (Porter & Klimchuk 1995) could be explained by the dynamic evolution of the plasma. In particular, a localized heating producing plasma condensation cycles can give rise to warm ($T \simeq 2$ MK), overdense loops with lifetimes of some hours, such as those observed by TRACE and SOHO. Moreover, increasing the amount of energy supplied by each pulse at the loop footpoints prevents the plasma condensation formation and causes the loops to settle in a hot ($T \simeq 2$–3 MK), quasi-static, slightly overdense state, which can reproduce the case of hot loops seen by *Yohkoh* SXT, without a corresponding warm counterpart observed by TRACE (e.g., Nitta 2000).

Nevertheless, our simulations are unable to reproduce both the transition region and the coronal DEM structure with a unique set of parameters, which suggest that some additional physical processes, like that proposed by Judge (2008) or by Klimchuk et al. (2008) and De Pontieu et al. (2009), must be taking place in the transition region.

DS acknowledges useful discussions with the members of the ISSI team "The role of the Spectroscopy and Imaging Data in Understanding Coronal Heating" (team Parenti).

This work was supported in part by the Agenzia Spaziale Italiana (contract I/015/07/0 and agreement ASI/INAF I/023/09/0). Financial support by the European Commission through the SOLAIRE Network (MTRN-CT-2006-035484) is also gratefully acknowledged.

REFERENCES

Antiochos, S. K., MacNeice, P. J., Spicer, D. S., & Klimchuk, J. A. 1999, ApJ, 512, 985

Antiochos, S. K., MacNeice, P. J., & Spicer, D. S. 2000, ApJ, 536, 494

Antiochos, S. K., & Sturrock, P A. 1978,ApJ, 220, 1137

Aschwanden, M. J., Newmark, J. S., Delaboudinière, J.-P., Neupart, W. M., Klimchuk, J. A., Gary, G. A. et al. 1999, ApJ, 515, 842

Aschwanden, M. J., Nightingale, R. W., & Alexander, D. 2000, ApJ, 541, 1059

Aschwanden, M., Schrijver, C. J., & Alexander, D. 2001, ApJ, 550, 1036

Cargill, P. J. 1994, ApJ, 422, 381

Cargill, P. J. & Klimchuk, J. A. 2004, ApJ, 605, 911

Craig, I. J. D. & Brown, J. C. 1976, A&A, 49, 239

De Pontieu, B., Hansteen, V. H., McIntosh, S. W., & Patsourakos, S. ApJ, 702, 1016.

Judge, P. 2008, ApJ, 683, L87

Karpen, J. T., Antiochos, S. K., Hohensee, M., Klimchuk, J. A., & MacNeice, P. J. 2001, ApJ, 553, L85

Karpen, J. T., Antiochos, S. K., & Klimchuk, J. A. 2006, ApJ, 637, 531

Karpen, J. T. & Antiochos, S. K. 2008, ApJ, 676, 658

Klimchuk, J. A. 2006, Sol. Phys., 234, 41

Klimchuk, J. A. & Cargill, P. J. 2001, ApJ, 553, 440

Klimchuk, J. A., Karpen, J. T., & Antiochos, S. K. 2009, ApJ, submitted

Klimchuk, J. A., Patsourakos, S., & Cargill, P. J. 2008, ApJ, 682, 1351

Lanzafame, A. C., Brooks, D. H., Lang, J., Summers, H. P., Thomas, R. J., & Thompson, A. M. 2002, A&A, 384, 242

Lanzafame, A. C., Brooks, D. H., & Lang, J. 2005, A&A, 432, 1063

MacNeice, P. J., Olson, K. M., Mobarry, C., de Fainchtein, R., & Packer, C. 2000, Comput. Phys. Commun., 126, 330

Müller, D. A. N., Hansteen, V. H., & Peter, H. 2003, A&A, 411, 605

Müller, D. A. N., Peter, & H., Hansteen, V. H. 2004, A&A, 424, 289

Nitta, N. 2000, Sol. Phys., 195, 123

O'Shea, E., Banerjee, D., & Doyle, J. G. 2007, A&A, 475, L25

Parker, E. N. 1983, ApJ, 264, 642

Parker, E. N. 1988, ApJ, 330, 474

Patsourakos, S., Klimchuk, J. A., & MacNeice, P. J. 2004, ApJ, 603, 322

Patsourakos, S. & Klimchuk, J. A. 2005, ApJ, 628, 1023

Peter, H., Gudiksen, B. V., & Nordlund, A. 2006, ApJ, 638, 1086

Porter, L. J. & Klimchuk, J. A. 1995, ApJ, 454, 499

Reale, F., Nigro, G., Malara, F., Peres, G., & Veltri, P. 2005, ApJ, 633, 489

Rosner, R., Tucker, W. H., & Vaiana, G. S. 1978, ApJ, 220, 643

A&A 488, 303–310 (2008)
DOI: 10.1051/0004-6361:200809713

Astronomy & Astrophysics

Physical parameters along the boundaries of a mid-latitude streamer and in its adjacent regions

R. Susino[1], R. Ventura[2], D. Spadaro[2], A. Vourlidas[3], and E. Landi[3]

[1] Dipartimento di Fisica e Astronomia – Sezione Astrofisica, Università di Catania, via S. Sofia 78, 95123 Catania, Italy
e-mail: sur@oact.inaf.it
[2] INAF-Osservatorio Astrofisico di Catania, via S. Sofia 78, 95123 Catania, Italy
e-mail: [rve;dspadaro]@oact.inaf.it
[3] Naval Research Laboratory, 4555 Overlook Avenue, SW, Washington, DC 20375-5320, USA
e-mail: [vourlidas;landi]@nrl.navy.mil

Received 4 March 2008 / Accepted 28 May 2008

ABSTRACT

Context. Coronal streamers appear to be strictly associated with the generation of the slow solar wind, even if a firm identification of the sources of the particle flux within these structures is still an unresolved issue.
Aims. The purpose of this work is to contribute to a better knowledge of the physical characteristics of streamers and of their surroundings in a wide range of heliocentric distances and at both high radial and latitudinal resolutions.
Methods. The analysis is based on spectral observations of a narrow, mid-latitude streamer performed with UVCS/SOHO during one week in May 2004: H I Lyα and O VI resonance doublet line intensities and profiles were obtained at different heliocentric distances and latitudes. In addition, white-light polarized brightness images were taken in the same days of observation, through the LASCO/SOHO C2 coronagraph.
Results. The radial variations in electron density and temperature, H I and O VI kinetic temperatures, and outflow velocities were derived from the observed line intensities, profiles, and O VI line intensity ratios between 1.6 and 5.0 $R_\odot$, in two regions, 2–3 arcmin wide, located along the boundaries and in a narrow strip (5–10 arcmin) outside the streamer structure. Significantly high kinetic temperatures and outflow velocities were found in the out-of-streamer region above 3.0 $R_\odot$ for the O VI ions and, for the first time, H I atoms, compared to those obtained along the streamer boundaries. Moreover, the O VI kinetic temperatures and velocities turn out much higher than the H I ones at any heliocentric distance in all the observed regions. A higher anisotropy is also noticed for the O VI kinetic temperature in the region flanking the streamer.
Conclusions. The slow coronal wind is found to flow with significantly different speeds and kinetic temperatures along the boundaries of the streamer and in the out-of-streamer regions at all heights, above 3.0–3.5 $R_\odot$. This fact, consistent with previous studies, indicates that two components of slow wind probably form in the observed regions: one originates just above the streamer cusp and flows with velocities a little higher than 100 km s^{-1}, while the other flows along the open magnetic field lines flanking the streamer with velocities slightly lower than the slow wind asymptotic heliospheric value of ~400 km s^{-1}, around 5.0 $R_\odot$.

Key words. Sun: corona – Sun: solar wind – Sun: UV radiation

1. Introduction

Recent observations of the extended solar corona, carried out with the Ultra-Violet Coronagraph Spectrometer (UVCS, Kohl et al. 1995) on board the SOlar and Heliospheric Observatory (SOHO, Domingo et al. 1995), have significantly contributed to the study of the physical properties of coronal structures at different heights and latitudes and to identifying the sources of fast and slow solar winds. In particular, spectroscopic analysis of ultraviolet line emission in coronal streamers has revealed that they are strictly involved in the generation of the slow-speed component of the solar wind (e.g., Kohl et al. 1997; Raymond et al. 1997).

Streamers are bright, large, and long-lived magnetic structures visible both in white and UV light. They appear to be shaped like pointed helmets or a wide fan of radial rays and extend into the interplanetary medium. During solar maximum they ubiquitously fill the solar corona, while during minimum they are located around the solar equator, forming the so-called streamer belt.

Even though many recent works made it evident that a link exists between streamers and the slow solar wind (see, e.g., Noci et al. 1997; Habbal et al. 1997; Woo & Martin 1997; Wang et al. 1998; Uzzo et al. 2003), it is not yet clear from which regions within these structures the particle flux originates. Outflow (e.g., Habbal et al. 1997; Strachan et al. 2002; Uzzo et al. 2006, 2007) and abundance (e.g., Raymond et al. 1997; Antonucci et al. 2006; Uzzo et al. 2007) measurements have shown that potential sources of the slow solar wind might be the streamer regions where a transition from closed to open magnetic field lines exists, i.e. the legs and stalk structures. Nevertheless, at present, a real identification of the slow wind acceleration regions is still an open question.

This work is based on the spectral data collected by UVCS/SOHO during one week in May 2004, already described in Spadaro et al. (2007, hereafter Paper I) and pertaining to a narrow, mid-latitude quiescent streamer observed during the declining phase of the solar activity cycle 23.

While only the results of the analysis concerning the central region of the streamer were presented and discussed in Paper I,

here we focus on characterizing the physical conditions of the plasma located across the boundaries of the streamer and in its surroundings, with a special emphasis on comparing different regions of the structure. As in Paper I, owing to the changing shape and aspect of the streamer along the line of sight over the observation week as a consequence of the solar rotation, the results obtained can be considered as an average representation of the physical status of the plasma inside and immediately outside streamer structures. To deduce the radial variations in the physical plasma parameters, such as the electron density and temperature, the kinetic temperature, and outflow velocity of the emitting ions in these regions, we adopted the same analysis methods as in Paper I. The purpose of the present work is to contribute to better knowledge of the characteristics of streamers and of their surroundings, which appear to be crucial for firmly identifying the sources of the slow solar wind in the framework of the ongoing campaign devoted to the study of the physical properties of these coronal structures (see, e.g., Uzzo et al. 2006, 2007).

2. Observations and data analysis

The spectral data described in Paper I and used in the present work were collected during special observations carried out by UVCS/SOHO in 2004 from May 17 to May 23 (see Table 1 of Paper I). The measurements refer to a narrow, mid-latitude quiescent streamer structure located above the southwest limb of the Sun and consist of radial and latitudinal scans of the extended corona from 1.6 to 5.0 $R_\odot$ in the 215°–240° range of position angle (PA, measured counterclockwise from solar north pole direction); intensities and profiles of both H I Lyα and O VI resonance doublet lines were collected during the observations (see Sect. 2 of Paper I for more details). The Lyα data were acquired only during a radial scan started on May 22 and completed on May 23, 2004.

In addition, LASCO (Large Angle Spectroscopic COronagraph, Brueckner et al. 1995) pB images, whose inversion provided electron density maps of the region observed in UV, were taken day by day from May 17 to May 22. On May 18 and 19, moreover, intensities and profiles of the O VI resonance doublet lines were also measured by the spectrometer SUMER (Solar Ultraviolet Measurements of Emitted Radiation, Wilhelm et al. 1995) in two adjacent regions on the solar disc close to the southwest limb, just below the observed streamer. These chromospheric spectral data were used to calculate the proper stray-light contribution coming from the solar disc to the O VI line profiles observed in corona (see below).

Standard wavelength and radiometric calibration, flat-field correction, image distortion, stray-light contribution removal, subtraction of the background, and instrumental broadening correction were all applied to both the H I Lyα and O VI doublet line profiles, as described in Sect. 2 of Paper I. The contribution from the interplanetary scattered Lyα line contained in the observed Lyα profile was also removed. Then the spectra were extracted and single Gaussian fits to the line profiles were obtained to determine their intensity and $1/e$ half width.

To localize the streamer borders, we adopted the $1/e$ intensity criterion described, for instance, in Abbo & Antonucci (2002), for each exposure and spectral line examined. For the northern boundary, however, this was possible only for exposures collected from May 21 to May 23 (i.e., in the 2.5–5.0 $R_\odot$ range of heliocentric distance), because in the previous days a wide, faint structure was present in the northward region of the streamer, precluding an accurate identification of the border (see Fig. 2 of Paper I). We then extracted the spectra

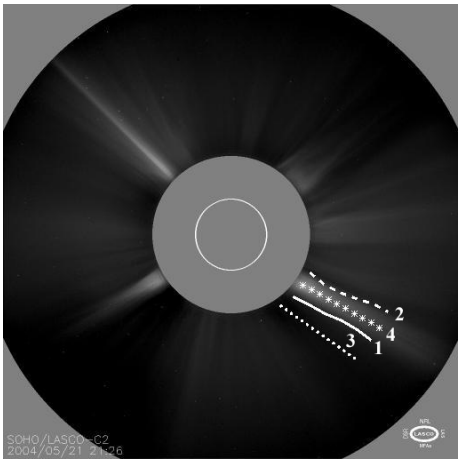

Fig. 1. LASCO C2 white-light image taken on May 21, 2004. The lines mark the positions of the southern (solid line, label 1) and northern (dashed line, label 2) boundaries of the streamer structure and its central region (asterisks, label 4), as deduced from the radial scans performed in that day. The region between the solid and the dotted lines corresponds to the observed out-of-streamer region (label 3).

relevant to two narrow strips centered on the northern and the southern boundaries of the streamer, respectively, and approximately 2–3 arcmin wide for both the H I Lyα and O VI exposures, and a strip, approximately 5–10 arcmin wide, adjacent to the southern border of the structure.

Figure 1 shows a LASCO C2 white-light image of the extended solar corona, obtained on May 21, 2004. The positions of the center of the streamer structure and of its borders, derived as described above, are superimposed on the image. It is also marked the position of the out-of-streamer region adjacent to the southern border of the observed streamer.

To derive the radial profiles of the electron density and temperature, the kinetic temperature, and outflow velocity of the emitting ions along the streamer boundaries and in the considered adjacent region, we made use of the same spectral synthesis code as was adopted in Paper I and iteratively reproduced the observed H I Lyα and O VI spectral emission as closely as possible. As in Paper I, we assumed that the bulk of the coronal emission from the considered region is confined within ±0.2–0.3 $R_\odot$ from the plane of the sky.

The average disc profiles adopted to synthesize the radiatively excited component of the spectral lines expected from the extended corona are those that gave the best results in the analysis of the central region of the streamer (see Sect. 3.2 of Paper I): i.e. the O VI 1032 and 1037 Å disc intensities listed in Vernazza & Reeves (1978) and the chromospheric Lyα line profile reported in Gouttebroze et al. (1978).

The atomic data, elemental abundances, and ionization balances used in the synthesis of the O VI and H I Lyα emission are those adopted in the analysis of the central region of the streamer (see Sect. 2 of Paper I and the discussion presented there).

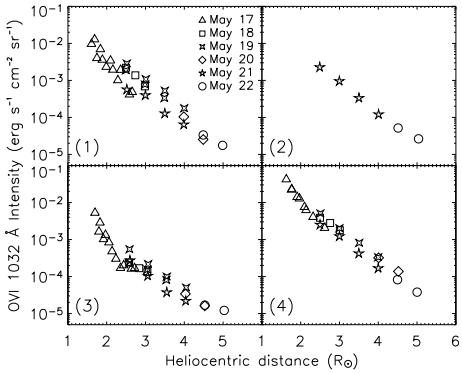

Fig. 2. O VI 1032 Å line-integrated intensities reported versus heliocentric distance along the southern (*top-left panel*) and northern (*top-right panel*) boundaries of the streamer, the out-of-streamer region (*bottom-left panel*) and the central region of the streamer (*bottom-right panel*). Different symbols refer to different observation days according to the labels reported top-left. The number in each panel denotes the corresponding observed region as represented in Fig. 1. The error bars, determined as described in the text, are not visible because they are smaller than the symbol size.

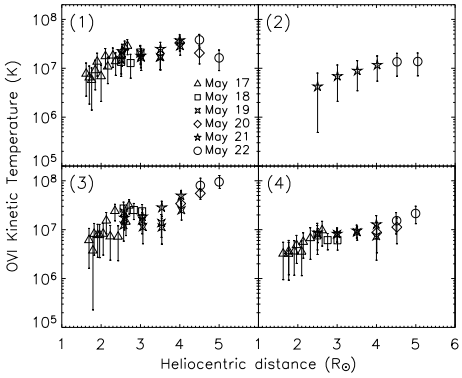

Fig. 3. Same as Fig. 2 for the O VI perpendicular (i.e. along the line of sight) kinetic temperature. See the text for a description of the error bar determination.

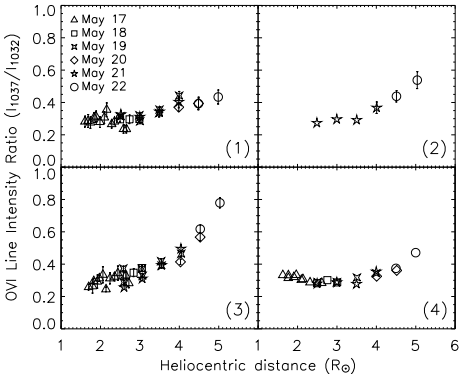

Fig. 4. Same as Fig. 2 for the O VI (1037 Å/1032 Å) line ratios. The error bars, determined as described in the text, are plotted only if greater than the symbol size.

3. Results and discussion

3.1. Behavior of the line intensities and profiles

Figure 2 shows the total intensity of the O VI 1032 Å line, as a function of heliocentric distance along the southern and the northern boundaries of the streamer, as well as in the region outside the streamer, adjacent to its southern border. The corresponding quantity observed in the central region of the streamer on the same days is also reported for comparison. The errors affecting the data points were computed as in Paper I: the corresponding $\pm\sigma$ values are plotted as error bars in the figure.

The total intensity radial profiles along the borders of the streamer (Fig. 2, top panels) fall off with height by at least two orders of magnitude in the examined heliocentric distance range. The data points referring to the northern boundary are higher than those corresponding to the southern one at any heliocentric distance (by a factor ranging from about 5 at 2.5 $R_\odot$ to about 2 at 5.0 $R_\odot$). In both cases the intensity values are systematically lower than those observed in the central region of the streamer (Fig. 2, bottom-right panel) on the same days by a factor of 3.5–4.

As for the intensity radial profile in the region adjacent to the southern border of the streamer (Fig. 2, bottom-left panel), it exhibits a decrease a little less than three orders of magnitude in the range of heliocentric distance considered. These intensity values are, on average, a factor of 3.5 lower than those measured along the streamer boundaries and by a little less than one order of magnitude lower than the corresponding data points obtained in the central region of the streamer during the same observational days. This can be ascribed to the lower density in the regions outside the streamer, as is evident in the LASCO C2 white-light images (see, e.g., Fig. 2 of Paper I).

The line-of-sight component of the O VI kinetic temperature relevant to the boundaries of the streamer (Fig. 3, top panels) shows the same increasing trend as measured along the central region of the observed structure (Fig. 3, bottom-right panel). The data points referring to the northern border are systematically lower than those corresponding to the southern one, which, in turn, are 1.5–2 times higher than in the central region at all heliocentric distances.

The O VI kinetic temperature radial profile in the region adjacent to the southern border of the streamer (Fig. 3, bottom-left panel) is characterized by a steep increase from ~4–7 MK at 1.6 $R_\odot$ to ~100 MK at 5.0 $R_\odot$. The data points almost overlap with those referring to the borders of the streamer within 3.5 $R_\odot$, while at greater heliocentric distances, the kinetic temperature in the out-of-streamer region is systematically higher. Moreover, the temperature values are several times higher than those inferred along the central region of the monitored structure on the same days, at all heights. The behavior of the O VI kinetic temperature radial profiles might suggest that the same heating mechanism acting inside the streamer is working along its boundaries, and even more efficiently in the region outside the streamer, probably due to the different magnetic configuration (open vs. closed) of this region (see, e.g. Frazin et al. 2003; Ventura et al. 2005).

The O VI intensity ratios relevant to both the southern and northern boundaries of the streamer (Fig. 4, top panels) range between 0.25 and 0.35 below 3 $R_\odot$. At greater heliocentric distances, the observed ratios increase up to 0.45–0.5. These data

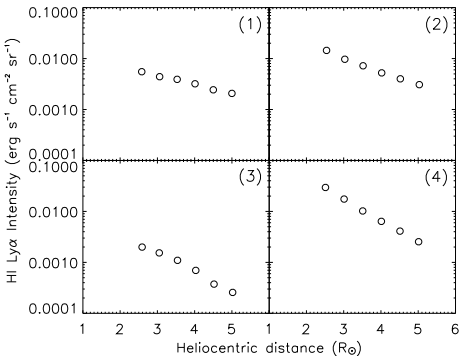

Fig. 5. H I Lyα line-integrated intensities versus heliocentric distance, as observed during the run of 2004 May 22–23 along the southern (*top-left panel*) and northern (*top-right panel*) boundaries of the streamer, the out-of-streamer region (*bottom-left panel*), and the central region of the streamer (*bottom-right panel*). The number in each panel denotes the corresponding observed region as represented in Fig. 1. The error bars, determined as described in the text, are not visible because they are smaller than the symbol size.

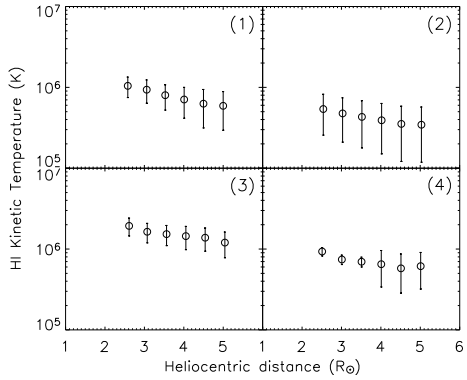

Fig. 6. Same as Fig. 5 for the H I perpendicular (i.e., along the line of sight) kinetic temperature. See the text for a description of the error bar determination.

points are spread more with respect to the O VI intensity ratio profile obtained inside the streamer (Fig. 4, bottom-right panel) on the same days, although they are characterized by very similar values at all heights.

The most evident feature of the radial profile of the O VI line intensity ratio in the region adjacent to the southern boundary of the streamer (Fig. 4, bottom-left panel) is its quickly increasing trend, from about 0.25–0.35 below 3.2 $R_\odot$ to about 0.8 at 5.0 $R_\odot$. While up to about 3.0 $R_\odot$ these intensity ratios are very similar, within the uncertainties, to those referring to both the central region and the boundaries of the streamer, at greater heliocentric distances they are higher and higher, reaching a value nearly twice that derived in the southern border of the structure at 5.0 $R_\odot$. The differences between in- and out-of-streamer ratios, increasing with height, probably reflect the progressively increasing efficiency of the Doppler dimming effect in the regions flanking the streamer, where the magnetic field lines open and the solar wind is expected to accelerate more and more with height (see, e.g., Noci et al. 1987).

Figure 5 shows the total intensity of the H I Lyα line as a function of the heliocentric distance along the two boundaries of the streamer (top panels) and in the region adjacent to the southern border (bottom-left panel). For comparison, the corresponding quantity referring to the central region of the streamer is also reported (bottom-right panel). The errors affecting the data points have been estimated as in the case of O VI lines. Due to the high rate of charge exchange between protons and neutral hydrogen in the corona up to about 10 $R_\odot$, we can use the Lyα line widths as a proxy for the velocity distribution of protons along the line of sight (e.g., Withbroe et al. 1982; Allen et al. 1998; Vásquez et al. 2003).

The Lyα intensity radial profiles along the two boundaries exhibit the same decreasing trend in the examined interval of heliocentric distances. The data points relevant to the southern boundary are lower than those referring to the northern one by little more than a factor of two at 2.5 $R_\odot$ and nearly 1.5 times at 5.0 $R_\odot$. In both cases the intensity values are in general lower than those observed along the central region of the streamer with vanishing differences at greater heights. The intensity distribution in the region outside the streamer exhibits the same decreasing trend, even if it is systematically lower, with values up to one order of magnitude less than in the borders. It is worth noting that the decrease in the Lyα intensity profiles is shallower than that of the O VI line observed on May 21 and 22 in the same range of heights, for all the regions considered here, because Lyα is resonantly scattered, while O VI 1032 Å is collisionally excited.

Figure 6 reports the line-of-sight component of the H I kinetic temperature as a function of the heliocentric distance for all the considered regions. The radial distribution of the H I kinetic temperature along the southern border of the streamer (top-left panel) exhibits a mild decrease from 1 MK to about 0.6 MK, in the 2.5–5.0 $R_\odot$ range of heights. These temperature values are slightly higher than those observed in the region inside the streamer (bottom-right panel), while the values referring to the northern border (top-right panel) are on average about a factor of two lower at any heliocentric distance; however, such differences might not be significant, due to the error bars affecting the data points.

As for the out-of-streamer region (Fig. 6, bottom-left panel), the kinetic temperatures are more than a factor of two higher than those measured along the southern boundary of the structure, although they exhibit the same decreasing trend. These properties generally agree with the hypothesis of a heating mechanism that acts more efficiently in the regions surrounding the streamer, where an open magnetic configuration is expected. However, the main feature is the opposite behavior of the kinetic temperature of the H I atoms in comparison with the O VI ions. The characteristic decreasing trend of the former was also present in the data referring to the central region of the streamer (see Sect. 3.1 of Paper I).

3.2. Derivation of the physical parameters

The radial profiles of the electron density and temperature, kinetic temperature, and outflow velocity of the emitting ions along the boundaries of the streamer and in its adjacent region were derived from the empirical data presented in the previous subsection, using the same iterative approach as described in Sect. 3.2 of Paper I. To take possible variations in the physical parameters due to a temporal evolution of the observed structure into account (caused, for instance, by the solar rotation or

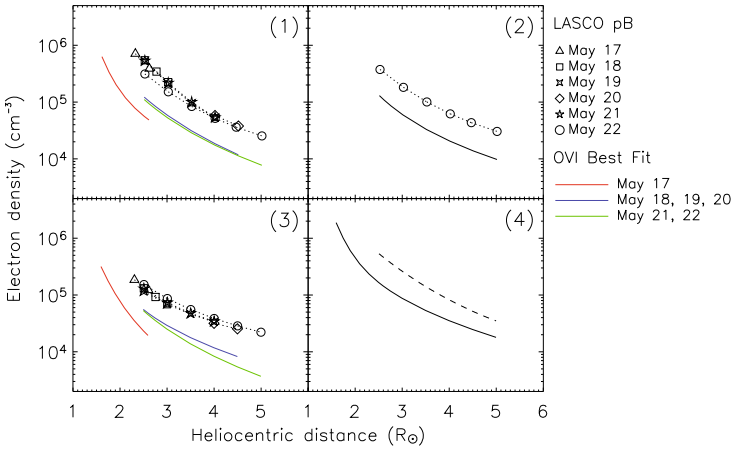

Fig. 7. Electron densities obtained from the inversion of LASCO C2 pB data (open points connected by dotted lines) and electron density radial profiles giving the best synthesis of O VI spectral data (solid color lines) derived along the southern (*top-left panel*) and northern (*top-right panel*) boundaries of the streamer, the out-of-streamer region (*bottom-left panel*) and the central region of the streamer (*bottom-right panel*). Different symbols and colors refer to different days of observation according to the legend. The number in each panel denotes the corresponding observed region as represented in Fig. 1.

changes in the global structure of the streamer), we grouped the O VI spectral data into three subsets, containing the observations collected on May 17, May 18, 19, and 20, and May 21, 22, respectively. Our choice was motivated by the line intensities relevant to May 18, 19, and 20 being systematically higher than those obtained during the other days. We then derived the plasma conditions for the three subsets separately.

Figure 7 reports the electron density radial profiles deduced from the inversion of the LASCO C2 pB data collected during the days of observation, together with those giving the best synthesis of the observed O VI emission line intensities, profiles, and intensity ratios, for both the streamer boundaries (top panels) and the out-of-streamer region (bottom-left panel). The density curves obtained in the case of the central region of the streamer (bottom-right panel, see also Paper I) are also shown for comparison purposes.

The different profiles deduced by the LASCO C2 pB data inversion during the various observation days exhibit a similar behavior, both along the boundaries and in the region adjacent to the streamer. They decrease by about one order of magnitude in the considered range of heliocentric distance. Moreover, the differences among the various curves are always within a factor of two in both cases. The density values along the boundaries of the streamer are slightly lower than those deduced from LASCO data within the central region of the structure, by a factor of 1.5 on average. The density values derived outside the streamer, conversely, are significantly lower than along the axis: by a factor of about 4 at 1.6 $R_\odot$ and about two at 5.0 $R_\odot$.

We used the electron density values relevant to May 22 to synthesize the H I Lyα line intensities and profiles, both along the streamer boundaries and in the adjacent region, getting good agreement, within the uncertainties, with the observed spectral data reported in Figs. 5 and 6 at all heights.

However, as in the case of the central region of the streamer, the density values obtained from LASCO C2 data are too high to consistently reproduce the observed O VI emission line intensities, profiles, and intensity ratios (see the detailed discussion of this issue in Paper I). The density profiles giving the best synthesis of the observed O VI spectral data are systematically lower, in general by a factor of 3.5 in the 2.5–5.0 $R_\odot$ range of heliocentric distance. This difference is larger than the estimated uncertainties in the determination of the electron density, which are below a factor of two (cf. Hayes et al. 2001; Strachan et al. 2002). For a possible explanation of this apparent discrepancy, we refer the reader to the detailed discussion reported in Paper I, considering that the observed O VI emission probably originated in a narrow structure away from the plane of the sky, contributing little brightness compared to the background corona, whereas the Lyα, and most of white-light radiation, could originate in a wider and denser region along the line of sight.

The curves obtained by matching the O VI observations and relevant to the streamer boundaries (Fig. 7, top panels) exhibit systematically lower density values than those corresponding to the central region of the streamer (Fig. 7, bottom-right panel), by about a factor of 3 in the 1.6–2.5 $R_\odot$ range of heliocentric distances (i.e., for observations collected on May 17) and by about a factor of two at greater heights. The density profile relevant to the northern boundary (Fig. 7, top-right panel) overlaps that corresponding to the southern one practically at all heliocentric distance except above 4.0 $R_\odot$, where it is slightly higher. The out-of-streamer density profiles (Fig. 7, bottom-left panel) are even lower than those relevant to the central region of the streamer by about a factor of 4–5. The profiles giving the best synthesis of O VI spectral data also show significant variations during the different observational days, while the curves relevant to May 18, 19, 20 and May 21, 22 are almost consistent. The density values fitting the observations collected on May 17 are systematically lower than those corresponding to the other days, by about a factor of 2.5 at 2.6 $R_\odot$ along the borders of the streamer and by about a factor of 3 at the same height in its adjacent region. This variability reflects the fluctuations found in the O VI emission line intensity radial profiles on the same days (see Fig. 2) and can be reasonably ascribed to both the changing shape and aspect of the streamer and surrounding regions during the observational week, although some effect of the CME which occurred on May 18 in the northward region of the examined structure cannot be ruled out.

The electron temperature (T_e) radial profiles along the borders of the streamer and in its adjacent region were derived from the corresponding density profiles by the same technique adopted in Paper I and described by Gibson et al. (1999), which works under the assumption that the coronal plasma is in radial hydrostatic equilibrium. This means that there are no significant dynamic forces and that thermal pressure is balanced by gravity. This hypothesis could be considered fairly valid for the plasma located across the boundaries of the examined streamer, since

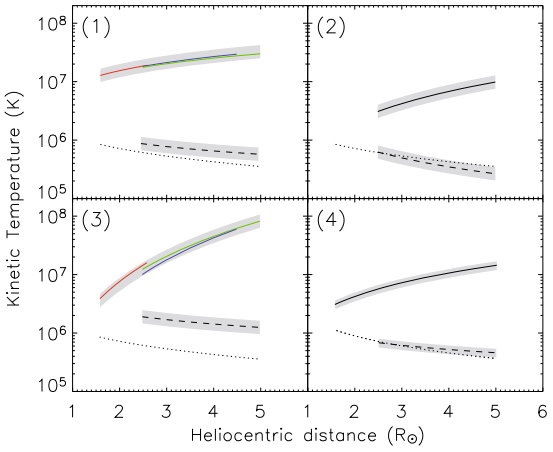

Fig. 8. Radial profiles of the O VI (solid color lines) and H I (dashed black lines) kinetic perpendicular temperature ($T_\perp$) empirically derived by iteratively reproducing as closely as possible the data reported in Figs. 3 and 6, respectively. They are shown versus heliocentric distance along the southern (*top-left panel*) and northern (*top-right panel*) boundaries of the streamer, the out-of-streamer region (*bottom-left panel*), and the central region of the streamer (*bottom-right panel*). Different colors refer to different observational days according to the legend. Also reported is the averaged radial profile of the electron temperature T_e (dotted line), determined as described in the text. The number in each panel denotes the corresponding observed region as represented in Fig. 1. The shaded bands represent the average ranges of uncertainties affecting the temperature curves.

the velocities reached by the O VI ions and the hydrogen atoms at 5.0 $R_\odot$ in these regions are about 120 km s^{-1}, so well below the thermal velocities of electrons corresponding to the resulting temperatures at all heights. In the out-of-streamer regions, however, the assumption of radial hydrostatic equilibrium still holds only at low heliocentric distances, while at greater heights the high outflow velocity of particles determined in this study cannot be considered as a minor term in the force balance (see below). In this case, therefore, the values of electron temperature deduced from the electron density, according to Gibson et al. (1999), are only a first approximation estimate.

The electron temperature profiles resulting from the different density profiles reported in Fig. 7 do not exhibit significant differences between both the streamer boundaries and the region adjacent to the southern border of the structure. Therefore we averaged the various electron temperature profiles and obtained a common curve for these three regions. This curve, reported in Fig. 8 (top and bottom-left panels), is less than 30% lower than the profile derived in the region inside the streamer (bottom-right panel, see also Paper I).

Figure 8 also shows the empirical radial profiles of the component of the kinetic temperature in the direction perpendicular to the magnetic field ($T_\perp$) deduced for O VI ions and H I atoms (protons) along the streamer boundaries and in the out-of-streamer region. The average uncertainty ranges affecting the radial profiles, reported in the figure, were derived in terms of the lowest and highest temperature values that allow a consistent reproduction of the observed line intensities, profiles, and O VI intensity ratios, within the observational uncertainties.

The O VI perpendicular kinetic temperature along the southern border of the streamer (Fig. 8, top-left panel) ranges from about 10 MK at 1.6 $R_\odot$ to about 30 MK at 5.0 $R_\odot$, with values that are systematically higher than those derived along the central region of the streamer (Fig. 8, bottom-right panel), by a factor of about 3.5 at 1.6 $R_\odot$ and about 2 at 5.0 $R_\odot$. The temperature profile along the northern boundary (Fig. 8, top-right panel), conversely, exhibits a similar increasing behavior than that obtained along the streamer axis, although it is 1.5 times lower on average. In the streamer adjacent region (Fig. 8, bottom-left panel) the temperature radial profile abruptly increases from about 3.5 MK at 1.6 $R_\odot$ to nearly 100 MK at 5.0 $R_\odot$, with values much higher (up to nearly one order of magnitude) than those obtained inside the streamer. Note that the curves relevant to different days exhibit no significant variations.

The radial profiles of the H I perpendicular kinetic temperature are all much lower (up to about two orders of magnitude) than the corresponding O VI profile. Along both the boundaries of the streamer, they show a slight decrease in the 2.5–5.0 $R_\odot$ interval of heliocentric distance and do not diverge from the corresponding curve relevant to the central region of the streamer by more than 50%. Differences of the same order of magnitude or even lower can be noticed when comparing the electron temperature profile with the H I $T_\perp$ curves along both the streamer borders. Therefore it seems reasonable that the hydrogen atoms (and then protons) in these regions are nearly in thermal equilibrium with electrons, as well as along the central region of the streamer (see Paper I). This is not the case in the region adjacent to the southern border of the structure, where the radial profile of the H I perpendicular kinetic temperature is higher than the corresponding electron temperature curve, by a factor of 3 on average. Note, also, that the H I kinetic temperature is higher outside the streamer than in its central region by the same factor.

As for the components of the O VI and H I kinetic temperatures parallel to the magnetic field lines ($T_\parallel$), not reported in Fig. 8, the best synthesis of the empirical data set relevant to the streamer borders was obtained considering slightly anisotropic conditions with $T_\parallel = T_\perp/1.3$, according to what has already been found in the analysis of the central region of the streamer (see Paper I and Frazin et al. 2003). Outside the streamer we achieved the best synthesis of the H I spectral data with the same level of anisotropy in the kinetic temperature. In the case of O VI a higher anisotropy ($T_\parallel = T_\perp/2.0$) is required for the best fit to the observations.

The empirical radial profiles of the O VI and H I outflow velocity along the boundaries of the streamer and in its adjacent region are reported in Fig. 9. They were obtained by adopting the same procedure as described in Sect. 3.2 of Paper I. The corresponding quantity along the central region of the streamer structure is also reported for comparison. The error bars of ±25 km s^{-1}, on average, affecting each point were deduced as in the case of the kinetic temperature uncertainties.

The outflow velocity values derived for both O VI ions and neutral hydrogen atoms along the southern boundary of the streamer (Fig. 9, top-left panel) are generally consistent, within the uncertainties, with those obtained for the northern one

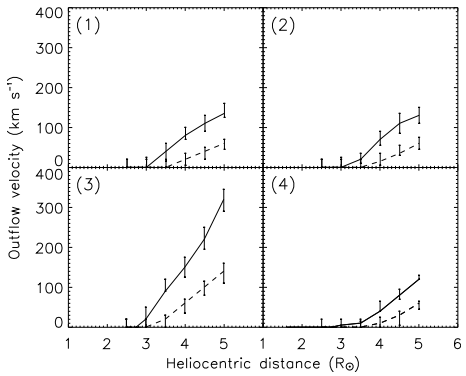

Fig. 9. Radial profiles of the O VI (solid lines) and H I (dashed lines) outflow velocity derived along the southern (*top-left panel*) and northern (*top-right panel*) boundaries of the streamer, the out-of-streamer region (*bottom-left panel*) and the central region of the streamer (*bottom-right panel*). The number in each panel denotes the corresponding observed region as represented in Fig. 1.

(Fig. 9, top-right panel). Evidence of significant deviation from static conditions only appears above 3.0 $R_\odot$ for both of them. The O VI outflow velocity along the borders of the streamer is in general greater than in the central region of the structure (Fig. 9, bottom-right panel) by about a factor of 1.5–2, reaching values around 135 km s^{-1} at 5.0 $R_\odot$. Moreover, its radial profile is steeper along the boundaries, below 4.0 $R_\odot$. No significant differences have been found for the H I outflow velocity between the radial profiles derived along the boundaries of the streamer and in its central region; moreover, the respective curves reach the same value of 60 km s^{-1} at 5.0 $R_\odot$.

The out-of-streamer scenario (see Fig. 9, bottom-left panel) is substantially different, even if static conditions still appear present below 3.0 $R_\odot$. The O VI outflow velocity profile abruptly increases above 3.0 $R_\odot$, from values around 20 km s^{-1} to 320 km s^{-1} at 5.0 $R_\odot$. This speed value is nearly 3 times higher than obtained at the same height in the central region of the streamer. The H I outflow velocity increases more gradually than does that of O VI, reaching a speed of about 150 km s^{-1} at 5.0 $R_\odot$, that is, 2.5 times higher than derived in the central region of the streamer at the same height.

It is worth noticing that the outflow velocity of coronal O VI ions at lower heights might be underestimated in this analysis: we adopted the quiet Sun O VI line disc intensities reported in Vernazza & Reeves (1978) to perform the synthesis of O VI emission in the examined regions, obtaining a very consistent agreement with the observations. However, a non-negligible O VI outflow velocity below 3.0 $R_\odot$ could result from the analysis of the observed line intensity ratio, when the possible influence of the active region sunspots (present on the solar disc during the week of observation, see Fig. 4 in Paper I) on the intensity of the radiative scattering component of the coronal O VI lines is also considered, as discussed by Morgan & Habbal (2005).

We finally note that, in all the examined regions, the O VI ions appear to flow significantly faster (2–3 times) than the H I ones. This, together with the considerably higher O VI kinetic temperatures found in the examined regions, confirms the possibility of energy deposition and plasma heating and acceleration through the absorption of Alfvén waves at ion cyclotron frequency (e.g., Li et al. 1997, 1999; Tu & Marsch 1997; Cranmer et al, 1999a, 1999b; Hu & Habbal, 1999), both along the boundaries of the streamer structure and immediately outside it.

4. Summary and conclusions

Through the analysis of the intensity and profile of the H I Lyα and O VI resonant doublet lines, we empirically determined the plasma parameters at different heliocentric distances along the boundaries and in a region adjacent to a mid-latitude streamer, observed through a week in May 2004, during the declining phase of the solar activity cycle 23.

The electron density values deduced by both the LASCO C2 pB data and O VI spectral data are lower than the corresponding ones inferred inside the streamer by a factor of 2–3 along the borders and by a factor of 3–5 in the out-of-streamer region. This behavior has already been described in the literature: in their analysis of several mid-latitude streamers observed in 1997 and 2000 (i.e., during the minimum and the maximum of solar activity), Ventura et al. (2005) found that the out-of-streamer regions are characterized by densities up to one order of magnitude lower than those relevant to the regions inside the streamers; similar results have also been obtained by Antonucci et al. (2005), who analyzed a collection of equatorial streamers at solar minimum.

The electron temperature radial profiles deduced both along the boundaries of the streamer and in its adjacent region exhibit the same decreasing trend as inferred along the central region of the structure, with only slightly lower values. These modest differences are consistent with the results of Antonucci et al. (2005), who derived a radial profile of T_e for regions adjacent to streamers and compared it to the profile obtained by Gibson et al. (1999) along the streamer's central regions. The component of the O VI kinetic temperature in the direction perpendicular to the magnetic field is characterized by a steep increase with height, both along the boundaries of the streamer and in its surroundings, reaching values considerably higher than in the central region of the streamer. A similar trend characterizes the results reported in Antonucci et al. (2005), Spadaro et al. (2005) and Ventura et al. (2005), who found significantly higher O VI temperatures in the regions adjacent to the observed streamers. However, these authors did not notice appreciable differences between the in- and out-of-streamer radial profiles of the H I kinetic temperature, whereas we found on average a factor of 3 higher temperatures outside the streamer. Conversely, Uzzo et al. (2007) found H I temperatures up to a factor of about 2 higher inside the mid-latitude streamers considered in their analysis, compared to outside, between 1.75 and 5.0 $R_\odot$. In one case only, at 5.0 $R_\odot$, they noticed a temperature value slightly lower in the central region of a streamer with respect to its surroundings.

Evidence of a non-negligible outflow velocity of O VI and H I ions appears at 3.0–3.5 $R_\odot$, both along the borders of the streamer and in the out-of-streamer region, while static plasma conditions hold at lower heights. The outflow velocity of the O VI ions significantly increases in the considered range of heliocentric distances, while the hydrogen atoms appear to accelerate more gradually.

The O VI outflow velocity behavior determined here is generally in good agreement with that inferred by Habbal et al. (1997) in the first study of the transition from fast to slow wind across a streamer using UVCS measurements. These authors reported O VI speeds of about 94 km s^{-1} at 4.5 $R_\odot$, in the central region of the examined streamers, while, at increasing distances from the streamer axis, they found the same value closer to the

Sun, namely at 3.5–4.0 $R_\odot$ and 2.5–3.0 $R_\odot$ at $PA = \pm 10°$, and $PA = \pm 20°$ from the streamer axis, respectively. This is also compatible with the latitudinal gradient in O VI wind speed occurring very close to the streamer borders in our data.

The O VI velocity derived outside the streamer, examined here at 3.5 $R_\odot$, is consistent, within the uncertainties, with the value (~115 km s^{-1}) reported by Antonucci et al. (2005) at the same height in regions lying in the immediate vicinity of streamers. However, these authors found significant velocities even below 3.0 $R_\odot$: already at 1.8 $R_\odot$, for instance, they got a value of ~90 km s^{-1}, that is comparable with those derived by Cranmer et al. (1999b) at the same height in the core of polar coronal holes during the minimum of solar activity. These differences could probably be ascribed to the fact that the out-of-streamer regions observed by Antonucci et al. (2005) are nearly 1.5 times wider than those considered in our analysis and on average 30° far from the respective streamer axis, while in our case the maximum separation is about 20°, so the out-of-streamer strips examined by Antonucci et al. (2005) could intersect wider parts of the large coronal holes located around the solar poles during activity minimum, where the acceleration of the wind could take place already at low heliocentric distances, resulting in greater outflow velocities. On the other hand, we cannot exclude that the O VI ion speed values deduced from our analysis could be underestimated below 3.0 $R_\odot$, as described at the end of Sect. 3.2.

An interesting feature is that the enhancements in the perpendicular kinetic temperature of O VI and, to a lesser extent, of H I already appear to increase at heliocentric distances below 3.0 $R_\odot$. Probably, the same mechanism responsible for the plasma heating at low heights also gradually accelerates the wind particles, which reach detectable velocities only at larger heliocentric distances. Similar differences between the kinetic and dynamical plasma responses were also detected by Spadaro et al. (2005), in their analysis of plasma parameters inside and outside mid-latitude streamers at solar minimum, and by Ventura et al. (2005), whose observed O VI line intensity ratios are in excellent agreement with those reported in this work.

The H I and O VI outflow velocities in the region adjacent to the southern border of the streamer are significantly lower (by a factor of 4–5) than those characterizing the fast wind flowing in polar coronal holes (see, e.g., Kohl et al. 1998; Cranmer et al. 1999b; Antonucci et al. 2004; Telloni et al. 2007). This clearly indicates that the plasma located immediately outside the streamer is in a regime of slow flow, even if its velocity is higher than along both the boundaries and inside the streamer above the cusp, i.e., the region where the transition between closed and open magnetic field lines takes place and the heliospheric current-sheet forms.

Hence we can conclude, in agreement with Antonucci et al. (2005), that two components of slow wind probably form in the observed regions. One is flowing along the magnetic flux tube formed by the open field lines delimiting the streamer structure, with only slightly lower O VI velocities at 5.0 $R_\odot$ than the slow wind asymptotic heliospheric value of approximately 400 km s^{-1}. The other one originates just above the streamer cusp, in our case located between 3.5 and 4.0 $R_\odot$, and flows with significantly slower speed than in the regions flanking the structure. Our investigation showed for the first time that this bi-modal behavior also occurs for the H I velocities in the examined regions. The differences between these two slow-wind components suggest that they are probably of different nature, and the particle flux observed above the streamer cusp cannot be considered simply as the merging of the wind flowing in the regions surrounding the streamer structure (see, e.g., Noci et al. 1997; Raymond et al. 1997; Antonucci et al. 2005).

Acknowledgements. The authors wish to thank Y.-K. Ko for her assistance during UVCS/SOHO observations carried out at NASA GSFC, and R. Suleiman for his help in the preliminary reduction of the UVCS raw data. They also thank the referee for providing very useful comments. This work was supported in part by the Agenzia Spaziale Italiana (contract I/035/05/0). Financial support by the European Commission through the SOLAIRE Network (MTRN-CT-2006-035484) is also gratefully acknowledged. The work of E. Landi is supported by NASA grants.

References

Abbo, L., & Antonucci, E. 2002, in SOHO 11 Symp., From Solar Minimum to Max: Half a Solar Cycle with SOHO, ed. A. Wilson (Noordiwijk: ESA), ESA-SP, 508, 477
Allen, L. A., Habbal, S. R., & Hu, Y. Q. 1998, JGR, 103, 6551
Antonucci, E., Dodero, M. A., Giordano, S., Krishnakumar, V., & Noci, G. 2004, A&A, 416, 749
Antonucci, E., Abbo, L., & Dodero, M. A. 2005, A&A, 435, 699
Antonucci, E., Abbo, L., & Telloni, D. 2006, ApJ, 643, 1239
Brueckner, G. E., Howard, R. A., Koomen, M. J., et al. 1995, Sol. Phys., 162, 357
Cranmer, S. R., Field, G. B., & Kohl, J. L. 1999a, ApJ, 518, 937
Cranmer, S. R., Kohl, J. L., Noci, G., et al. 1999b, ApJ, 511, 481
Domingo, V., Fleck, B., & Poland, A. I. 1995, Sol. Phys., 162, 1
Frazin, R. A., Cranmer, S. R., & Kohl, J. L. 2003, ApJ, 597, 1145
Gibson, S. E., Fludra, A., Bagenal, F., et al. 1999, JGR, 104, 9691
Gouttebroze, P., Lemaire, P., Vial, J. C., & Artzner, G. 1978, ApJ, 225, 655
Habbal, S. R., Woo, R., Fineschi, S. et al. 1997, ApJ, 489, L103
Hayes, A. P., Vourlidas, A., & Howard, R. A. 2001, ApJ, 548, 1081
Hu, Y. Q., & Habbal, S. R. 1999, JGR, 104, 17045
Kohl, J. L., Esser, R., Gardner, L. D., et al. 1995, Sol. Phys., 162, 313
Kohl, J. L., Noci, G., Antonucci, E., et al. 1997, Sol. Phys., 175, 613
Kohl, J. L., Noci, G., Antonucci, E., et al. 1998, ApJ, 501, L127
Morgan, H., & Habbal, S. R. 2005, ApJ, 630, L189
Noci G., Kohl, J. L., & Withbroe, G. L. 1987, ApJ, 315, 706
Noci, G., Kohl, J. L., Antonucci, E., et al. 1997, in Fifth SOHO Workshop, The Corona and Solar Wind near Minimum Activity, ed. A. Wilson (ESA-SP 404; Noordwijk: ESA), 75
Raymond, J. C., Kohl, J. L., Noci, G., et al. 1997, Sol. Phys., 175, 645
Spadaro, D., Ventura, R., Cimino, G., & Romoli, M. 2005, A&A, 429, 353
Spadaro, D., Susino, R., Ventura, R., Vourlidas, A., & Landi, E. 2007, A&A, 475, 707 (Paper I)
Strachan, L., Suleiman, R., Panasyuk, A. V., Biesecker, D. A., & Kohl, J. L. 2002, ApJ, 571, 1008
Telloni, D., Antonucci, E., & Dodero, M. A. 2007, A&A, 472, 299
Uzzo, M., Ko, Y.-K., Raymond, J. C., Wurz, P., & Ipavich, F. M. 2003, ApJ, 585, 1062
Uzzo, M., Strachan, L., Vourlidas, A., Ko, Y.-K., & Raymond, J. C. 2006, ApJ, 645, 720
Uzzo, M., Strachan, L., & Vourlidas, A. 2007, ApJ, 671, 912
Vásquez, A. M., van Ballegooijen, A. A., & Raymond, J. C. 2003, ApJ, 598, 1361
Ventura, R., Spadaro, D., Cimino, G., & Romoli, M. 2005, A&A, 430, 701
Vernazza, J. E., & Reeves, E. M. 1978, ApJS, 37, 485
Wang, A. H., Wu, S. T., Suess, S. T., Poletto, G. 1998, JGR 103, 1913
Woo, R., & Martin, J. 1997, GRL, 24, 2535
Wilhelm, K., Curdt, W., Marsch, E., et al. 1995, Sol. Phys.,162, 189
Withbroe, G. L., Kohl, J. L., Weiser, H., & Munro, R. H. 1982, Space Sci. Rev., 33, 17
Woods, T. N., Tobiska, W. K., Rottman, G. J., & Worden, J. R. 2000, JGR, 105, 27195
Zangrilli, L., Nicolosi, P., Poletto, G., et al. 1999, A&A, 342, 592

A&A 475, 707–715 (2007)
DOI: 10.1051/0004-6361:20077873

Astronomy & Astrophysics

Physical parameters of a mid-latitude streamer during the declining phase of the solar cycle

D. Spadaro[1], R. Susino[2], R. Ventura[1], A. Vourlidas[3], and E. Landi[3]

[1] INAF-Osservatorio Astrofisico di Catania, via S. Sofia 78, 95123 Catania, Italy
e-mail: [dspadaro;rventura]@oact.inaf.it
[2] Dipartimento di Fisica e Astronomia – Sezione Astrofisica, Università di Catania, via S. Sofia 78, 95123 Catania, Italy
e-mail: sur@oact.inaf.it
[3] Naval Research Laboratory, 4555 Overlook Avenue, SW, Washington, DC 20375-5320, USA
e-mail: [vourlidas;landi]@nrl.navy.mil

Received 14 May 2007 / Accepted 7 September 2007

ABSTRACT

Context. Investigating the physical properties of solar coronal streamers is important for understanding their role in the global magnetic structure of the extended solar atmosphere, as well as in the generation of the slow solar wind.
Aims. We hope to contribute as completely as possible to the ongoing SOHO instruments campaign devoted to the study of the physical characteristics of coronal streamers at various heliocentric distances.
Methods. We analyzed ultraviolet H I Lyα and O VI resonance doublet lines observed by UVCS/SOHO in a narrow, mid-latitude streamer structure along different lines of sight during a week in May 2004 and made nearly simultaneous white-light polarized brightness measurements from the LASCO/SOHO C2 coronagraph.
Results. Electron densities and temperatures, H I and O VI kinetic temperatures, and outflow velocities were derived from the line intensities and widths, as well as from the O VI line intensity ratio in the 1.6−5 $R_\odot$ range of heights, limited to the central region of the streamer. To our knowledge, the H I outflow velocities obtained in this work are the first ones determined inside a streamer structure. They are significantly lower than those of the O VI ions. This, together with the O VI kinetic temperatures that are much higher than the H I ones, suggest that the absorption of Alfvén waves at the ion cyclotron frequency might also occur inside streamers.
Conclusions. In comparison with other streamers described in the literature, the structure examined in this work generally exhibits lower electron density and neutral hydrogen kinetic temperature. Conversely, the O VI kinetic temperature and outflow velocity radial profiles are consistent with the results for the other examined streamers.

Key words. Sun: corona – Sun: solar wind – Sun: UV radiation

1. Introduction

Streamers can be described as collections of open and closed magnetic flux tubes that give rise to elongated, high-density, helmet, or fan-shaped structures extending from the Sun into interplanetary space (see, e.g., Noci et al. 1997; Kohl et al. 2006). During solar maximum, they can be found at almost every latitude, while they are located during minimum around the solar equator, forming the so-called streamer belt.

Investigating the physical properties of solar coronal streamers as completely as possible is important for understanding the role that they play both in the global magnetic structure of the extended solar atmosphere (see, e.g., Low 2001) and in the generation of the largely variable, slow-speed solar wind believed to originate within such features. Many recent works have focused on this topic (e.g., Marsch 1997; Noci et al. 1997; Raymond et al. 1997; Habbal et al. 1997; Woo & Martin 1997), but – at present – a firm identification of the slow wind-source regions inside streamers is still an unresolved issue.

Up to about a decade ago, most of the information on streamers came from visible-continuum eclipse observations, from which profiles of density vs. height have been derived at different times during the solar activity cycle. Following the launch of SOHO (SOlar and Heliospheric Observatory) satellite in 1995 (Domingo et al. 1995), new information on streamer properties has become available, in particular through the Ultraviolet Coronagraph Spectrometer (UVCS, Kohl et al. 1995), which offered the first opportunity to study the basic properties of the most intense EUV emission line profiles (e.g., the H I Lyα and O VI resonance doublet) as a function of heliocentric distance and latitude in the extended solar corona.

The ultraviolet emission lines present a rich and varied source of diagnostic information about the solar corona. The line intensity and profile for a given element depend on the electron density, the electron temperature, the density and kinetic temperature of the emitting ions, and on the outflow velocity. In the following text we report the physical parameters and their radial variations in a narrow, mid-latitude streamer structure, derived from observations carried out through a week in May 2004, during the declining phase of the solar activity cycle 23. The empirical model describing the streamer characteristics presented in this paper is based on analysis of ultraviolet spectroscopic measurements in the extended corona obtained by UVCS and of white-light polarized brightness measurements from the LASCO (Large Angle Spectroscopic COronagraph) C2 coronagraph (Brueckner et al. 1995), both aboard the SOHO satellite. The values of these parameters are compared with the properties of streamers observed by SOHO instruments during the course of the solar cycle and/or at latitudes closer to the solar equator, with the aim of contributing to the ongoing campaign devoted

Table 1. Summary of the UVCS observations.

Start date, Time (UT)	PA (°)	Heliocentric distances ($R_\odot$)
May 17, 17:30	215	1.6, 1.75, 1.90, 2.1
	225	2.3, 2.6
	240	2.6, 2.3
	235	2.1, 1.9, 1.75, 1.6
May 18, 17:45	235	2.5, 2.75, 3.0
May 19, 18:00	235	2.5, 3.0, 3.5
	240	4.0
	240	3.5, 3.0, 2.5
May 20, 14:00	235	4.0, 4.5
May 21, 19:40	235	2.5, 3.0, 3.5, 4.0
May 22, 15:30 (O VI)	235	4.5, 5.0
May 22, 21:30 (Lyα)	235	2.5, 3.0, 3.5, 4.0, 4.5, 5.0

Note. The values of PA refer to the center of the entrance slit.

to the study of the physical characteristics of coronal streamers (see, e.g., Uzzo et al. 2006).

2. Observations and data analysis

The present work is based on spectral data collected during special observations carried out by UVCS/SOHO in 2004, from May 17 at 17:30 UT to May 23 at 06:30 UT. The measurements consist of radial and latitudinal scans of the extended corona above the southwest limb of the Sun, from 1.6 to 5.0 $R_\odot$, in the 215°−240° range of position angle (PA, measured counterclockwise from solar north pole). On May 17 and 19 UVCS performed both radial and latitudinal scans, while only radial scans were carried out the other days. Details of the observation sequences are reported in Table 1. During the whole observation period, we monitored a mid-latitude quiescent streamer, located in the southwest quadrant. Note that the maximum values of the line intensities along the entrance slit correspond to PA's around 235°, at all the heights considered during the various days of observation. Only data pertaining to this region of the streamer have been analyzed in the present work.

Only intensities and profiles of the O VI resonance doublet lines were collected in the first 5 days, while the last day was devoted to acquiring intensities and profiles of both the O VI and Lyα lines, the latter through the redundant optical path of the O VI channel. The O VI data were taken with a spatial binning of 6 pixels, giving a spatial resolution of 42 arcsec (7 arcsec for each pixel) along a 40 arcmin entrance slit. The slit width was set equal to 50 μm at 1.6 $R_\odot$, and progressively increased up to 200 μm at higher heliocentric distances in order to optimize both spectral resolution and photon flux. To meet the same requirement for Lyα observations, carried out only at or above 2.5 $R_\odot$ (see Table 1), we adopted a spatial binning of 3 pixels and a slit width of 150 μm at any height. The exposure time was 200 s, in all cases, and the number of exposures was chosen for each position of the entrance slit so as to optimize the signal-to-noise ratio.

LASCO C2 pB images were also taken day by day from May 17 to May 22, 2004. The inversion of such pB data (see, e.g., Hayes et al. 2001) provided daily electron density maps relevant to the portion of extended corona observed in UV, in the 2.25 to 6 $R_\odot$ range of heliocentric distance. We also determined the electron density (N_e) below 2.25 $R_\odot$ by adopting the method described by Parenti et al. (2000), based on the dependence on N_e of the ratio of the radiative and collisional components of the O VI 1032 Å line. This technique works under the condition of a nearly static plasma, as is the case of the examined streamer below 2.25 $R_\odot$, so that the Doppler dimming effect on the radiatively excited component of the O VI lines can be considered negligible. Values of the ratio $(I_{rad}/I_{col})_{1032}$ were derived from our UVCS data through the simple relationships between the intensities of the collisionally and radiatively excited components of the O VI 1032 Å and 1037 Å lines, i.e., $I_{col}(1032)/I_{col}(1037) = 2$ and $I_{rad}(1032)/I_{rad}(1037) = 4$ (see, also, Noci et al. 1987). Considering that the total intensity of each doublet line is given by $I = I_{rad} + I_{col}$, we obtain:

$$(I_{rad}/I_{col})_{1032} = \frac{2(I_{1032} - 2I_{1037})}{4I_{1037} - I_{1032}}.$$

On May 18 and 19, in addition, the intensity and profile of the O VI resonance doublet lines on the solar disc were obtained by the spectrometer SUMER (Solar Ultraviolet Measurements of Emitted Radiation, Wilhelm et al. 1995), which observed two adjacent regions close to the southwest limb just below the observed streamer, approximately 5 arcmin wide in the y direction. The SUMER data consist of high-resolution spectra centered on the O VI doublet at 1032 Å and 1037 Å, observed using the $0.3'' \times 120''$ slit. These spectra were taken at four different locations ($Y = -533''$, $-433''$, $-333''$, $-233''$) along the northsouth direction and at the same position along the eastwest direction ($X = 750''$). At each position along the northsouth direction, the observations were repeated 11 times with an exposure time of 30 s. SUMER data were then decompressed, corrected from the flat-field image and geometrical distortions, and calibrated by using the standard software available as part of the SolarSoft package. SUMER data were averaged along the slit to increase the signal to noise ratio; the results for the same position along the northsouth direction were then averaged together, resulting in one single spectrum for each position along the northsouth direction. Gaussian line profiles were fitted from the resulting spectra, paying close attention to background removal.

These chromospheric spectral data were used to calculate the proper stray-light contribution coming from the solar disc to the O VI lines observed in corona and, together with disc intensities provided by other authors, to synthesize the radiatively excited component of the coronal lines expected from the streamer model (see below). Moreover, the disc intensity of the O VI 1032 Å line was used in Eq. (8) of Parenti et al. (2000) to determine the electron density at heliocentric distances lower than 2.25 $R_\odot$. As for the Lyα line, we adopted the average chomospheric profile reported by Gouttebroze et al. (1978), which agrees, within the uncertainties, with the full-disc Lyα intensities measured by the spectrometer SOLSTICE (SOLar STellar Irradiance Comparison Experiment) on the UARS satellite (see Woods et al. 2000) during the week of our observations.

Figure 1 shows a composite view of the extended solar corona and of the chromosphere, obtained on May 17, 2004. The Hα image of the solar disc, taken at the INAF-Catania Astrophysical Observatory, illustrates the conditions of the chromosphere on the first day of observation. Some instantaneous positions of the UVCS slit, superimposed on the LASCO C2 white-light image, are also reported. The presence of a group of filaments lying in a wide area under the streamer is evident. Some active regions are also present on the equatorial belt, but they do not seem to be connected to the streamer morphology. This fact should be kept in mind when interpreting the results.

Figure 2 reports the sequence of white-light LASCO C2 images, taken from May 18 to 22, 2004, together with some of the instaneous positions of the UVCS slit during the radial scans.

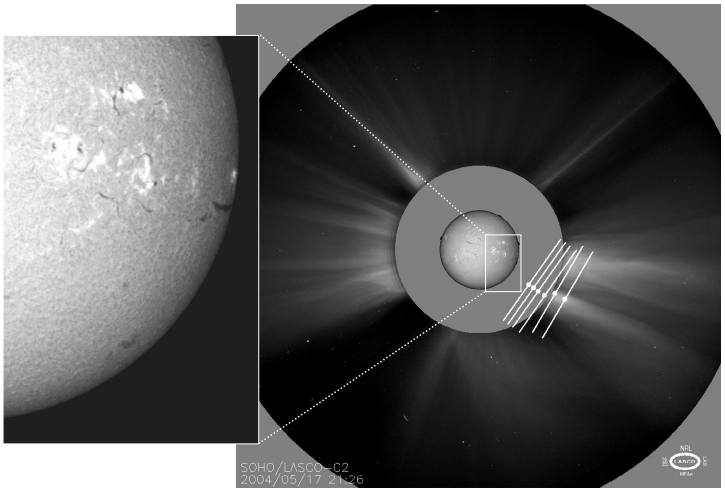

Fig. 1. Composite image obtained by combining the Hα image of the solar disc, taken at the INAF-Catania Astrophysical Observatory on May 17, 2004, and the LASCO C2 white-light image of the extended solar corona taken on the same day. Some instantaneous positions of the O VI channel entrance slit of UVCS (white segments) during the radial scan are shown superimposed on the LASCO image. The white dots mark the positions along the slit closest to the solar limb, to which the heliocentric distances and PA reported in Table 1 refer. A closer view of the disc region near the limb below the observed streamer, extracted from the Hα image, is also shown on the left.

It proves the different aspects of the streamer observed along the line of sight during the observation period as a consequence of the solar rotation. It is worth noting that on May 18, at 12:06 UT, a faint CME left the Sun along the PA = 256° direction, as reported in the SOHO LASCO CME catalog. However, it is classified as "very poor", and its influence on the streamer structure appears negligible, as can be deduced from LASCO C2 data and related movies.

The UVCS Data Analysis and processing Software (DAS, originally developed by C. Benna, A. van Ballegoijen, J. Raymond and S. Giordano) was used for flat-field correction, wavelength and radiometric calibration, removal of image distortion, and spectra extraction (Gardner et al. 1996; Kohl et al. 1997). Panasyuk's package (available from the Harvard-Smithsonian Center for Astrophysics website: `cfa-www.harvard.edu/uvcs`) was used to remove the stray light contribution to both the H I Lyα and O VI doublet lines, as well as the contribution from the interplanetary scattered Lyα line contained in the observed Lyα profile. Subtraction of the background and instrumental broadening correction were also performed before single Gaussian fits to the line profiles were obtained, in order to determine their intensity and $1/e$ half width.

The values of the electron density, electron temperature, kinetic temperature, and outflow velocity of the emitting ions at different heliocentric distances in the streamer region centered around PA = 235° (hereafter indicated as central region of streamer) have been deduced by iteratively reproducing the above set of observational results as closely as possible, by means of a spectral synthesis code developed by Ventura & Spadaro (1999). The code calculates both the radiatively and collisionally excited components of coronal lines from an adjustable model of the considered solar structure and average disc profiles of the chromospheric and inner corona exciting lines. It also includes the progressive depletion of the radiative components with increasing plasma outflow speed, known as the Doppler dimming effect (see, e.g., Kohl et al. 2006). We adopted an improved version of the code that takes possible anisotropies in the kinetic temperatures of the emitting ions into account, considering a bi-Maxwellian velocity distribution. As in Strachan et al. (2002) and Uzzo et al. (2006), we assumed that the bulk of the coronal emission from the streamer is contained within $\pm 0.2-0.3\,R_\odot$ from the plane of the sky.

Atomic data, elemental abundances, and ionization balances are those reported in Ventura & Spadaro (1999) and in papers quoted there. Note that the ionization balances for H I and O VI ions adopted in the present work were obtained with the assumption of ionization equilibrium. This appears to be fairly valid for low-velocity regimes, as can be expected to occur in streamer structures (cf., Spadaro & Ventura 1994a,b). Moreover, the O VI line intensity ratio, suitable for obtaining information on the outflow speed inside a coronal structure, does not depend on the ionization balance of the ionic species (see Noci et al. 1987).

3. Results and discussion

3.1. UVCS line intensities and profiles

Figure 3 reports the total intensity of the O VI 1032 Å line as a function of heliocentric distance along the central region of the streamer. The errors affecting the data points were computed as the standard deviation ($\pm 1\sigma$) of the Poisson photon-counting statistics. The O VI 1032 Å intensity distribution, obtained as a combination of radial scans carried out in a time interval of 6 days (see Table 1), falls off with height by about three orders of magnitude. It is evident that the points relevant to May 18, 19, and 20 are systematically higher than those corresponding to the other observing days. The projection along the line of sight of different components of the streamer region, dragged westward by the solar rotation, might clearly account for the increase in the O VI emission, although we cannot rule out some effect of the CME that occurred on May 18. Even if this event did not appear to affect the streamer structure significantly, the possible presence of coronal material, left along the line of sight after the CME occurrence, could enhance the O VI 1032 Å emission for a while.

Figure 4 reports the O VI line intensity ratio I(1037 Å)/I(1032 Å) as a function of the heliocentric distance along the central region of the streamer. This ratio was obtained by combining the values referring to the various observation days. The uncertainties in the line ratios have been deduced from the

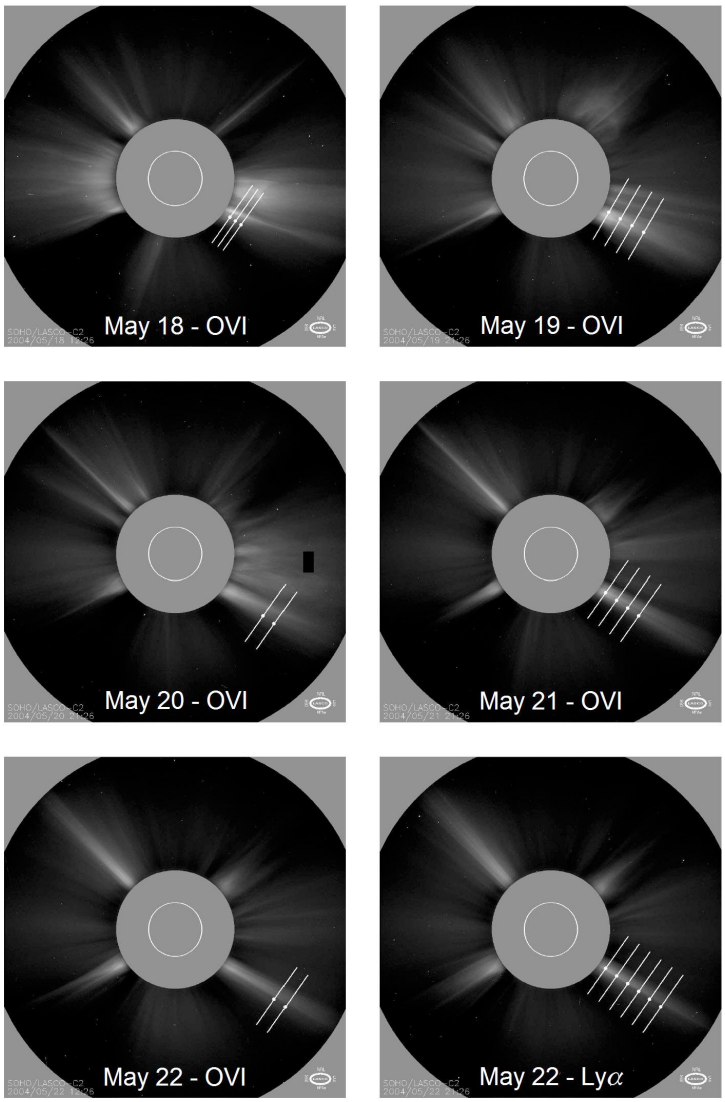

Fig. 2. LASCO C2 white-light images taken from May 18 to May 22, 2004, during the O VI scans and the Lyα scan, as indicated in each panel. Some instantaneous UVCS slit positions are also reported, superimposed on the LASCO images.

statistical uncertainties in the relevant line intensities. Within 4.0 $R_\odot$, the O VI intensity ratio is below or equal to 0.35, with a flat minimum $\simeq$0.28 between 2.5 and 3.5 $R_\odot$. At greater heliocentric distances, the O VI intensity ratio increases up to nearly 0.5, revealing a corresponding increase in the radial outflow velocity from values around 20 km s^{-1} to about 100 km s^{-1} (Noci et al. 1987; Noci & Gavryuseva 2007). It is worth noting that the values of the line ratio referring to the days characterized by the enhancement in the O VI line intensities (see Fig. 3) are in excellent agreement with the behavior of the ratios derived from the data collected in the other days. Since CME eruptions typically involve flows of material with velocities well above 100 km s^{-1}, implying line ratios significantly higher than 0.5 (Noci et al. 1987), this result appears to confirm the idea of a negligible influence of the observed CME on the dynamical structure of the monitored streamer.

Figure 5 shows the radial profile along the central region of the streamer of the O VI line-of-sight component of the kinetic temperature (hence, perpendicular to the solar radial direction, which is approximately the direction of the magnetic field), deduced from the $1/e$ half widths of the O VI 1032 Å spectral line. The uncertainties in the kinetic temperature have been estimated from the uncertainties affecting the line widths, through the error propagation statistical treatment (see Zangrilli et al. 1999). The corresponding σ values are plotted as error bars in Fig. 5. The most evident feature of this radial profile is its quickly increasing trend, from ~2−3 MK to ~20 MK, in the range of heliocentric

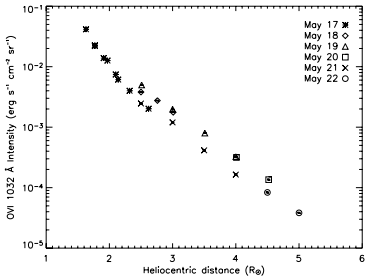

Fig. 3. O VI 1032 Å line-integrated intensities reported as a function of the heliocentric distance along the central region of the mid-latitude streamer observed from May 17 to May 22, 2004. Different symbols refer to different observation days. The error bars, determined as described in the text, are smaller than the symbol size for all the data points.

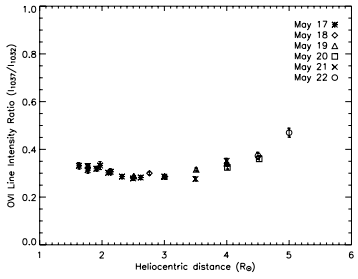

Fig. 4. As in Fig. 3, for the O VI (1037 Å/1032 Å) line intensity ratio. The error bars, determined as described in the text, are smaller than the symbol size for many of the data points.

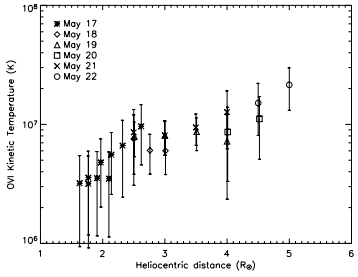

Fig. 5. As in Fig. 3, for the O VI perpendicular kinetic temperature, i.e., along the line of sight. See the text for a description of the error bar determination.

distance considered. This suggests that some kind of heating might be taking place within the streamer.

Figure 6 reports the total intensity of the H I Lyα line as a function of heliocentric distance along the central region of the streamer, as determined by the radial scan carried out in the 2.5−5.0 $R_\odot$ range, from 21:30 UT on May 22 to 6:30 UT on May 23 (see Table 1). The errors affecting the data points were computed as in the case of O VI lines. The Lyα intensity radial profile exhibits a shallower decrease than that of the O VI line observed on May 21 and 22: in the same range of heights, we notice a decrease slightly larger than one order of magnitude for the former and about two orders of magnitude for the latter.

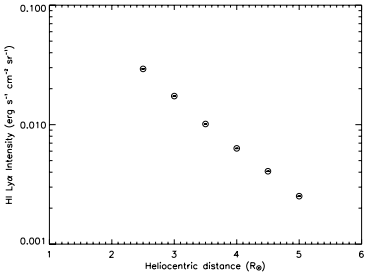

Fig. 6. Line-integrated intensities of the H I Lyα line as a function of heliocentric distance along the central region of the streamer, obtained on May 22–23, 2004. The error bars, determined as described in the text, are smaller than the symbol size for all the data points.

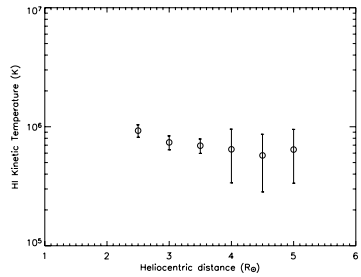

Fig. 7. As in Fig. 6, for the H I perpendicular kinetic temperature, i.e., along the line of sight. See the text for a description of the error bar determination.

Besides the possible differences due to the solar rotation, it is worth noting that, as discussed in previous papers (e.g., Ventura et al. 2005), the two lines fall off differently with height because Lyα emission is dominated by resonance scattering, proportional to the density, while the O VI line also has a collisionally excited component, which depends on density squared.

Figure 7 shows the radial profile of the H I perpendicular kinetic temperature derived as in the case of the O VI ions, together with their related uncertainties. Due to the high rate of charge exchange between protons and neutral hydrogen, we can use the Lyα line widths as a proxy for the velocity distribution of protons along the line of sight (e.g., Withbroe et al. 1982; Allen et al. 1998; Vásquez et al. 2003). The small decrease in the H I perpendicular kinetic temperature, by about a factor 1.4 in the 2.5−5.0 $R_\odot$ range, and the values always below or equal to 1 MK are the main characteristics of a behavior opposite that of the O VI ions (see Fig. 5). This different behavior has already been described in the literature (e.g., Strachan et al. 2002; Ventura et al. 2005; Uzzo et al. 2006) and hints at mechanisms that preferentially heat O VI ions more than protons.

3.2. Diagnostics of physical parameters

The above set of observational results were used as constraints to derive the plasma conditions in the monitored streamer structure. In fact, the Lyα and O VI resonance-doublet line intensities and profiles depend on the electron density, the electron temperature, the density and kinetic temperature of the emitting ions, and the outflow velocity, so that the radial profiles of these physical parameters along the central region of the streamer can be

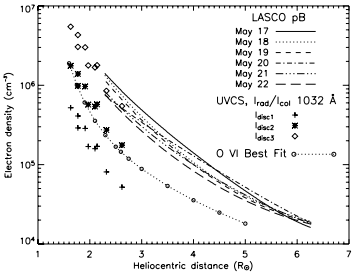

Fig. 8. Electron densities derived from the inversion of LASCO C2 pB data relevant to the different days of observation, represented as a function of heliocentric distance by different curves. Also reported are the densities obtained from UVCS line intensities below 2.6 $R_\odot$. Different symbols refer to values obtained adopting different O VI 1032 Å disc intensity inputs, namely $I_{\rm disc1}$ = 116, $I_{\rm disc2}$ = 305, $I_{\rm disc3}$ = 610 erg cm^{-2} sr^{-1} s^{-1}. Finally, the open circle-dotted line represents the electron density profile giving the best agreement between the synthesized and the observed O VI line emission.

determined after iteratively reproducing the spectroscopic data reported in the previous subsection as closely as possible by means of the synthesis code quoted in Sect. 2 (see, e.g., Ventura & Spadaro 1999).

The iterative procedure starts from an initial estimate of the above plasma parameters, deduced from the UV line intensities and profiles, as well as white-light pB data, collected during the whole observation period (see Sect. 2 and, also, cf. Kohl et al. 1997). The spectral characteristics of the emission lines synthesized by this initial model are compared with the measured spectroscopic observables. Then the plasma parameters are iteratively re-adjusted under the guidance provided by the repeated comparison of the synthetic observables with the data, until an optimal consistency with the observations is obtained (cf., e.g., Kohl et al. 2006). The agreement of the emission-line intensities, profiles, and intensity ratios synthesized from the resulting empirical model of the streamer with the spectral data reported in Figs. 3−7 appears remarkable, well within the data uncertainties, particularly in the case of the O VI line intensity ratio.

Figure 8 shows the radial profiles of the electron density along the central region of the mid-latitude streamer monitored during our week of observations, derived from the inversion of LASCO C2 pB data relevant to the different days of observation, together with the density values obtained at lower heliocentric distances from the UVCS data collected on May 17 (see Table 1), adopting the method proposed by Parenti et al. (2000).

The various density profiles obtained by the LASCO C2 pB data inversion overlap at heliocentric distances greater than 5.5 $R_\odot$, while they fan out progressively at lower heights, even if the largest differences among the various curves are always within a factor of two. This is reasonable, due to the changing shape and aspect of the streamer over the observation days. The Lyα intensities and profiles synthesized by adopting the electron density values relevant to May 22, also taking into account the Doppler dimming effect due to the outflow velocity, reproduce the spectral data reported in Figs. 6 and 7 quite well.

The electron densities computed by Eq. (8) of Parenti et al. (2000) were obtained assuming an electron temperature equal to 1.1×10^6 K (Fineschi et al. 1998) over all the 1.6−2.6 $R_\odot$ range of heliocentric distances. Different symbols refer to different values of the O VI 1032 Å disc intensity adopted in the relationship from which densities have been derived, respectively 116, 305, and 610 erg cm^{-2} sr^{-1} s^{-1}. The first intensity value corresponds to the average of the SUMER disc measurements carried out on May 18 and 19. The resulting density values are more than one order of magnitude lower than those deduced by LASCO C2 pB data at 2.3 and 2.6 $R_\odot$ and hardly compatible with an ideal extrapolation of LASCO density curves at lower heights. The second value of the O VI disc intensity is the quiet-Sun contribution listed in Vernazza & Reeves (1978), while the third one was adopted in order to get densities satisfactorily matching those derived from LASCO C2 pB data. An intensity value about five times higher than measured by SUMER could be considered questionable at first glance. However, the lack of simultaneous measurements of disc intensities is a source of uncertainty whose influence is hardly quantifiable, as we do not really know how large a variability we can expect in the O VI 1032 Å disc intensities. Moreover, SUMER observations are relevant to a limited quiet region close to the limb below the observed streamer, while a significantly higher contribution to the disc radiation could also come from some of the active regions near the equator visible in the Hα image of May 17 (see Fig. 1), and still present on the following days (see, for instance, Morgan & Habbal 2005).

Also reported in Fig. 8 is the electron density profile giving the best synthesis of the observed O VI emission line intensities, profiles, and intensity ratios. These density values are systematically lower than those derived by LASCO C2 pB data inversion, in some cases even a factor of five lower. At low heliocentric distances, they are in good agreement with the densities obtained by the method of Parenti et al. (2000), with an O VI disc intensity input equal to the quiet-Sun value reported by Vernazza & Reeves (1978).

The observed values of the resonance-doublet line ratio I(1037 Å)/I(1032 Å) strongly indicate that the densities derived from LASCO data are too high to explain the streamer emission in the O VI lines. They result in synthetic O VI intensity ratios systematically close to 0.5, corresponding to resonance-doublet line emission dominated by the collisionally excited components (Noci et al. 1987), even at heliocentric distances below 4.0 $R_\odot$, where the observed curve exhibits lower values and the characteristic shape discussed by Noci et al. (1987) and Noci & Gavryuseva (2007). This holds even if we adopt the highest O VI disc intensities listed above in the calculation of the radiatively excited components of the coronal lines. On the other hand, the use of the lowest density values reported in Fig. 8 results in synthetic O VI intensity ratios almost close to 0.25, the ratio of the radiatively excited components of the lines (Noci et al. 1987), already below 2.5 $R_\odot$, whatever the O VI disc intensities adopted among those listed above. Hence we also consider these densities unsuitable for explaining the observed O VI emission.

The striking differences among the electron density values obtained by the LASCO C2 pB data inversion, which nicely reproduce H I Lyα observations, and those adopted to fit the O VI resonance doublet data (see Fig. 8) deserve a further and more thorough analysis, also considering that such differences are indeed larger than the estimated density uncertainties, which are well below a factor of two (cf. Hayes et al. 2001; Strachan et al. 2002). We need to take into account that the pB inversion assumes axisymmetry, so that the derived density represents a structure with significant depth along the line of sight. If we are looking at a narrow structure away from the plane of the sky, and this is conceivable for the mid-latitude streamer examined here, it might contribute little brightness compared to the background

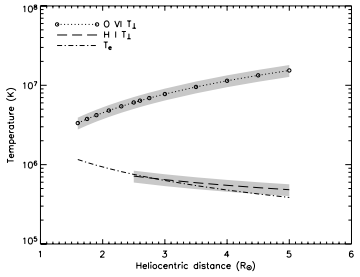

Fig. 9. Radial profiles of the O VI and H I kinetic temperatures in the direction perpendicular to the magnetic field ($T_\perp$), according to the derived empirical model. Grey bands represent the average ranges of uncertainty affecting these temperature curves. Also reported is the radial profile of the electron temperature (T_e), determined as described in the text.

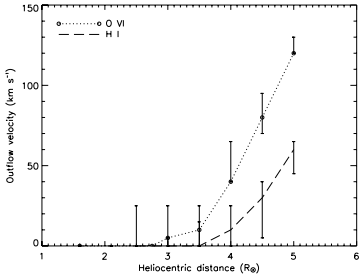

Fig. 10. Radial profiles of the outflow velocity along the streamer axis for the H I and O VI ions, according to the derived empirical model. The error bars refer to the uncertainties estimated at the various heliocentric distances as described in the text.

corona. However, we can get a much higher density for the region in the plane of the sky corresponding to the projection of the considered structure, because of the high contribution from the background corona. This could be the case for the Lyα and O VI lines originating in the streamer investigated in this work: Lyα, and most of white-light radiation, could originate in a wider and denser region along our line of sight, while the O VI emitting ions could be confined over a smaller volume. This could explain why lower densities are required to fit the O VI resonance doublet data.

Once the electron density had been derived, we deduced the electron temperature (T_e) profile along the central region of the streamer according to the method described by Gibson et al. (1999), which calculates temperatures from radial power-law fits to the combined density data set, assuming that the streamer plasma is in radial hydrostatic equilibrium. This implies that there are no significant dynamic forces and that thermal pressure is balanced by gravity. This can reasonably apply to our case, because the wind velocity may be considered as a minor term in force balance. Actually, the radial outflow velocities determined in this study reach values of about 100 km s^{-1} at heights around 5 $R_\odot$, while the thermal velocities of electrons corresponding to the temperatures found in the examined streamer are significantly higher than this value everywhere (see also the discussion in Gibson et al. 1999). The computations were carried out using both the density profile deduced from LASCO C2 pB data inversion and the one giving the best fit of the O VI observations. The differences between the two sets of T_e data so determined can be considered negligible, being around 10%. We finally adopted the T_e curve relevant to the density profile deduced from LASCO data.

The empirical radial profile of T_e is reported in Fig. 9, together with the profiles of the component of the kinetic temperature in the direction perpendicular to the magnetic field ($T_\perp$) derived for H I atoms (and protons) and O VI ions. The average uncertainty ranges pertaining to the empirical kinetic temperature curves are also reported in the figure: they were derived in terms of the lowest and highest temperature values that are still consistent with the observed line intensities, profiles, and O VI intensity ratios, within the observational uncertainties. Both the radial profiles of T_e and H I $T_\perp$ exhibit a slight decrease, practically overlapping between 2.5 and 3.3 $R_\odot$ and then only slightly diverging at greater heliocentric distances. This agrees with the hypothesis of thermal equilibrium between electrons and hydrogen atoms (protons), suggested on the basis of the high-density and low-outflow conditions characterizing streamers, expecially at low heights (cf., Raymond et al. 1997; Vásquez et al. 2003). The O VI $T_\perp$, already as high as 3 MK at 1.6 $R_\odot$, is characterized by a significant increase with height, up to nearly 15 MK, hence exhibiting much higher values than the corresponding hydrogen temperature.

As for the components of the H I and O VI kinetic temperature parallel to the magnetic field lines ($T_\parallel$), not plotted in Fig. 9, we adopted different values in the development of the empirical model, so as to consider both isotropic ($T_\parallel = T_\perp$) and anisotropic conditions with $T_\parallel = T_\perp/2$, $T_\perp/1.3$, respectively. The last value, simultaneously adopted for both neutral hydrogen and oxygen ions, seems to give the best reproduction of the observed Lyα and O VI spectral data, even if we cannot rule out the possibility of isotropic temperatures, considering the uncertainties characterizing the empirical curves plotted in the figure. On the other hand, such mildly anisotropic velocity distributions of the emitting ions are almost similar to those found by Frazin et al. (2003) in the stalk of an equatorial streamer observed at solar activity minimum.

The values of the outflow velocity along the central region of the streamer for both the H I and O VI ions were initially set equal to zero. This choice is reasonably supported by many pieces of observational evidence, suggesting that streamer axes are characterized by low-velocity outflows (e.g., Strachan et al. 2002; Uzzo et al. 2006). Subsequently, the ion speeds were progressively increased in order to match all the spectroscopic observations, until the empirical radial profiles of the H I and O VI outflow velocity reported in Fig. 10 were obtained. The error bars were deduced for each point by a procedure similar to that adopted for estimating the temperature uncertainties, and they result in about ±20 km s^{-1}. Evidence of a significant deviation from static conditions only appears at about 3.5−4.0 $R_\odot$, for both H I and O VI ions, with a progressive steepening of the outflow velocity radial profiles at greater heliocentric distances. However, the outflow velocity of coronal O VI ions at lower heights in the central region of the streamer might be underestimated in our analysis, which adopted the quiet Sun O VI line disc intensities reported by Vernazza & Reeves (1978) to perfom the synthesis of O VI emission in the streamer. Even if this approach gives a very consistent agreement with the observations, a non-negligible O VI outflow below 3.0 $R_\odot$ could result from the analysis of the observed line intensity ratio, when the possible influence of the active region sunspots present on the solar disc during the week of observation on the intensity of the

radiative scattering component of the coronal O VI lines is also considered, as discussed by Morgan & Habbal (2005).

Above 4 $R_\odot$, the O VI outflow velocity increases more rapidly than does that of H I, indicating that the former ions may flow as much as 1.5−2 times faster than the latter ones, reaching a speed of 120 km s^{-1} at 5 $R_\odot$. The faster O VI outflow velocity, together with the O VI kinetic temperatures that are much higher than the hydrogen temperatures (see above), suggest that the absorption of Alfvén waves at the ion cyclotron frequency, as proposed by several authors (e.g., Li et al. 1997, 1999; Tu & Marsch 1997; Cranmer et al. 1999a, 1999b; Hu & Habbal 1999) to explain both the high kinetic temperatures and the high ion outflow velocities observed in coronal holes, might also occur inside streamers, at least above a certain height.

4. Conclusions

The plasma parameters empirically determined at several heights in the central region of a narrow, mid-latitude streamer structure observed along different lines of sight through a week during the declining phase of the solar activity cycle 23, exhibit the following overall behavior.

The electron densities derived from the inversion of LASCO C2 pB data range from $\sim 5 \times 10^6$ cm^{-3} to $\sim 4 \times 10^4$ cm^{-3} in the 1.6−5 $R_\odot$ interval of heliocentric distance, without considerable differences among the curves relevant to the different days of observation. These densities appear to reproduce the Lyα data collected on May 22−23 quite well, while they are too high to explain the streamer emission in the O VI resonance doublet lines. To fit these data, electron densities are required that are a factor of three – four lower, so that they range from $\sim 2 \times 10^6$ cm^{-3} (at 1.6 $R_\odot$) to $\sim 1.5 \times 10^4$ cm^{-3} (at 5 $R_\odot$). Taking the axisymmetry assumed in the pB inversion into account, the above differences could result from a wider and denser region along the line of sight contributing to the white-light and Lyα radiation, while the O VI ions are probably confined over a smaller volume, away from the plane of the sky. On the other hand, Antonucci et al. (2005) report that the electron densities derived from the analysis of O VI doublet lines are generally lower than those inferred from the visible light observations.

The electron temperature profile calculated from radial power-law fits to the combined density data set exhibits a slight decrease, with values ranging from ∼1.2 MK to ∼0.4 MK in the 1.6−5 $R_\odot$ interval of heliocentric distance. The behavior of the component of the H I kinetic temperature in the direction perpendicular to the magnetic field is very similar, with only slightly higher values above 3.5 $R_\odot$. The corresponding component of the O VI kinetic temperature is characterized by a significant increase with height, from about 3 MK at 1.6 $R_\odot$ up to nearly 15 MK at 5 $R_\odot$. A mild anisotropy is noticed in the velocity distributions of the emitting ions, with the components of the H I and O VI kinetic temperature parallel to the magnetic field a factor of 1.3 smaller than the respective perpendicular components.

The outflow velocities appear negligible up to 3 $R_\odot$, whereas evidence of a significant deviation from static conditions appears at 3.5−4.0 $R_\odot$ for both H I and O VI ions, suggesting that the transition from closed to open magnetic field regions (the so-called streamer cusp) might occur within this range of heliocentric distance. Then the ion outflow velocities increase outward, reaching values of 60 km s^{-1} (H I) and 120 km s^{-1} (O VI) at 5 $R_\odot$. It is worth noting that the H I outflow velocities obtained in this work are, according to our knowledge of the literature, the first ones determined inside a streamer structure. We also note that the faster O VI outflow velocity, together with the O VI kinetic temperatures that are much higher than the H I ones, suggest that the absorption of Alfvén waves at the ion cyclotron frequency might also occur inside streamers, at least above a certain height.

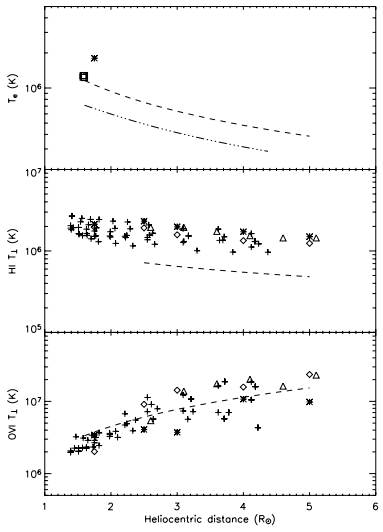

Fig. 11. T_e (*top*), H I $T_\perp$ (*middle*), and O VI $T_\perp$ (*bottom*) radial profiles derived in the streamer examined here (dashed line) and in those investigated by Gibson et al. (1999) – dash-dot-dot-dot line, Parenti et al. (2000) – squares, Strachan et al. (2002) – diamonds, Frazin et al. (2003) – triangles, Ventura et al. (2005) – crosses, Uzzo et al. (2006) – asterisks.

The physical properties summarized above can be compared with those of some other streamers described in the literature, observed during different phases of the solar cycle and/or at different latitudes. This comparison may contribute to the ongoing campaign devoted to studying the physical characteristics of coronal streamers and investigating whether structures grouped on the basis of their morphology, latitude, and solar-cycle phase appearance also share common physical conditions (see, e.g., Parenti et al. 2000; Uzzo et al. 2006). It is worth noting that the quiescent streamer reported by Uzzo et al. (2006) was at a similar latitude to the one investigated here and was observed in April 2003 while the solar activity was still decreasing. Conversely, the equatorial streamers of Gibson et al. (1999) and Strachan et al. (2002), the equatorial and mid-latitude active region streamers of Parenti et al. (2000) and the depleted-core equatorial streamer of Frazin et al. (2003) were observed during a minimum phase of the solar activity. The results presented by Ventura et al. (2005) concern a collection of streamer observations performed at different latitudes in 1997 and 2000, hence near solar minimum and maximum respectively.

The densities derived from our LASCO data are in general agreement with those reported by the authors quoted above, except for Strachan et al. (2002) and Uzzo et al. (2006), who find values at least a factor of two higher. The densities fitting our O VI data are only similar to those obtained by Ventura et al. (2005) in some mid-latitude streamers at solar minimum, but considerably lower than the values reported in other investigations.

The comparisons of T_e, H I $T_\perp$ and O VI $T_\perp$ radial profiles derived in this work with the corresponding ones obtained in some other streamers described in the literature are summarized

in Fig. 11. Significant differences are noticed among our electron temperature and H I kinetic temperature values and those reported by the majority of the other authors. As for the O VI kinetic temperatures, conversely, the agreement is generally better.

The outflow velocities derived for the O VI ions are consistent with the results concerning the other examined streamers quoted above. No significant radial outflows appear below 3 $R_\odot$, while the transition towards non-static conditions occurs within 3.5−4 $R_\odot$ in all the streamer structures considered. This behavior has also been noticed in some streamers investigated by Antonucci et al. (2005), observed near solar minimum. Above 4 $R_\odot$ all the streamers exhibit a sharp increase in the outflow velocity, up to values around 100 km s^{-1} at 5 $R_\odot$. This increase is steeper in the structure examined here than in those described by Strachan et al. (2002) and Uzzo et al. (2006).

Finally, we computed the 1 AU scaled particle-flux density from the densities and outflow velocities determined at 5 $R_\odot$, assuming a pure radial expansion factor (see, for instance, Strachan et al. 2002). We find $\sim 1.3 \times 10^8$ cm^{-2} s^{-1}. This is a factor of three lower than the in situ measurements for the particle flux density of the slow solar wind (e.g., Gosling 1997; Phillips et al. 1995), and even lower than the value of 5.4×10^8 cm^{-2} s^{-1}, found by Strachan et al. (2002) in an equatorial streamer at solar minimum.

Acknowledgements. The authors wish to thank Y.-K. Ko for her assistance during UVCS/SOHO observations carried out at NASA GSFC, and R. Suleiman for his help in the preliminary reduction of the UVCS raw data. They also thank S. R. Habbal for her comments and suggestions, which led to a much sounder version of the manuscript. This work was supported in part by the Agenzia Spaziale Italiana (contracts ASI I/R/84/02 and I/035/05/0). The work of E. Landi is supported by the NNG06EA14I, NNH06CD24C and other NASA grants.

References

Allen, L. A., Habbal, S. R., & Hu, Y. Q. 1998, JGR, 103, 6551
Antonucci, E., Abbo, L., & Dodero, M. A. 2005, A&A, 435, 699
Brueckner, G. E., Howard, R. A., Koomen, M. J., et al. 1995, Sol. Phys., 162, 357
Cranmer, S. R., Field, G. B., & Kohl, J. L. 1999a, ApJ, 518, 937
Cranmer, S. R., Kohl, J. L., Noci, G. C., et al. 1999b, ApJ, 511, 481
Domingo, V., Fleck, B., & Poland, A. I. 1995, Sol. Phys., 162, 1
Fineschi, S., Gardner, L. D., Kohl, J. L., Romoli, M., & Noci, G. C. 1998, Proc. SPIE, 3443, 67
Frazin, R. A., Cranmer, S. R., & Kohl, J. L. 2003, ApJ, 597, 1145
Gardner, L. D., Kohl, J. L., Daigneau, P. S., et al. 1996, Proc. SPIE, 2831, 2
Gibson, S. E., Fludra, A., Bagenal, F., et al. 1999, JGR, 104, 9691
Gosling, J. T. 1997, Robotic Exploration Close to the Sun, ed. S. R. Habbal (Woodbury: AIP), AIP Conf. Proc., 385, 17
Gouttebroze, P., Lemaire, P., Vial, J. C., & Artzner, G. 1978, ApJ, 225, 655
Habbal, S. R., Woo, R., Fineschi, S., et al. 1997, ApJ, 489, L103
Hayes, A. P., Vourlidas, A., & Howard, R. A. 2001, ApJ, 548, 1081
Hu, Y. Q., & Habbal, S. R. 1999, JGR, 104, 17,045
Kohl, J. L., Esser, R., Gardner, L. D., et al. 1995, Sol. Phys., 162, 313
Kohl, J. L., Noci, G., Antonucci, E., et al. 1997, Sol. Phys., 175, 613
Kohl, J. L., Noci, G., Cranmer, S. R., & Raymond, J. C. 2006, A&AR, 13, 31
Lemaire, P., Wilhelm, K., Curdt, W., et al. 1997, Sol. Phys., 170, 105
Li, X., Esser, R., Habbal, S. R., & Hu, Y.-Q. 1997, JGR, 102, 17419
Li, X., Habbal, S. R., Hollweg, J. V., & Esser, R. 1999, JGR, 104, 2521
Low, B. C. 2001, JGR, 106, 25141
Marsch, E. 1997, in Fifth SOHO Workshop, The Corona and Solar Wind near Minimum Activity, ed. A. Wilson (Noordwijk: ESA), ESA-SP 404, 135
Morgan, H., & Habbal, S. R. 2005, ApJ, 630, L189
Noci, G., & Gavryuseva, E. 2007, ApJ, 658, L63
Noci, G., Kohl, J. L., & Withbroe, G. L. 1987, ApJ, 315, 706
Noci, G., Kohl, J. L., Antonucci, E., et al. 1997, in Fifth SOHO Workshop, The Corona and Solar Wind near Minimum Activity, ed. A. Wilson (Noordwijk: ESA), ESA-SP 404, 75
Parenti, S., Bromage, B. J. I., Poletto, G., et al. 2000, A&A, 363, 800
Phillips, J. L., Bame, S. J., Barnes, A., et al. 1995, GRL, 22, 3301
Raymond, J. C., Kohl, J. L., Noci, G., et al. 1997, Sol. Phys., 175, 645
Spadaro, D., & Ventura, R. 1993, A&A, 276, 571
Spadaro, D., & Ventura, R. 1994a, A&A, 281, 245
Spadaro, D., & Ventura, R. 1994b, A&A, 289, 279
Spadaro, D., & Ventura, R. 1996, A&AS, 115, 531
Strachan, L., Suleiman, R., Panasyuk, A. V., Biesecker, D. A., & Kohl, J. L. 2002, ApJ, 571, 1008
Tu, C.-Y., & Marsch, E. 1997, Sol. Phys., 171, 363
Uzzo, M., Strachan, L., Vourlidas, A., Ko, Y.-K., & Raymond, J. C. 2006, ApJ, 645, 720
Vásquez, A. M., van Ballegooijen, A. A., & Raymond, J. C. 2003, ApJ, 598, 1361
Ventura, R., & Spadaro, D. 1999, A&A, 341, 264
Ventura, R., Spadaro, D., Cimino, G., & Romoli, M. 2005, A&A, 430, 701
Vernazza, J. E., & Reeves, E. M. 1978, ApJS, 37, 485
Wilhelm, K., Curdt, W., Marsch, E., et al. 1995, Sol. Phys., 162, 189
Wilhelm, K., Lemaire, P., Curdt, W., et al. 1997, Sol. Phys., 170, 75
Withbroe, G. L., Kohl, J. L., Weiser, H., & Munro, R. H. 1982, Space Sci. Rev., 33, 17
Woo, R., & Martin, J. 1997, GRL, 24, 2535
Woods, T. N., Tobiska, W. K., Rottman, G. J., & Worden, J. R. 2000, JGR, 105, 27195
Zangrilli, L., Nicolosi, P., Poletto, G., et al. 1999, A&A, 342, 592